Applications of the Faraday Effect in Hot Atomic Vapours

Mark A. Zentile

Abstract

This thesis presents both a computational and experimental investigation into light propagation in hot alkali-metal vapours, with a particular focus on utilizing the Faraday effect for practical applications. A model to calculate various spectra for a weak-probe laser beam in an atomic medium with an applied axial magnetic field is presented. A computer program (ElecSus) was developed which implements this model efficiently. Using ElecSus we design optical devices such as Faraday filters and laser frequency stabilizing references. The design of Faraday filters utilizing compact vapour cells is shown, along with excellent agreement with experiment. The importance of including the effect of self broadening in the model is shown for these short path length vapour cells. Also, a Faraday filter is presented that can potentially be used for quantum optics experiments on the caesium D_1 line (894 nm). The filter displays the highest ratio of transmission to equivalent noise bandwidth to date for a linear Faraday filter, demonstrating the power of computerized optimization for this application. Furthermore, a Faraday filter is presented for use as an intra-cavity element in an external-cavity diode laser. A proof-of-principle experiment is demonstrated which shows that using a short external cavity with the Faraday filter eliminates mode-hops.

Experimentally and theoretically the Faraday effect is investigated in large magnetic fields where alkali-metal atoms enter the hyperfine Paschen-Back regime. This hyperfine Paschen-Back Faraday effect is shown to allow a direct measure of the refractive indices for left and right circular polarized light. Furthermore, fitting the weak-probe spectra using ElecSus is found to give measures of the magnetic field with a fractional precision of the order of 10^{-4}. In addition we study slow-light pulse propagation in a high density rubidium vapour, showing that our theoretical model for the electric susceptibility is valid for short pulses as well as continuous-wave light. This shows that the model is accurate for predicting weak-probe pulse propagation.

Applications of the Faraday Effect in Hot Atomic Vapours

Mark A. Zentile

A thesis submitted in partial fulfilment
of the requirements for the degree of
Doctor of Philosophy

Department of Physics
Durham University

July 28, 2015

Declaration

I confirm that no part of the material offered has previously been submitted by myself for a degree in this or any other University. Where material has been generated through joint work, the work of others has been indicated.

Mark A. Zentile
Durham, July 28, 2015

Acknowledgements

I acknowledge funding from a studentship from the Engineering and Physical Sciences Research Council.
In a variety of ways, many people have helped me with the creation of this thesis. I would like to take this opportunity to thank them all.
Firstly, I would like to thank all my colleagues and friends who I have had the pleasure to work with in the "slow-light" project. I thank my supervisors Ifan Hughes and Charles Adams for taking me on as a Ph.D. student, and giving me the opportunity to work on a fascinating area of physics. I'm grateful also for their encouragement and patience throughout my Ph.D. work (even after breaking expensive equipment!). To Ifan, I also thank for his open-door policy for which I have taken advantage of to discuss anything and everything. To Charles, I also thank for insights and ideas that have ensured that we never ran out of interesting things to investigate. A huge thanks goes to Lee Weller, who spent a large amount of time patiently training me to use the lab equipment and teaching me the data analysis techniques. I really enjoyed the time we spent working together. I am very grateful to James Keaveney for the time spent helping me with problems about python programming/electronics/lab equipment, which meant solutions were found far quicker than I would have been able to do alone. The day-to-day running of the experiments is now in the very capable hands of Dan Whiting, James Keaveney and Erwan Bimbard who I wish the best of luck in future discoveries and endeavours. I'm particularly pleased that the "what if the magnetic field was larger" mentality seems to be as strong as ever. Is there any problem that won't be solved by a larger magnet!
I would also like to thank three summer students who played a significant role in the investigations presented in this thesis, and who achieved a tremendous amount in the short time we worked together. I would like to thank Rebecca Andrews for setting up the "hyperfine Paschen-Back Faraday effect" experiment and taking the data with me. I thank Renju Mathew and Will Hamlyn who's work on Faraday filters has helped us all understand them a lot better. I also thank Will for building the temperature control circuit used to stabilize the cell temperature for the Faraday-filter laser.
To the wider JQC Durham Physics group (previously known as AtMol) I am truly grateful for the friendly atmosphere and the patience to listen to my long winded rants during tea breaks. There are many people from which

I've borrowed bits of equipment which made the investigations in this thesis progress so much faster and smoother than otherwise would have been the case; I thank you all. Specifically, I'd like to thank Kevin Weatherill and Chris Wade for not only allowing me use of the Ti:Sapph laser but also accommodating me in your lab and teaching me how to use the laser. On the subject of equipment, I would also like to thank Svenja Knappe, from NIST, for providing the microfabricated vapour cells, which were essential for some of the studies in this thesis.
Also thanks must be said for Ifan, James and Dan as well as my sister, Catherine, and brother-in-law, Chris, who kindly proof read this thesis as well as providing general comments. It should be noted that whatever typographical and grammatical errors remain, they are a tiny fraction of the vast number weeded out from the first draft!
I also thank rest of my family: Mum, Dad, Nana, Granddad, and auntie Lucy for all their love and support. And finally I thank Jennie for making my whole 8 years at Durham a truly wonderful experience.

Contents

List of Figures

List of Tables

Chapter 1

Introduction

Optical media consisting of a gas of single atoms have remarkable properties which can be exploited for a large range of applications. Since indistinguishable atoms can be thought of as identical oscillators, gaseous ensembles of atoms can be used to create clocks with unprecedented precision, long term stability and reproducibility [1]. Also, since electromagnetic fields affect the atomic state, probing the atomic gases can be a way to sense these fields with high precision [2]. On the other hand, the atoms will affect the light which interacts with it and so we can envisage using atomic media as optical elements to manipulate light.

Since the invention of laser cooling, cold atoms have been a workhorse for research into many phenomena. They provide an opportunity to do research that would otherwise be impossible, such as studies on Bose-Einstein condensates [3], or the interaction between individual atoms [4] in optical dipole traps [5]. However, in recent years the interest in thermal atomic vapours is increasing, especially for creating compact devices. This is due to experiments with thermal atomic vapours generally being simpler, cheaper, smaller and lighter in mass. Using vapour cells allows one to tune the atomic number density over several orders of magnitude. From figure 1.1, we can see that we can exceed the number densities that can be achieved in cold-atom experiments by heating the vapour cell. Although, this is at the cost of increased line-broadening due to the Doppler effect.

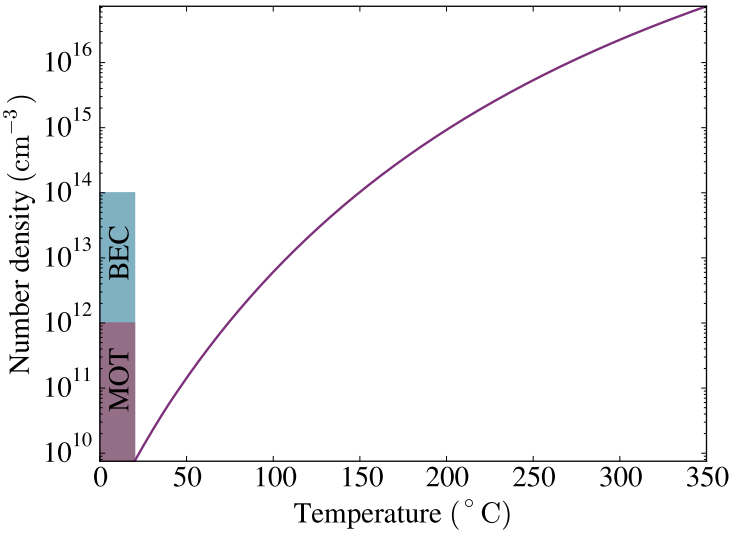

Figure 1.1: Number density of atomic rubidium, in the gas phase, as a function of temperature (using formula given in [6]). The typical maximum number density in magneto-optical trap (MOT) and Bose-Einstein condensate (BEC) experiments are 10^{12} and 10^{14} cm^{-3} respectively [7].

1.1 Motivation for smaller cells

The attenuation of the intensity, I, of weak[1] monochromatic light by a medium of length ℓ is given by the well known Beer-Lambert law,

$$I = I_0 \exp(-\alpha \ell), \tag{1.1}$$

where I_0 is the initial intensity and α is known as the attenuation coefficient. Interesting phenomena such as Rydberg blockade [8], the cooperative Lamb shift [9, 10], saturated opacity [11] and enhanced energy transfer [12] can be seen at large atom number densities. The high number density will cause α to be large, causing conventional cell lengths of a few centimetres to be optically thick close to the atomic resonances. This means that it can be difficult for a probe beam to extract information about the sample. One way round this problem may be to tune the probe beam away from the atomic resonance and then use a dispersive signal [13], however this technique may not suitable for applications where we need to work near resonance (e.g. measuring shifts

[1] There are many times in this thesis where we will make the approximation that the light is 'weak', but in full generality this means the intensity is small enough such that the behaviour of the medium is independent of intensity.

of resonance lines). Another idea is to use selective reflection [14] as the signal, or possibly use electromagnetically-induced transparency [15]. One straightforward solution is to reduce ℓ such that the optical depth is small enough for some of the probe beam to pass through the atomic medium and provide a signal. Remarkably, vapour cells with path lengths as small as 30 nm have now been demonstrated [10].

Other than fundamental physics, the use of compact vapour cells is of interest for applied physics[2]. Making atomic devices more compact, power efficient and lighter is currently a burgeoning area of research [16–18], since it allows them to become practical and mobile consumer products. Particularly for devices that require an applied magnetic field, compact vapour cells [19–25] offer the additional advantage that small permanent magnets can be used as an alternative to current carrying coils to create a uniform magnetic field across the vapour cell [26], while consuming no power.

1.2 The hyperfine Paschen-Back regime

Another advantage of using permanent magnets to apply magnetic fields to atomic vapours is that large magnetic fields are more easily accessible. Some applications require very large fields [27–30] to be applied to the atomic vapour. As we will see in this thesis (section 4.2), magnetic fields of the order 10 kG can be applied using compact permanent magnets. At these large fields alkali-metal atoms enter the hyperfine Paschen-Back regime [31–36], where the nuclear spin, and the total electronic angular momenta are decoupled. Exceptionally, for lithium a magnetic field of the order of 10 kG is strong enough to also decouple the orbital and spin angular momenta of the electron [37].

The hyperfine Paschen-Back (HPB) regime is also of interest for studies of coherent dynamics as individual transitions can become separately addressable [38, 39]. This happens when the magnetic field breaks the degeneracy and the spacing between the transitions is greater than the Doppler width; allowing ideal two- or three-level systems to be realized [39].

[2] Although, today's fundamental physics is tomorrow's applied.

1.3 The Faraday effect

In 1846, Faraday discovered that the plane of polarization of light rotates when travelling through various media with an applied axial magnetic field [40]. This was the first magneto-optic phenomenon discovered, and showed that light, magnetism and electricity are related.

The Faraday effect has many applications, since it allows precise manipulation of the polarization of light. The effect has uses in optical filtering [41], quantum memories [42], optical isolation [29], optical limitation [43] and off-resonance laser-frequency stabilization [44, 45], to name only a few.

The Faraday effect has been studied in many regimes. The resonant Faraday effect (also known as the Macaluso-Corbino effect [46]) is characterized when the light's frequency is near the atomic resonance. The off-resonant Faraday effect [47] is characterized when the light is detuned far from the atomic resonance. However, both these phenomena are often only studied for weak magnetic fields, such that the Zeeman shift is smaller than the line-broadening. In chapter 5 the Faraday effect is studied in the hyperfine Paschen-Back regime, where for ^{87}Rb the Zeeman shift is much larger than the atomic line-broadening.

1.3.1 Faraday filters

In 1956, Öhman noticed [41] that the resonant Faraday effect could be used to create a filter by placing crossed polarizers around an optical medium subject to an axial magnetic field. Faraday filters were later applied to solar observations [48, 49] and used to frequency stabilize dye lasers [50–52]. In the early 1990s the subject of Faraday filters was revived [53, 54]. Such filters have received increasing attention ever since, owing to their high performance in many applications. Faraday filters now find use in remote temperature sensing [55], atmospheric lidar [56–59], diode laser frequency stabilisation [60–62], Doppler velocimetry [49, 63, 64], communications [65] and quantum key distribution [66] in free space, optical limitation [43], filtering Raman light [67], and quantum optics experiments [68, 69].

It's interesting to note that the same apparatus used to create a Faraday

filter can be used to create an optical isolator [29], a device which has high transmission in one direction but low transmission in the opposite direction[3]. This is achieved by rotating one of the polarizers such that they are at 45° with respect to one another. Also the temperature and magnetic field are chosen such that there is a 45° Faraday rotation rather than a 90° rotation needed for a Faraday filter.

The main advantages to using Faraday filters over similarly spectrally-narrow Fabry-Perot etalons is that they are cheaper, and more robust to temperature changes or vibrations [57]. Another advantage to using Faraday filters is that they typically have a very large field of view [71], in contrast to fibre Bragg gratings.

1.4 Aim of this thesis

The aim of this investigation is to further the understanding of the underlining physics of optical devices utilizing thermal atomic vapours. The Faraday effect is of particular interest since it allows the manipulation of the polarization state of light. Also, the use of compact, short path-length vapour cells in this thesis (and the new physics that must be considered) is important since these will make the most practical devices. In this thesis we describe a model to calculate the weak-probe electric susceptibility of an ensemble of hot alkali-metal atoms. We then develop a computational implementation of the model which is open source and fast. This computer program (ElecSus) includes global fitting routines to effectively fit the model to experimental data. Also the speed of the program allows one to interface the program with optimization routines, which allows the optical properties of the vapour to be efficiently designed. We use this technique extensively to design Faraday filters for alkali metals.

1.5 Thesis summary

The rest of this thesis is structured as follows:

[3] or more precisely, a device which breaks "Lorentz reciprocity" [70].

Chapter 2. Here we develop a model to calculate the electric susceptibility of an ensemble of hot alkali-metal atoms. This model underpins the rest of the work in this thesis. The model is then used to discuss the hyperfine Paschen-Back regime and the Faraday effect.

Chapter 3. The computational implementation of the model (the ElecSus program [72]) for the electric susceptibility is described. Also, we explain how to calculate signals that would be seen in experiments such as transmission or other Stokes parameters. The methods used to fit the theory to the data are explained and we describe how fitting to local solutions is avoided by using global fitting routines.

Chapter 4 This chapter details the experimental apparatus and techniques used for the investigations in this thesis. We show how the atomic medium is prepared by showing the vapour cells used and describing their heaters. Also we describe how to apply a magnetic field using permanent magnets that have their dimensions precisely designed. We then go on to explain how the laser frequency is calibrated when taking atomic spectra and also explain how pulsed light is generated from a continuous-wave beam. These techniques form the basis of the experiments in the following chapters.

Chapter 5. We show that unique properties of an atomic vapour emerge at the very high magnetic fields of the hyperfine Paschen-Back regime. The Faraday effect in this regime is shown to have three important applications:

- Weak-probe spectroscopy can be used to measure the magnetic field with a relative precision at the 10^{-4} level.
- The Faraday spectra are good approximations to the refractive indices of the vapour, and so could be used as a direct measure.
- The Faraday spectra can be used as a laser-frequency reference that is far detuned from the usual atomic resonances seen at zero magnetic field; a highly temperature stable way of off-resonance laser locking.

Chapter 6. In this chapter we describe the technique of Faraday filtering. We use computer optimization in order to design the best working conditions of Faraday filters. Computer optimization is also employed as a

tool to explain how line broadening affects the performance of Faraday filters. The effect of homogeneous and inhomogeneous broadening mechanisms are explored for both 'wing' and 'line-centre' filters. We show how wing-type filters are extremely sensitive to homogeneous broadening mechanisms. This result is of particular importance for the design of compact Faraday filters, where dense vapours are necessary but are subject to homogeneous 'self' broadening.

Chapter 7. Using the technique of computer optimization, we find that the caesium D_1 line performs best for a key figure of merit. Experimentally, we realize the predicted caesium D_1 filter, which achieves a performance that surpasses any other Faraday filter demonstrated to date. This filter could be incorporated into quantum optics experiments that utilize the Cs D_1 line.

Chapter 8. We experimentally demonstrate a diode laser system where a Faraday filter is used in an external cavity as the frequency selective element. We again employ the ElecSus program in order to find the optimal filter parameters. This 'Faraday-filter laser' is the first to be made where the cavity free-spectral range is greater than the filter width. This means that the laser frequency does not mode hop within the filter profile. This kind of laser system is in principle more mechanically stable than grating based external cavity diode lasers, with the caveat that it is less frequency tunable.

Chapter 9. ElecSus is used to design a slow-light medium with an atomic rubidium vapour. An experiment is described, where the medium is probed with nano-second pulses, to test the theoretical prediction. The agreement between experiment and theory is excellent, showing that we can use the absorptive and dispersive properties calculated by ElecSus to accurately model weak-probe pulse propagation.

Chapter 10. Here we summarize the main conclusions of this thesis and briefly look at studies that could be done in future that build on the work presented here.

1.6 Publications

During the work for this thesis several journal articles have been published. The work is a collaborative effort between the named authors, with all authors contributing to the discussions of the results as well as contributing to the preparation of the article. The specific contributions of this author has been listed under the respective article.

1.6.1 Publications arising from this work

Listed here are journal articles which have arisen from the work carried out for this thesis. As such, these articles form the basis of some of the chapters.

[72] M. A. Zentile, J. Keaveney, L. Weller, D. J. Whiting, C. S. Adams, and I. G. Hughes, *ElecSus: A program to calculate the electric susceptibility of an atomic ensemble*, Comput. Phys. Commun. **189**, 162 (2015).

- Assembled the experiments, and acquired and analysed the data.
- Wrote the majority of the ElecSus code in it's present form.
- Lead the writing of the article, creating all the figures and writing the majority of the text.

[73] M. A. Zentile, D. J. Whiting, J. Keaveney, C. S. Adams, and I. G. Hughes, *Atomic Faraday filter with equivalent noise bandwidth less than 1 GHz*, Opt. Lett. **40**, 2000 (2015).

- Performed the computerized optimization.
- Assembled the experiment, and acquired and analysed the data.
- Lead author of the article.

[74] M. A. Zentile, J. Keaveney, R. S. Mathew, D. J. Whiting, C. S. Adams, and I. G. Hughes, *Optimisation of atomic Faraday filters in the presence of homogeneous line broadening*, ArXiv:1504.03651 (2015), accepted for publication in J. Phys. B At. Mol. Opt. Phys.

- Performed the computerized optimizations and theoretical analysis.
- Assembled the experiment, and acquired and analysed the data.
- Lead author of the article.

[45] M. A. Zentile, R. Andrews, L. Weller, S. Knappe, C. S. Adams, and I. G. Hughes, *The hyperfine Paschen-Back Faraday effect*, J. Phys. B At. Mol. Opt. Phys. **47**, 075005 (2014).

- Performed the theoretical calculations.
- Acquired the data alongside R. Andrews, and analysed the data.
- Lead author of the article.

[29] L. Weller, K. S. Kleinbach, M. A. Zentile, S. Knappe, I. G. Hughes, and C. S. Adams, *Optical isolator using an atomic vapor in the hyperfine Paschen-Back regime*, Opt. Lett. **37**, 3405 (2012).

- Assisted in taking the experimental data.
- Analysed the experimental data used to characterize the vapour cell.

[26] L. Weller, K. S. Kleinbach, M. A. Zentile, S. Knappe, C. S. Adams, and I. G. Hughes, *Absolute absorption and dispersion of a rubidium vapour in the hyperfine Paschen-Back regime*, J. Phys. B At. Mol. Opt. Phys. **45**, 215005 (2012).

- Assisted in taking the experimental data.
- Fitted some of the experimental data to theory.

1.6.2 Other work

The following publications arose during the work for this thesis. Whilst they are relevant, they do not underpin the work presented in this thesis.

[12] L. Weller, R. J. Bettles, C. L. Vaillant, M. A. Zentile, R. M. Potvliege, C. S. Adams, and I. G. Hughes, *Cooperative Enhancement of Energy Transfer in a High-Density Thermal Vapor*, ArXiv:1308.0129 (2013).

- Assisted in taking the experimental data.
- Performed the theoretical analysis concerning the kinetic theory.

[39] D. J. Whiting, E. Bimbard, J. Keaveney, M. A. Zentile, C. S. Adams, and I. G. Hughes, *Electromagnetically induced absorption in a non-degenerate three-level ladder system*, (2015) in preparation.

- Designed the magnets and cell heater used for the experiment.
- Characterized the vapour cell.

Part I

Theory and computational methods

Chapter 2

A model for the weak-probe electric susceptibility of an atomic vapour

2.1 Introduction

This chapter outlines how to calculate the attenuation and dispersion of light for a hot atomic gas. We will start with a plane wave solution to Maxwell's wave equation in free space, then modify it to include a medium with a frequency dependent refractive index (dispersion) and attenuation. It is shown that the electric susceptibility is key in calculating these properties.

The applied electric field is then linked to the atomic polarizability, in order to describe the macroscopic electric susceptibility from the microscopic atomic polarizability. Then using the steady state solution to the optical Bloch equations, the susceptibility for a two-level atomic medium is found. This is then generalized for a multi-level atom giving us our final result.

Note that the model is 'semi-classical', where the light is treated as a classical wave and the atomic system is treated quantum mechanically. The quantum nature of light is not expected to be required since the electromagnetic field is not strongly coupled to the atom. This means that photons that interact with an atom only do so once, unlike a cavity system for example [75].

2.2 A plane wave in a dispersive medium

We start by considering a monochromatic plane wave of an electric field restricted to propagation in one dimension. Plane waves are solutions to Maxwell's wave equation [76], and are a sufficient approximation to the Gaussian laser beams used experimentally for this thesis [77]. We choose to write the plane wave as,

$$\boldsymbol{E}(z,t) = \boldsymbol{E}_0 \exp(\mathrm{i}[kz - \omega t]), \tag{2.1}$$

where z is the propagation direction, t is time, ω is the angular frequency and k is the wavenumber defined as $k \equiv 2\pi/\lambda$, where λ is the wavelength. $\boldsymbol{E}_0$ is a complex amplitude, and is a vector which lies in the x-y plane (a transverse wave). We have written the electric field as a complex number, but in principle it is a directly observable quantity and so should be real valued. However, this complex solution to the Maxwell's wave equation is more mathematically convenient when dealing with a superposition of waves with different phases (see chapter 9). We should interpret the real part of equation (2.1) as representing the electric field [76, 78].

The wavenumber in a medium can be represented by its value in vacuum (k_0) using the relation, $k = nk_0$, where n is the refractive index of the medium, defined as the ratio of the speed of light in vacuum to the phase velocity in the medium ($n \equiv c/v_p$). In this way we can parameterize the phase shift caused by the medium. However, we could instead allow a complex index of refraction, ($n_c \equiv n + \mathrm{i}\beta$). We now write the wavenumber as follows,

$$k = n_c k_0. \tag{2.2}$$

Putting this into equation (2.1) we get,

$$\boldsymbol{E}(z,t) = \boldsymbol{E}_0 \exp(\mathrm{i}[n_c k_0 z - \omega t]), \tag{2.3}$$

$$\boldsymbol{E}(z,t) = \boldsymbol{E}_0 \exp(-\beta k_0 z) \exp(\mathrm{i}[n k_0 z - \omega t]). \tag{2.4}$$

By allowing a complex index of refraction, we have parameterized the attenuation in the medium as well as the phase shift. We can see this more clearly

if we use the relation for the intensity of light from a sinusoidal wave [78],

$$I = \frac{1}{2} n \epsilon_0 c |\boldsymbol{E}|^2, \tag{2.5}$$

where ϵ_0 is the permittivity of free space. Therefore the transmission $\mathcal{T}$ after traversing a medium of length ℓ will be given by,

$$\mathcal{T} \equiv \frac{I}{I_0} = \exp(-2\beta k_0 \ell). \tag{2.6}$$

This is simply the Beer-Lambert law (see equation (1.1)) with the attenuation coefficient given by,

$$\alpha = 2\beta k_0. \tag{2.7}$$

Also evident is that the medium imparts a phase shift, $\Delta\phi$, (when compared to a wave travelling in vacuum) of,

$$\Delta\phi = (n-1) k_0 \ell. \tag{2.8}$$

In general, n_c changes with optical frequency and so we need to calculate its spectrum for an atomic medium. This will allow us to compare theory and experiment by spectroscopy.

2.3 The electric susceptibility

We require a link between our macroscopic n_c quantity and the microscopic behaviour of the atoms. We can start by noting that the applied electric field from the light should electrically polarize an atom, since its bound charges will interact with the electric field. If the wavelength of light is much larger than the size of the atom, then the atom will closely resemble a dipole [79]. This will cause the macroscopic medium to be polarized, $\boldsymbol{P}$, in the following way [78],

$$\boldsymbol{P} = \sum_a \mathcal{N}_a (\boldsymbol{d}_a)_{\mathrm{av}}, \tag{2.9}$$

where $\mathcal{N}_a$ is the number density of the a'th type of identical atom and $(\boldsymbol{d}_a)_{\text{av}}$ is the spatial average of its dipole moment. If we also ignore local field effects[1] (valid for low number density) we can simply write,

$$\boldsymbol{P} = \sum_a \mathcal{N}_a \boldsymbol{d}_a, \tag{2.10}$$

without taking the spatial average. However, the atom has been treated as a classical dipole. To treat the atom quantum mechanically, we should replace $\boldsymbol{d}_a$ with the expectation value of the dipole operator. The dipole operator is given by $\boldsymbol{d} \equiv e\boldsymbol{r}$, where e is the elementary charge and $\boldsymbol{r}$ is the position of the electron from the nucleus. This gives us,

$$\boldsymbol{P} = \sum_a \mathcal{N}_a \langle \boldsymbol{d} \rangle_a. \tag{2.11}$$

Since an atomic gas is macroscopically isotropic, the medium's polarization should be in the same direction to the applied field and directly proportional. Therefore,

$$\boldsymbol{P} = e_0 \chi \boldsymbol{E}, \tag{2.12}$$

where e_0 is the vacuum permittivity and χ is known as the electric susceptibility. Note that $e_0\chi$ is simply the proportionality constant, written such that χ is dimensionless. This equation defines χ. Also since the polarization of the medium may not be entirely in phase with $\boldsymbol{E}$, χ is necessarily a complex number. Another feature to note about equation (2.12) is that the polarization is linear with the applied electric field. This is actually an approximation. Very large electric fields will in general cause a non-linear response by the medium [81], but since only weak fields will be used in this thesis, linearity is a safe approximation.

The complex index of refraction is related to χ by the equation [78]

$$n_c = \sqrt{1+\chi} \approx 1 + \frac{\chi_{\text{re}}}{2} + \mathrm{i}\frac{\chi_{\text{im}}}{2}, \tag{2.13}$$

where the approximation is valid when $|\chi|$ is small. Note that under this approximation, the attenuation coefficient can now be given by $\alpha = k\chi_{\text{im}}$

[1] See [80] for further discussion of local field effects in atomic vapours.

and the phase shift is given by $\Delta\phi = \frac{1}{2}\chi_{\mathrm{re}} k_0 \ell$.

Having linked the electric susceptibility to the medium's dispersion and attenuation, a calculation of the expectation value of the dipole operator is now required in order to calculate χ.

2.3.1 The two-level atom

We start by considering the simplest atomic ensemble, consisting of only identical two-level atoms. The atom has a ground state, $|\mathrm{g}\rangle$, and an excited state, $|\mathrm{e}\rangle$. The excited state decays spontaneously into the ground state with a rate constant of Γ_0. The two states are separated in energy by $\hbar\omega_0$ (where $\hbar$ is the reduced Plank's constant), and are coupled via a plane wave. It is convenient to define the detuning, $\Delta = \omega - \omega_0$ which is the difference of the light's angular frequency to the resonant frequency of the transition.

Since we are considering only one type of atom we will simplify our notation for the expectation of the dipole operator, $\langle \boldsymbol{d} \rangle_a = \langle \boldsymbol{d} \rangle$. We want to describe the evolution of the atomic wave-function, as the atom interacts with the light (under the assumption that the atom can be described as a dipole), and hence calculate $\langle \boldsymbol{d} \rangle$. This is a well known problem and can be described using a matrix formalism and the optical Bloch equations with the Lindblad operator (see page 72 in [79]). Here we simply quote the results.

From the density matrix formalism (see page 643 in [82]), we can write the expectation value as

$$\langle \hat{\boldsymbol{d}} \rangle = \mathrm{Tr}(\hat{\boldsymbol{d}}\hat{\rho}) = \boldsymbol{d}_{\mathrm{ge}}(\rho_{\mathrm{ge}} + \rho_{\mathrm{eg}}), \tag{2.14}$$

where the diagonal matrix elements of $\hat{\boldsymbol{d}}$ are zero[2] and the off diagonal elements are both equal (so we simply label them $\boldsymbol{d}_{\mathrm{ge}} \equiv \langle \mathrm{g}|\boldsymbol{d}|\mathrm{e}\rangle$). We then define $\rho_{\mathrm{ge}} \equiv \tilde{\rho}_{\mathrm{ge}} \exp(\mathrm{i}\omega t)$ and $\rho_{\mathrm{eg}} \equiv \tilde{\rho}_{\mathrm{eg}} \exp(-\mathrm{i}\omega t)$, so we can write

$$\langle \hat{\boldsymbol{d}} \rangle = \boldsymbol{d}_{\mathrm{ge}}[\tilde{\rho}_{\mathrm{ge}} \exp(\mathrm{i}\omega t) + \tilde{\rho}_{\mathrm{eg}} \exp(-\mathrm{i}\omega t)]. \tag{2.15}$$

If we also substitute the real part of the plane wave (equation (2.1), under

[2] This is due to the odd parity the dipole operator (see [83] for further discussion).

the dipole approximation of $z = 0$) into equation (2.12), we can write

$$\boldsymbol{P} = \frac{1}{2}\epsilon_0 \boldsymbol{E}_0[\chi \exp(-\mathrm{i}\omega t) + \chi^* \exp(\mathrm{i}\omega t)]. \tag{2.16}$$

Substituting equation (2.15) into (2.11) and then equating with (2.16) yields,

$$\mathcal{N}\boldsymbol{d}_{\mathrm{ge}}[\tilde{\rho}_{\mathrm{ge}} \exp(\mathrm{i}\omega t) + \tilde{\rho}_{\mathrm{eg}} \exp(-\mathrm{i}\omega t)] = \frac{1}{2}\epsilon_0 \boldsymbol{E}_0[\chi \exp(-\mathrm{i}\omega t) + \chi^* \exp(\mathrm{i}\omega t)], \tag{2.17}$$

where we can immediately identify,

$$\chi = \frac{2\mathcal{N} d_{\mathrm{ge}}}{\epsilon_0 E_0}\rho_{\mathrm{eg}}. \tag{2.18}$$

The steady-state solution of the optical Bloch equations, under the rotating wave approximation, is then used to calculate

$$\rho_{\mathrm{eg}} = \frac{\mathrm{i}d_{\mathrm{ge}}E_0}{2\hbar(\Gamma_0/2 - \mathrm{i}\Delta)}. \tag{2.19}$$

Therefore we can write

$$\chi(\Delta) = \frac{d_{\mathrm{ge}}^2 \mathcal{N}}{\epsilon_0 \hbar} f(\Delta), \tag{2.20a}$$

$$f(\Delta) = \frac{\mathrm{i}}{\Gamma_0/2 - \mathrm{i}\Delta}. \tag{2.20b}$$

One final element to calculate is d_{ge}. This can be calculated *ab initio*, where a model is built up by calculating the eigenstates of the valence electron in the potential of the ionic core. However this technique is limited by imprecise knowledge of the ionic core potential. However, it can be shown that d_{ge} can be calculated from the decay rate Γ_0 by using [79]

$$d_{\mathrm{ge}} = \sqrt{\frac{3\pi\epsilon_0\hbar c^3\Gamma_0}{\omega_0^3}}. \tag{2.21}$$

The decay rates are measurable quantities and are well known for alkali-metal atoms (see section B.2 where the values are provided).

Discussion of the two-level atom result

This result has utilized the steady-state solution of the optical Bloch equations. The steady-state solution is valid when the atoms spend a long time in the beam relative to their decay time (τ) [79]. For a typical laser beam sizes of $\sim 1\,\mathrm{mm}$, the majority of atoms in a thermal vapour cell will spend $> 40\,\tau$ in the beam (see discussion in section 6.5.1 of [84]). By this point the atoms are in the steady state to a very good approximation [79].

Another approximation made is that the atoms are stationary, but in fact their motion will cause a Doppler shift of the resonant frequency. Also this result is only valid for an ensemble of non-interacting two-level atoms. For alkali-metal atoms, this assumption of two-levels is not good. Hyperfine splitting and Zeeman sub-levels mean that there are many transitions which can be driven by a single frequency of the light. Also we may have a mixture of different atoms, such as different isotopes. However, this two-level atom result can be generalized to include all these effects, as will be shown in the next two sections.

2.3.2 The electric susceptibility for a multi-level atom

A full description of the multi-level atom is quite complicated since the number of coupled optical Bloch equations becomes very large. Also, taking the steady-state solution to the optical Bloch equations actually becomes invalid, since slow processes such as off-resonant optical pumping mean that the atoms have not reached the steady state even for the $> 40\,\tau$ time they spend in the beam. The distribution of beam crossing times must now be taken into account, which will be different for different laser beam geometries and sizes. This is a more complicated problem but solvable [85, 86]. However, we can drastically simplify this problem by again restricting ourselves to a weak beam. In this context, the beam is 'weak' enough such that optical pumping does not occur for the amount of time the atoms spend in the beam [87, 88]. This means that we can treat an ensemble of multi-level atoms as a mixture of two-level atoms where their single transition corresponds to the same strength and frequency that occurs in the multi-level atom. There-

fore we can re-write equations (2.20a) & (2.20b) for a single transition i as

$$\chi_i(\Delta_i) = \frac{C_i^2 d^2 \mathcal{N}_a}{\epsilon_0 \hbar} f(\Delta_i) \tag{2.22a}$$

$$f(\Delta_i) = \frac{\mathrm{i}}{\Gamma/2 - \mathrm{i}\Delta_i}, \tag{2.22b}$$

where C_i^2 is the relative strength factor of the transition (see section 2.3.5), d is the reduced dipole matrix element which represents the strength of the atomic transition if no fine or hyperfine structure were present. Note that equation (2.21) can be modified to calculate d (see [89]). Also, because different transitions occur at different energies we write the detuning as $\Delta_i \equiv \omega - \omega_i$ where ω_i is the resonance angular frequency of transition i. Recall that $\mathcal{N}_a$ is the number density of identical atoms, and can be calculated from the elemental number density $\mathcal{N}$ (see B.1) by the following equation,

$$\mathcal{N}_a = \frac{F_a \mathcal{N}}{2(2\mathcal{I}+1)}, \tag{2.23}$$

where F_a is the isotopic fraction and $\mathcal{I}$ the nuclear spin quantum number. The denominator, $2(2\mathcal{I}+1)$, is the number of states in the ground manifold since we expect the atoms to be distributed evenly among all these states. We can justify this by noting that we expect the population of atomic states to follow a Boltzmann distribution [90]. By calculating the Boltzmann factor, which represents the fraction of atoms in a higher state (N_2) relative to a lower state (N_1), we can calculate how much the population of each state will deviate from uniform. The Boltmann factor is given by [90]

$$\frac{N_2}{N_1} = \exp\left(\frac{E_1 - E_2}{k_\mathrm{B} T}\right), \tag{2.24}$$

where k_B is the Boltzmann constant, T is the thermodynamic temperature and E_1 and E_2 are the energies of the lower and upper state respectively. The largest deviation will be given for high magnetic fields and low temperatures. Considering the ground manifold of ^{87}Rb, at our largest achievable magnetic field of 6200 G and lowest temperature of 20°C, the two states with the largest energy difference give a Boltzmann factor of 0.997. The assumption

of zero population in the excited manifolds is again justified by calculating the Boltzmann factor which shows the population is of the order of 10^{-13}. Note that when not in the weak-probe regime, hyperfine pumping will occur and redistribute populations [87, 88].

The real and imaginary parts of χ_i are plotted as a function of Δ_i in panel (i) of figure 2.1. The decay rate, Γ, is also the full width half maximum of the imaginary part of χ_i (a Lorentzian distribution). Γ has contributions from natural broadening (Γ_0), dipole-dipole induced self broadening [91] (Γ_{self}), and any extra homogeneous broadening e.g. pressure broadening due to buffer gasses (Γ_{buf}).

2.3.3 Including the Doppler effect

The centre of the complex line-shape occurs at the resonance frequency, however, due to motion the Doppler effect causes the atom to observe a shifted frequency. A thermal ensemble of atoms has a Gaussian distribution of velocities in the light propagation direction, given by [92]

$$g(v) = \frac{1}{U\sqrt{\pi}} \exp\left(-\frac{v^2}{U^2}\right), \tag{2.25}$$

where v is the component of velocity of the atom in the light propagation direction and U is the root mean square (rms) speed of the atoms, given by $U = \sqrt{2k_{\text{B}}T/m}$, where m is the mass of the atom. The resulting atomic line-shape ($\mathcal{V}$) is given by a convolution between f and g. Therefore, equations (2.22a) & (2.22b) are generalized to

$$\chi_i(\Delta_i) = \frac{C_i^2 d^2 \mathcal{N}_a}{\epsilon_0 \hbar} \mathcal{V}(\Delta_i) \tag{2.26a}$$

$$\mathcal{V}(\Delta_i) = \int_{-\infty}^{\infty} f(\Delta - kv) g(v) \mathrm{d}v. \tag{2.26b}$$

Panel (ii) of figure 2.1 shows the line-shape of χ_i when we include Doppler broadening at 20 °C. It is again important for the atom-light interaction to be in the weak-probe regime or deviations from this line-shape will be seen [85, 93]. Further deviations can also occur for large amounts of buffer gasses or short length cells due to Dicke narrowing [94]. These effects are

beyond the scope of this work, but studies including them can be found in [80].

To calculate the total susceptibility we add the contribution from all transitions ($\chi = \sum_i \chi_i$). We then write the susceptibility in terms of a global detuning, Δ, which is the frequency relative to a global linecentre. For convenience we have chosen zero detuning to occur at the weighted linecentre for D_1 ($n^2S_{1/2} \rightarrow n^2P_{1/2}$) and D_2 ($n^2S_{1/2} \rightarrow n^2P_{3/2}$) transitions (see B.2) where $n = 3, 4, 5$ or 6 for sodium, potassium, rubidium or caesium, respectively. We now look at using an atomic Hamiltonian to calculate the frequencies of the transitions relative to the linecentre as well as their strengths.

2.3.4 The atomic Hamiltonian

The atomic Hamiltonian is written as a sum of interaction mechanisms,

$$H = H_0 + H_\mathrm{f} + H_\mathrm{hf} + H_\mathrm{Z}, \tag{2.27}$$

where H_0 is the coarse atomic energy and H_f, H_hf and H_Z are the fine, hyperfine and external magnetic field interactions respectively. The fine structure interaction can be written as

$$H_\mathrm{f} = \frac{\gamma_\mathrm{f}}{\hbar^2} \left(\boldsymbol{L} \cdot \boldsymbol{S} \right), \tag{2.28}$$

where $\boldsymbol{L}$ and $\boldsymbol{S}$ are the orbital and spin angular momenta of the valence electron respectively, and γ_f is the spin-orbit constant for the particular atom. The hyperfine interaction has contributions from the magnetic dipole interaction, H_d, and electric quadrupole interaction, H_q, ($H_\mathrm{hf} = H_\mathrm{d} + H_\mathrm{q}$). We have omitted higher order multi-pole interactions since their effect is small ($\Delta E/h < 1\,\mathrm{kHz}$ [95]). The magnetic dipole interaction can be written as [83]

$$H_\mathrm{d} = \frac{A_\mathrm{hf}}{\hbar^2} \left(\boldsymbol{\mathcal{I}} \cdot \boldsymbol{J} \right), \tag{2.29}$$

where A_hf is the magnetic dipole constant, and $\boldsymbol{\mathcal{I}}$ and $\boldsymbol{J}$ are the nuclear spin and total electron ($\boldsymbol{J} = \boldsymbol{L} + \boldsymbol{S}$) angular momenta respectively. Using the convention that the magnitude of an arbitrary angular momentum $\boldsymbol{K}$ is

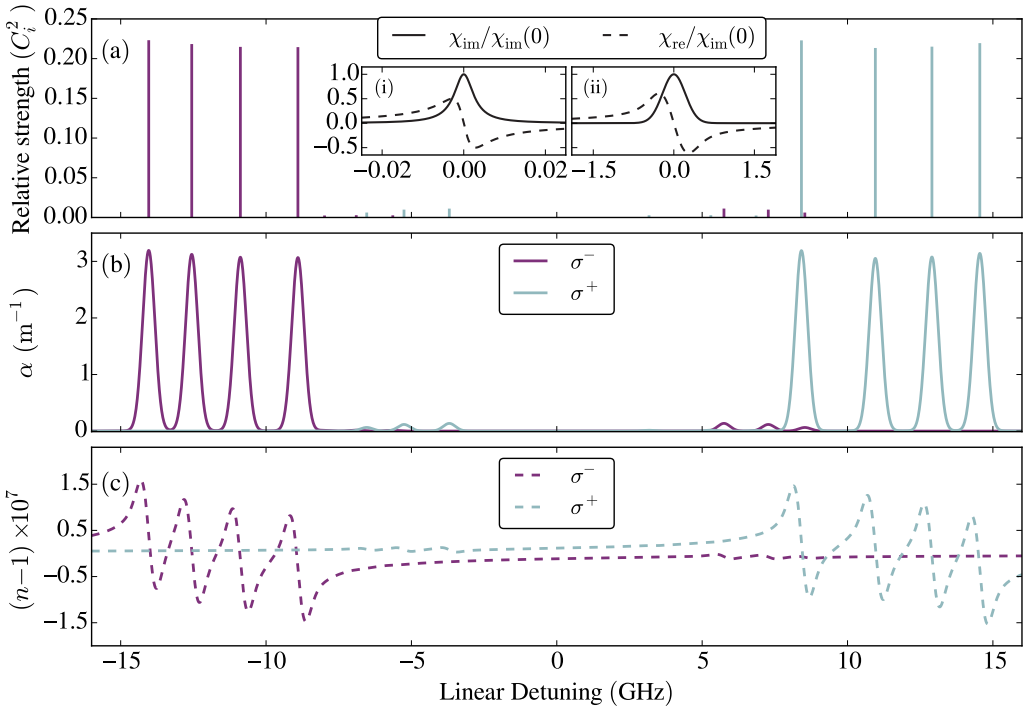

Figure 2.1: Graphs showing how the refractive indices and attenuation coefficients are found as a function of global detuning ($\Delta/2\pi$). Panel (a) is a stick spectrum showing the transition frequencies and strengths which are calculated from finding the eigenenergies and eigenvectors of the Hamiltonian of ^{87}Rb in a 6 kG magnetic field. An energy-level diagram corresponding to the 8 strong transitions is shown in figure 2.2. Inset (i) of panel (a) shows the Doppler-free complex lineshape profile for ^{87}Rb on the D_1 line (795 nm). Doppler broadening is added by convolving the lineshapes in (i) with a Gaussian resulting in the lineshapes given in (ii), (both insets are normalized to the peak of their respective imaginary part). For this example the Gaussian distribution was calculated for a temperature of 20° C. The lineshapes in (ii) are then simply added to the spectrum at the position of the transitions multiplied by their strength. This yields the attenuation coefficient shown in panel (b) or the refractive index shown in panel (c).

$\sqrt{K(K+1)}\hbar$, the electric quadrupole interaction can be written as [83]

$$H_{\mathrm{q}} = \frac{B_{\mathrm{hf}}}{\hbar^4}\left[\frac{3(\boldsymbol{\mathcal{I}}\cdot\boldsymbol{J})^2 + \frac{3}{2}(\boldsymbol{\mathcal{I}}\cdot\boldsymbol{J})\hbar^2 - \mathcal{I}(\mathcal{I}+1)J(J+1)\hbar^4}{2\mathcal{I}(2\mathcal{I}-1)J(2J-1)}\right], \tag{2.30}$$

where B_{hf} is the electric quadrupole constant. See B.2 for values for A_{hf} and B_{hf}. The interaction with an external magnetic field is given as[3]

$$H_{\mathrm{Z}} = \frac{\mu_{\mathrm{B}}}{\hbar}\left(g_L\boldsymbol{L} + g_S\boldsymbol{S} + g'_{\mathcal{I}}\boldsymbol{\mathcal{I}}\right)\cdot\boldsymbol{B}, \tag{2.31}$$

where μ_{B} is the Bohr magneton, and g_L, g_S and $g'_{\mathcal{I}}$ are the g-factors corresponding to the electron orbital, electron spin and nuclear[4] angular magnetic moments. g_L is taken to be 1; the values for the other g-factors are given in B.2. If we choose our quantization axis to be parallel to the magnetic field, equation 2.31 reduces to

$$H_{\mathrm{Z}} = \frac{\mu_{\mathrm{B}}}{\hbar}\left(g_L L_z + g_S S_z + g'_{\mathcal{I}}\mathcal{I}_z\right)B_z. \tag{2.32}$$

Once the Hamiltonian is constructed, we need to find the eigenenergies, E_j, and corresponding eigenstates, $|j\rangle$, in order to calculate the transition energies and strengths. The transition energy is simply the difference in energy between the ground and excited states ($E_{\mathrm{e}} - E_{\mathrm{g}}$).

2.3.5 Calculating transition strengths from the eigenstates

The eigenstates will be given by some combination of completely uncoupled basis states $|L, m_L, m_S, m_{\mathcal{I}}\rangle$, where m_L, m_S and $m_{\mathcal{I}}$ are the z-projection quantum numbers. Transition strengths are given by the electric dipole matrix element squared, $|\langle \mathrm{g}|er_q|\mathrm{e}\rangle|^2$, where er_q is the component of the dipole operator in the spherical basis (see equation 5.17 in [96]); this chooses whether the transition is σ^+, σ^- or π ($\Delta m_L = -q$ where $q = -1, +1$ or 0 respectively). To illustrate how the strength is calculated, we take the example of

[3] We have ignored the quadratic (diamagnetic) term in $\boldsymbol{B}$ [83] since it should be negligible for the low principle quantum numbers and magnetic fields [26] used in this thesis.

[4] The nuclear g-factor is written with a prime here since commonly $g_{\mathcal{I}}$ is defined with the product $g_{\mathcal{I}}\mu_{\mathcal{I}}$, where $\mu_{\mathcal{I}}$ is the nuclear magneton.

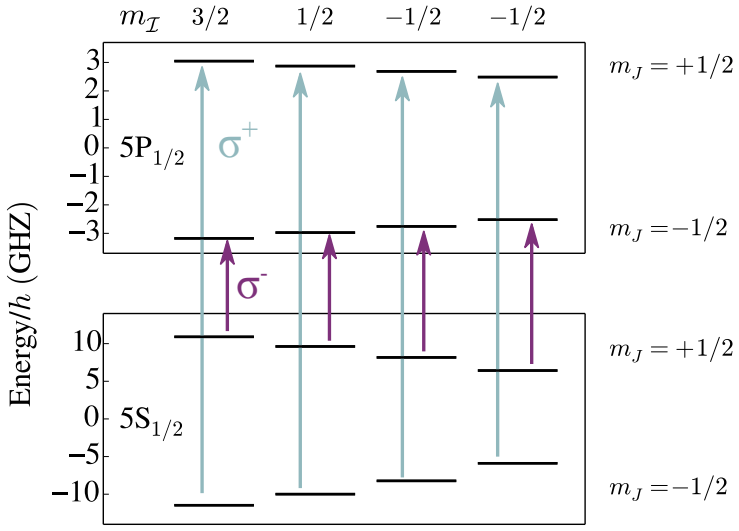

Figure 2.2: Energy levels for the D_1 line for a rubidium-87 atom in a 6 kG magnetic field. The energy levels are labelled by the quantum numbers which dominate the eigenstate in the hyperfine Paschen-Back regime. The 8 transitions correspond to the strong ones shown in figure 2.1, with shorter arrows corresponding to transitions occurring at lower frequency. The arrow lengths are not to scale with the transition frequency. See equation (3.29) in section 3.3.2 for precise details of how the energy levels are calculated.

a σ^- transition between the eigenstates

$$|g\rangle = a_1 \left|0, 0, +1/2, -1/2\right\rangle + a_2 \left|0, 0, -1/2, +1/2\right\rangle \tag{2.33}$$

$$\begin{aligned} |e\rangle = {} & b_1 \left|1, -1, +1/2, -1/2\right\rangle + b_2 \left|1, +1, -1/2, -3/2\right\rangle \\ & + b_3 \left|1, 0, -1/2, -1/2\right\rangle + b_4 \left|1, 0, +1/2, -3/2\right\rangle \end{aligned} \tag{2.34}$$

where a_1, a_2, b_1, b_2, b_3 and b_4 are parameters which are known after finding the eigenenergies and eigenstates of the Hamiltonian. Note that this choice of eigenstates is analogous to the $|1, 0\rangle \rightarrow |1, -1\rangle$, D_1 transition, in the $|F, m_F\rangle$ coupled basis[5] in rubidium-87. The transition strength will be given by

$$\left|\langle \mathrm{g} \left| er_1 \right| \mathrm{e} \rangle\right|^2 = a_1^2 b_1^2 \left|\langle 0, 0, +1/2, -1/2 \left| er_1 \right| 1, -1, +1/2, -1/2 \rangle\right|^2 . \tag{2.35}$$

All other terms are zero since the er_1 operator can only couple states where the excited m_L quantum number is reduced by one and all other quantum numbers are the same. Since only the orbital angular momentum of the

[5]The coupled basis angular momentum is defined as $F = I + L + S$ and m_F is its projection on the quantization axis which we have defined as the z-axis.

electron is changed during an electric dipole transition, we can decouple the transition into angular and spin parts,

$$|\langle \mathrm{g}\,|er_q|\,\mathrm{e}\rangle|^2 = a_1^2 b_1^2\,|\langle L, m_L\,|er_q|\,L', m_{L'}\rangle\,\langle m_S, m_{\mathcal{I}}|\,m_{S'}, m_{\mathcal{I}'}\rangle|^2\,, \tag{2.36}$$

where symbols with a prime denote the excited state quantum number. The last part in equation (2.36) ensures that the only non-zero result comes when the electron spin and nuclear spin remain unchanged. Using the Wigner-Eckart theorem [96] we can reduce the angular part,

$$|\langle L, m_L\,|er_q|\,L', m_{L'}\rangle|^2 = \begin{pmatrix} L & 1 & L' \\ -m_L & q & m_{L'} \end{pmatrix}^2 \langle L||e\boldsymbol{r}||L'\rangle^2\,. \tag{2.37}$$

The symbol in brackets is a Wigner 3-j symbol [97]. When $L' = 1$ and $L = 0$, the square of the Wigner 3-j symbol is $1/3$ for any σ^+, σ^- or π transition. The double-bar matrix element, $\langle L||e\boldsymbol{r}||L'\rangle$, denotes the reduced dipole matrix element, d. Therefore, for our particular example the transition strength is simply,

$$|\,\langle \mathrm{g}\,|er_1|\,\mathrm{e}\rangle\,|^2 = \frac{1}{3} d^2 a_1^2 b_1^2 \equiv d^2 C_i^2. \tag{2.38}$$

Recalling equation (2.26a), we see how the strength fits in to the amplitude of the electric susceptibility for a single transition. For the general case we find the strength from $d^2/3$ multiplied by $\sum_{i,j} a_i^2 b_j^2$, where a_i and b_i are the coefficients of two basis states which are allowed to couple by the selection rules.

See section 3.3.2 for details of how this strength factor is calculated using a matrix representation of the Hamiltonian. Note that only the case where the magnetic field is parallel to the propagation axis of the light is considered. In this case π transitions are forbidden [83].

Figure 2.1 shows an example for the rubidium D_1 line, showing the result of adding the lineshape at each transition frequency, scaled by the relative transition strength. A large magnetic field was simulated which separates the individual transitions for clarity. Figure 2.2 shows the corresponding energy-level diagram.

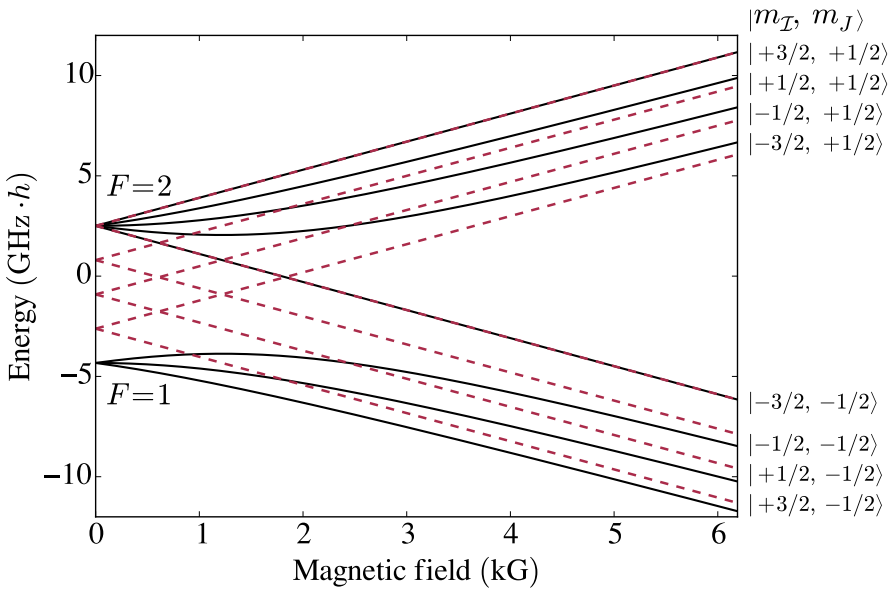

Figure 2.3: Energy levels of the $5^2S_{1/2}$ manifold of ^{87}Rb as a function of magnetic field. The solid back lines show the energy levels calculated after finding the eigenvalues of the atomic Hamiltonian. The dashed red lines show the approximation given by equation (2.39). At low magnetic fields the states group into $F = 1$ or 2. On the right of the plot each eigenstate is labelled with the basis state which dominates it's composition at high magnetic fields.

2.4 Phenomena arising from application of an external magnetic field

Using the model described in the previous sections, we will discuss two phenomena that emerge from applying a magnetic field: the hyperfine Paschen-Back regime and the Faraday effect.

2.4.1 Magnetic field regimes: the emergence of the hyperfine Paschen-Back regime

From analysis of the atomic Hamiltonian as a function of applied magnetic field we can see that the behaviour of the energy levels can be separated into three separate regimes. Further discussion of these regimes is given in [83]. Here we briefly describe them.

Figure 2.3 shows the energy levels of the ground manifold of ^{87}Rb ($5^2S_{1/2}$) as a function of applied magnetic field. We can see that the magnetic field lifts

the degeneracy. At low magnetic fields the magnetic interaction causes a linear shift in the energy levels. This is because, when the magnetic interaction can be considered weak compared to the hyperfine interaction ($\mu_{\mathrm{B}}B \ll A_{\mathrm{hf}}$), all the angular momenta of the atom are coupled via their individual magnetic moments. This means the atom behaves as though it has one angular momentum, $\boldsymbol{F} = \boldsymbol{\mathcal{I}} + \boldsymbol{L} + \boldsymbol{S}$, with it's z-projection m_F. Therefore the energy shifts are linear ($\delta E \propto m_F \mu_{\mathrm{B}} B$). This is known as the hyperfine linear-Zeeman regime [26]. In this regime F and m_F are good quantum numbers since each eigenstate of the Hamiltonian can be predominantly described by a single F and m_F quantum number.

When the magnetic field is increased further the energy shifts of most states are no longer linear with magnetic field. This is due to the partial uncoupling of the angular momenta. In this 'intermediate' regime, their are no good quantum numbers.

At large magnetic fields, the linear shift of the energy levels is recovered. This is due to $\boldsymbol{I}$ and $\boldsymbol{J}$ having almost completely decoupled. This is known as the hyperfine Paschen-Back (HPB) regime [33]. In this regime m_I and m_J are good quantum numbers since each eigenstate of the Hamiltonian will now be predominantly described by a single m_I and m_J quantum number. At large magnetic fields the hyperfine interaction can be treated as a perturbation. As such we can approximate the energy of each state by using the following equation [96],

$$E = (g_J m_J + g'_{\mathcal{I}} m_{\mathcal{I}})\mu_{\mathrm{B}} B + A_{\mathrm{hf}} m_J m_{\mathcal{I}} + \frac{B_{\mathrm{hf}}}{4\mathcal{I}(2\mathcal{I}-1)J(2J-1)}[3m_J^2 - J(J+1)][3m_{\mathcal{I}}^2 - \mathcal{I}(\mathcal{I}+1)]. \tag{2.39}$$

It should be noted that B_{hf} is zero for states for which $J = 1/2$, and therefore the last term in equation (2.39) is only required when approximating the $P_{3/2}$ term energy levels. From figure 2.3 we can see that the energy levels asymptotically reach the result given by equation (2.39) at high magnetic fields. Figure 2.3 also shows that there are two exceptional states (known as stretched states) in which the eigenenergies of the Hamiltonian are completely described by equation (2.39) for all magnetic field values. The explanation for this is that these eigenstates can be expressed in a single basis state at all

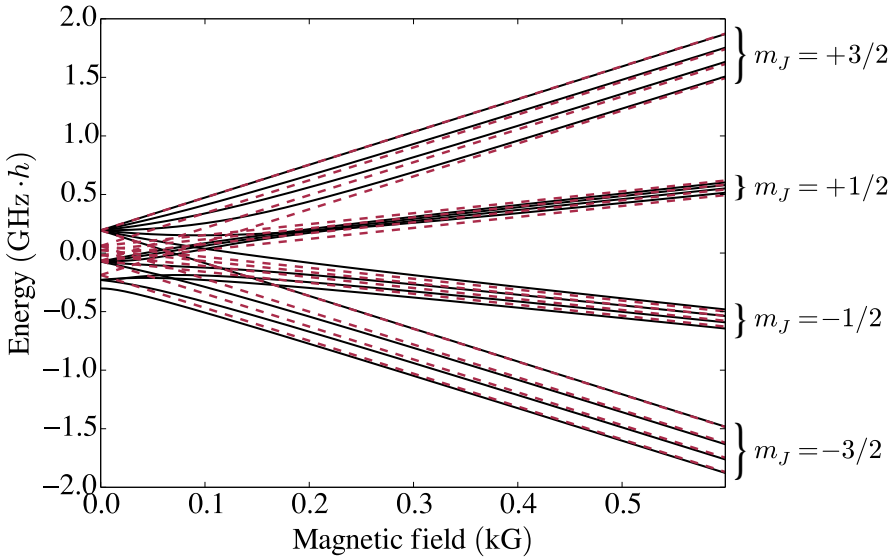

Figure 2.4: Energy levels of the $5^2P_{3/2}$ manifold of ^{87}Rb as a function of magnetic field. The solid back lines show the energy levels calculated after finding the eigenvalues of the atomic Hamiltonian. The dashed red lines show the approximation given by equation (2.39). The states can be grouped by the m_J quantum number shown on the right of the plot.

values of the magnetic field, and as such are perfectly described by a single set of quantum numbers.

Figure 2.4 shows the energy levels of the $5^2P_{3/2}$ manifold of ^{87}Rb. Again we calculate the energy levels from the eigenvalues of the atomic Hamiltonian and also by the approximation of equation (2.39). The behaviour is generally similar to that seen for the $5^2S_{1/2}$ manifold except that we enter the Paschen-Back regime at much lower values of the magnetic field. This is because the hyperfine interaction is much weaker for the $5^2P_{3/2}$ manifold. This is true in general for alkali-metal atoms; the ground manifold will always enter the HPB regime at the largest magnetic field.

For the model described here, equation (2.39) will well represent all the energy levels when the magnetic field becomes infinite. However, at some point the coupling between L and S will break down. At this point we enter what is known as the fine Paschen-Back regime [26], where the magnetic field interaction is much larger than the fine structure interaction. However, for the magnetic fields studied in this thesis we will not reach this regime and therefore our model should remain valid.

Atomic transitions in the HPB regime

Once both the excited manifold and the ground manifold are both in the HPB regime, we can see that the shifts of the atomic transitions should be predictably linear. Also, since the ground manifold of alkali-metal atoms will always enter the HPB regime at the largest magnetic field, we can say that optical transitions (or optical spectra) are in the HPB regime when the ground manifold is in the HPB regime.

To demonstrate this, the attenuation coefficient is plotted in figure 2.5 for increasing values of the magnetic field. At small and large magnetic field values the spectra are simple, and can be defined by good quantum numbers [26]. In these regimes, it may be sufficient to estimate frequency shifts by a perturbative treatment. However, in the intermediate regime there are no good quantum numbers, and neither the hyperfine interaction nor the magnetic interaction can be considered small. This shows the power of the Hamiltonian technique in being able to find transition frequencies and strengths accurately in all these regimes.

2.4.2 The Faraday effect

Our model considers the case of a medium where only $\sigma^{\pm}$ transitions are allowed. On application of a magnetic field the transition frequencies will be shifted and their strengths will be altered. This effect is different for σ^+ and σ^- transitions. Therefore the refractive indices for the polarizations that drive σ^+ and σ^- are different ($n^+ \neq n^-$). This is known as *circular birefringence* and it gives rise to the Faraday effect, which is the rotation of the plane of polarization of linearly polarized light as it propagates through a medium which has an axial magnetic field. This can be explained by noting that linearly polarized light can be thought of as being composed of equal amplitudes of left- and right-hand circularly polarized light. The differing refractive indices of the two in the optical medium mean that there will be a phase shift between the two circular components which will be observed as a rotation in the plane of linear polarization.

In addition to birefringence the magnetic field causes *circular dichroism*.

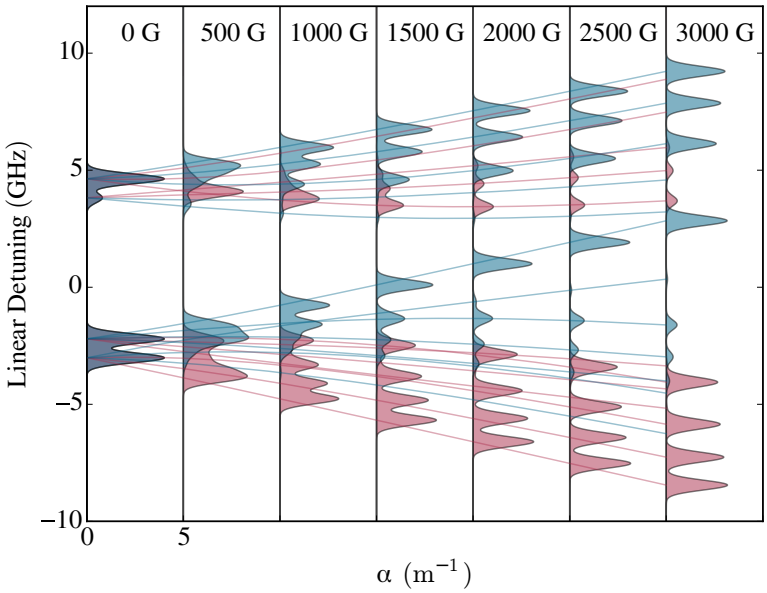

Figure 2.5: The attenuation coefficient as a function of linear detuning ($\Delta/2\pi$) for a ^{87}Rb vapour on the D_1 line (795 nm) and at a temperature of 20 °C. There are seven plots of the attenuation coefficient at magnetic field values ranging from 0 to 3000 G in increments of 500 G. Each plot is placed on its side, displaced to the right for clarity, with the attenuation coefficient ranging from 0 to 5 m^{-1} in each one. The area under each curve has been coloured either translucent red or blue, representing σ^- and σ^+ transitions. Overlaying the plots are curves showing the transition frequencies as a function of magnetic field. Notice that the strong σ^- transitions move to lower energies while the strong σ^+ ones move to higher energies. A video showing the evolution of the attenuation coefficients for a Caesium vapour is available from http://www.jqc.org.uk/research/project/elecsus/12683.

This is defined as the situation where the attenuation coefficients are different ($\alpha^+ \neq \alpha^-$). This will cause linearly polarized light to become elliptical. However, since refractive index curves fall to 1 (as $1/\Delta$) slower than attenuation falls to zero ($1/\Delta^2$), going off-resonance will cause the dispersion to dominate over attenuation. Therefore, it is possible to observe large rotations of linearly polarized light with little ellipticity generated [47]. When the attenuation is low, the plane of polarization rotates by the angle [46],

$$\theta = \frac{1}{2}(n_+ - n_-)k\ell. \tag{2.40}$$

Therefore we can say that the Faraday effect is a good probe of the differential dispersion ($n_+ - n_-$).

Figure 2.5 quite clearly shows that the atomic medium in the HPB regime exhibits a large amount of dichroism, where the σ^+ and σ^- transitions become completely separated. This gives rise to further phenomena which we will investigate in detail in chapter 5.

2.5 Discussion

A model for the weak-probe electric susceptibility of an atomic ensemble has been described. The next chapter will describe a computational implementation of this model. The method by which the model is implemented is not trivial. A program which runs quickly is essential for practical computerized optimization which is used extensively in this thesis.

Chapter 3

ElecSus: A program to calculate the electric susceptibility of an atomic ensemble

3.1 Introduction

Most applications of atomic vapours benefit from being able to predict the attenuation and dispersion (in absolute measures) of the medium. In chapter 2 we saw how the electric susceptibility is key in calculating these properties; here we present a fast, and easy to use, computer program utilizing the model described in chapter 2, that can be used to predict the attenuation and dispersion given certain parameters. This facilitates designing optical devices, such as Faraday filters [53, 54, 67, 98, 99] and optical isolators [29], without resorting to experimental trial and error. Also, since each theory curve will typically take less than a second to compute, fitting experiment to theory becomes practical. This allows experimental parameters to be measured efficiently. This has applications for optical magnetometry [100], optical thermometry [101–103], number density measurements in optically thick vapour [13, 104], and diagnostics for devices such as vacuum dispensers [105–107] and vapour cells [22–24, 108, 109].

In principle, programs could be constructed for any gas, but here we focus on alkali-metal vapours. Extensions to the case of molecular gases are also of interest [110].

3.2 The Stokes parameters

The electric susceptibility is not a directly measurable quantity. To compare theory and experiment the most convenient place to meet is the Stokes parameters. These are easily measured experimentally, and easily calculated theoretically, from the electric susceptibility.

This section is concerned with finding how to calculate the Stokes parameters for arbitrarily polarized light that has passed through a circularly birefringent and dichroic medium.

Together, the four Stokes parameters characterize the polarization state of light [111]. They are measurable with linear optics and photodetectors [112], and are therefore a convenient way to measure the polarization of light. However, the Stokes parameters have uses beyond measuring polarization. Predicting their spectral dependence for an atomic medium is useful since they can be used for several optical devices. The S_0 parameter, equivalent to transmission, can be used for primary thermometry [101]. The S_1 and S_2 parameter signals can be used as far off-resonance laser-frequency stabilising references [44], while the S_3 signal is the dichroic atomic vapour laser lock [113, 114] error signal. The Stokes parameters are defined as

$$S_0 \equiv (I_- + I_+)/I_0 \tag{3.1a}$$
$$= (I_x + I_y)/I_0 \tag{3.1b}$$
$$= (I_{\nearrow} + I_{\searrow})/I_0 \tag{3.1c}$$
$$S_1 \equiv (I_x - I_y)/I_0 \tag{3.1d}$$
$$S_2 \equiv (I_{\nearrow} - I_{\searrow})/I_0 \tag{3.1e}$$
$$S_3 \equiv (I_- - I_+)/I_0, \tag{3.1f}$$

where I_x and I_y are the intensities of light that are transmitted and reflected, respectively, at a polarizing beam-splitter placed after the medium; this de-

fines the x- and y-axes. The symbols $I_{\nearrow}$ and $I_{\searrow}$ denote the intensities of light after the medium, which are polarized at an angle that deviates from the x-axis by $45°$ and $-45°$ respectively, while I_- and I_+ represent the intensities of light which drive $\sigma^{\pm}$ transitions. I_0 is the initial intensity of light just after entering the medium.

3.2.1 Jones Calculus in the circular basis

Jones calculus is a well known way of calculating the polarization state of a coherent beam of light [115]. The Jones vectors and matrices in the linear basis can simply be looked up in books [116], and are generally preferred since optical elements such as polarizers tend to filter linear components of polarization. Since our medium is circularly birefringent and dichroic, it is more convenient to work in the circular basis. First we need to find the transformation matrix $\hat{U}$, and then use this to convert the vectors and matrices given in the linear basis to the circular basis. Using the Jones vectors in the linear basis (given in table 3.1), we find $\hat{U}$ by,

$$\hat{U} = \begin{bmatrix} \boldsymbol{J}_-^\dagger \cdot \boldsymbol{J}_x & \boldsymbol{J}_-^\dagger \cdot \boldsymbol{J}_y \\ \boldsymbol{J}_+^\dagger \cdot \boldsymbol{J}_x & \boldsymbol{J}_+^\dagger \cdot \boldsymbol{J}_y \end{bmatrix} \tag{3.2}$$

$$= \frac{1}{\sqrt{2}} \begin{bmatrix} 1 & -i \\ 1 & i \end{bmatrix}. \tag{3.3}$$

The vectors in the circular basis are then given by $\hat{U}$ acting on the vectors in the linear basis. The result is given in table 3.1. To change the Jones matrices (which describe optical elements) into the circular basis we use $\hat{U}\hat{A}\hat{U}^\dagger$, where $\hat{A}$ is the matrix in the linear basis. The Jones matrices for polarizers can be found in table 3.2.

Linear basis	Circular basis
$\boldsymbol{J}_x = \begin{bmatrix}1\\0\end{bmatrix}$	$\boldsymbol{J}_- = \begin{pmatrix}1\\0\end{pmatrix}$
$\boldsymbol{J}_y = \begin{bmatrix}0\\1\end{bmatrix}$	$\boldsymbol{J}_+ = \begin{pmatrix}0\\1\end{pmatrix}$
$\boldsymbol{J}_R = \frac{1}{\sqrt{2}}\begin{bmatrix}1\\-i\end{bmatrix}$	$\boldsymbol{J}_x = \frac{1}{\sqrt{2}}\begin{pmatrix}1\\1\end{pmatrix}$
$\boldsymbol{J}_L = \frac{1}{\sqrt{2}}\begin{bmatrix}1\\i\end{bmatrix}$	$\boldsymbol{J}_y = \frac{1}{\sqrt{2}}\begin{pmatrix}-i\\i\end{pmatrix}$
$\boldsymbol{J}_\nearrow = \frac{1}{\sqrt{2}}\begin{bmatrix}1\\1\end{bmatrix}$	$\boldsymbol{J}_\nearrow = \frac{1}{2}\begin{pmatrix}1-i\\1+i\end{pmatrix}$
$\boldsymbol{J}_\searrow = \frac{1}{\sqrt{2}}\begin{bmatrix}1\\-1\end{bmatrix}$	$\boldsymbol{J}_\searrow = \frac{1}{2}\begin{pmatrix}1+i\\1-i\end{pmatrix}$

Table 3.1: Jones vectors for horizontal ($\boldsymbol{J}_x$), vertical ($\boldsymbol{J}_y$), circular driving σ^+ ($\boldsymbol{J}_+$), circular driving σ^- ($\boldsymbol{J}_-$), linear +45° ($\boldsymbol{J}_\nearrow$) and linear -45° ($\boldsymbol{J}_\searrow$) light.

Optical element	Linear basis	Circular basis
Horizontal linear polarizer ($\hat{P}_x$)	$\begin{bmatrix}1&0\\0&0\end{bmatrix}$	$\frac{1}{2}\begin{pmatrix}1&1\\1&1\end{pmatrix}$
Vertical linear polarizer ($\hat{P}_y$)	$\begin{bmatrix}0&0\\0&1\end{bmatrix}$	$\frac{1}{2}\begin{pmatrix}1&-1\\-1&1\end{pmatrix}$
Linear polarizer at +45° ($\hat{P}_\nearrow$)	$\frac{1}{2}\begin{bmatrix}1&1\\1&1\end{bmatrix}$	$\frac{1}{2}\begin{pmatrix}1&-i\\i&1\end{pmatrix}$
Linear polarizer at -45° ($\hat{P}_\searrow$)	$\frac{1}{2}\begin{bmatrix}1&-1\\-1&1\end{bmatrix}$	$\frac{1}{2}\begin{pmatrix}1&i\\-i&1\end{pmatrix}$

Table 3.2: Jones matrices for polarizers.

3.2.2 Calculating the Stokes parameters for a circularly birefringent and dichroic medium

We start by writing the initial polarization of the light as a Jones vector in the circular basis,

$$\boldsymbol{E}_0 = E_{0,-}e^{i\phi_{0,-}}\boldsymbol{J}_- + E_{0,+}e^{i\phi_{0,+}}\boldsymbol{J}_+, \tag{3.4}$$

$$= \begin{pmatrix} E_{0,-}e^{i\phi_{0,-}} \\ E_{0,+}e^{i\phi_{0,+}} \end{pmatrix}. \tag{3.5}$$

Here $E_{0,-}$ and $E_{0,+}$ are the amplitudes of the electric field in the left and right polarized components respectively, and $\phi_{0,-}$ and $\phi_{0,+}$ are their initial phases. Since we only need to maintain information about the difference in phases between the left and right components, we can set $\phi_{0,-} = 0$ and write $\boldsymbol{E}_0$ in terms of the phase difference $\phi_0 = \phi_{0,+} - \phi_{0,-}$,

$$\boldsymbol{E}_0 = \begin{pmatrix} E_{0,-} \\ E_{0,+}e^{i\phi_0} \end{pmatrix}, \tag{3.6}$$

Note that we can use equation (2.5) to find the total initial intensity [116],

$$I_0 = \frac{c\epsilon_0}{2}\boldsymbol{E}_0^\dagger \cdot \boldsymbol{E}_0. \tag{3.7}$$

Note further that the constants in front of $\boldsymbol{E}_0^\dagger \cdot \boldsymbol{E}_0$ are not important for our calculation since they will cancel out, which can be seen in the definition of the Stokes parameters. Then we apply the effect of the medium as both the effect of attenuation ($\hat{D}$) and a phase shift ($\hat{B}$) to find the electric field after the cell ($\boldsymbol{E}$),

$$\boldsymbol{E} = \hat{B}\hat{D}\boldsymbol{E}_0, \tag{3.8}$$

$$= \begin{pmatrix} e^{in_-k\ell} & 0 \\ 0 & e^{in_+k\ell} \end{pmatrix} \begin{pmatrix} e^{-\frac{1}{2}\alpha_-\ell} & 0 \\ 0 & e^{-\frac{1}{2}\alpha_+\ell} \end{pmatrix} \begin{pmatrix} E_{0,-} \\ E_{0,+}e^{i\phi_0} \end{pmatrix}, \tag{3.9}$$

$$= \begin{pmatrix} E_{0,-}e^{i(n_-k\ell)}e^{-\frac{1}{2}\alpha_-\ell} \\ E_{0,+}e^{i(n_+k\ell+\phi_0)}e^{-\frac{1}{2}\alpha_+\ell} \end{pmatrix} \equiv \begin{pmatrix} E_- \\ E_+ \end{pmatrix}, \tag{3.10}$$

recalling that ℓ is the length of the medium, and n and α denote the refractive index and attenuation coefficient, and the $-$ and $+$ subscripts refer to circular polarizations which drive σ^- and σ^+ respectively. Note that the factor of $1/2$ before the attenuation coefficient which arises due to the fact that electric field is proportional to the square root of intensity, and the attenuation coefficient is defined with respect to intensity.

We now need to find the intensity of light polarized in all six components (horizontal, vertical, $+45°$, $-45°$, left and right) in order to construct the Stokes parameters. The left and right circular components of intensity are simple to find since we have worked in the circular basis,

$$I_- = \frac{c\epsilon_0}{2} E_-^* E_- \tag{3.11}$$

$$I_+ = \frac{c\epsilon_0}{2} E_+^* E_+. \tag{3.12}$$

To find the other polarizations we need first apply the corresponding polarizer (in the circular basis) to $\boldsymbol{E}$,

$$\boldsymbol{E}_x = \hat{P}_x \boldsymbol{E} \tag{3.13}$$

$$= \frac{1}{2} \begin{pmatrix} E_- + E_+ \\ E_- + E_+ \end{pmatrix} \tag{3.14}$$

$$\boldsymbol{E}_y = \hat{P}_y \boldsymbol{E} \tag{3.15}$$

$$= \frac{1}{2} \begin{pmatrix} E_- - E_+ \\ -E_- + E_+ \end{pmatrix} \tag{3.16}$$

$$\boldsymbol{E}_\nearrow = \hat{P}_\nearrow \boldsymbol{E} \tag{3.17}$$

$$= \frac{1}{2} \begin{pmatrix} E_- - iE_+ \\ iE_- + E_+ \end{pmatrix} \tag{3.18}$$

$$\boldsymbol{E}_\searrow = \hat{P}_\searrow \boldsymbol{E} \tag{3.19}$$

$$= \frac{1}{2} \begin{pmatrix} E_- + iE_+ \\ -iE_- + E_+ \end{pmatrix}. \tag{3.20}$$

The corresponding intensities are found from equation (3.7). It is useful to define a quantity (p) representing the proportion of the light before the

medium that drives σ^- transitions,

$$p \equiv \frac{|E_{0,-}|^2}{|E_{0,-}|^2 + |E_{0,+}|^2}. \tag{3.21}$$

We can now write the Stokes parameters in terms of p and the attenuation coefficients, $\alpha^{\pm}$, and refractive indices $n^{\pm}$,

$$S_0 = p\exp\left(-\alpha_-\ell\right) + (1-p)\exp\left(-\alpha_+\ell\right), \tag{3.22a}$$

$$S_1 = 2\sqrt{p-p^2}\cos\left(2\psi\right)\exp\left[-\frac{1}{2}\left(\alpha_- + \alpha_+\right)\ell\right], \tag{3.22b}$$

$$S_2 = 2\sqrt{p-p^2}\sin\left(2\psi\right)\exp\left[-\frac{1}{2}\left(\alpha_- + \alpha_+\right)\ell\right], \tag{3.22c}$$

$$S_3 = p\exp\left(-\alpha_-\ell\right)) - (1-p)\exp\left(-\alpha_+\ell\right)), \tag{3.22d}$$

$$\psi = \frac{1}{2}(n_+ - n_-)k_0\ell + \theta_0, \tag{3.22e}$$

where $\theta_0 = \phi_0/2$. For linearly polarized light incident on the medium, θ_0 represents the angle the plane of polarization makes with the x-axis. The parameters p and θ_0 are enough to characterize the initial polarization state of a coherent laser beam.

We can also calculate the individual I_x and I_y spectra using the definitions (3.1b) and (3.1d),

$$I_x = (S_0 + S_1)/2, \tag{3.23}$$

$$I_y = (S_0 - S_1)/2. \tag{3.24}$$

These spectra are useful since they correspond to Faraday filtering [53, 54, 67, 98, 99].

3.3 Program structure

This section outlines the structure of the ElecSus program as well as giving details about how the key components of the program work. The program is centred on the `elecsus.py` module. This module takes the user-specified parameters and settings from the run card, imports the `spectrum` function

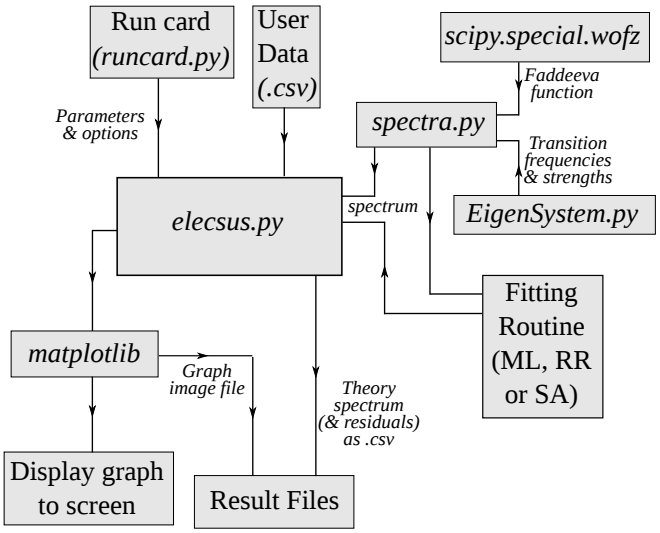

Figure 3.1: The flow of information in the ElecSus program.

and uses it to generate the spectrum, or imports the fitting modules which fit user data to curves generated by `spectrum`. Experimental data supplied by the user should be as a two-column comma separated values (csv) file; the first column specifies linear detuning in units of GHz while the second is the corresponding value for the spectrum. csv files are readable by spreadsheet programs and are a common data output format on digital storage oscilloscopes. The program then creates a new sub-directory for the output files. It writes the main result to a csv file named by the user-specified label suffixed by `_theory.csv`. If requested in the run card, the module also uses `matplotlib` [117] to plot the curve and display it to the screen; there is also an option to save the plot to a file. If a fit was performed the module will also save the residuals [118] of data and theory curves as a csv file, as well as output the fit parameters to a file suffixed by `_Parameters.txt`. Figure 3.1 shows a flowchart of the program structure.

3.3.1 Global lineshape profile

In section 2.3.3 we saw that calculating the atomic line-shape, $\mathcal{V}(\Delta_i)$, can be done by performing a convolution. However, the result is related to the

Faddeeva function, $w(\zeta)$,

$$\mathcal{V}(\Delta_i) = \frac{\mathrm{i}\sqrt{\pi}}{k_0 U} w(\zeta), \tag{3.25}$$

$$\zeta = \frac{\mathrm{i}}{2}\frac{\Gamma}{k_0 U} + \frac{\Delta_i}{k_0 U}, \tag{3.26}$$

recalling that U is the rms speed of the atoms. Using a `scipy` implementation of the Faddeeva function (`scipy.special.wofz`), which is a wrapper for a fast algorithm written in C++ [119], ElecSus quickly calculates the line-shape. Calculating the global line-shape must be done with care since an inefficient implementation can be slow. The line-shape should be the same for all transitions of the same atom and so the `wofz` function only needs to be called once per isotope. Isotopes of the same element will also have a slightly different line-shape because the different masses provide a different Doppler broadening. The appropriate line-shape profile is then added to the spectrum for each transition with a shift given by the transition detuning and an amplitude proportional to its line-strength.

3.3.2 Matrix representation of the atomic Hamiltonian

For each atomic term ($\mathrm{n}^2\mathrm{S}_{1/2}$ and $\mathrm{n}^2\mathrm{P}$) a separate Hamiltonian is built up in a similar manner as described in section 2.3.4 as a matrix in the completely uncoupled basis. Each matrix is of size $D_{LS\mathcal{I}} \times D_{LS\mathcal{I}}$ where

$$D_{LS\mathcal{I}} = (2L+1)(2S+1)(2\mathcal{I}+1). \tag{3.27}$$

We set the coarse atomic energy to zero since we are simply looking for the detuning values from a global linecentre. For the $\mathrm{n}^2\mathrm{S}_{1/2}$ term $L = 0$, so there is no fine structure interaction. The Hamiltonian is therefore given by

$$\hat{H}_\mathrm{S} = \frac{A_\mathrm{hf}}{\hbar^2}(\boldsymbol{\mathcal{I}} \cdot \boldsymbol{J}) + \frac{\mu_\mathrm{B} B_z}{\hbar}\left(g_S \hat{S}_z + g'_\mathcal{I} \hat{\mathcal{I}}_z\right). \tag{3.28}$$

ElecSus calculates D_1 and D_2 spectra separately, however the full $\mathrm{n}^2\mathrm{P}$ term is calculated. The eigenenergies of the fine structure part of the Hamiltonian are $-\gamma_\mathrm{f}$ and $\gamma_\mathrm{f}/2$, but since we want to calculate detuning values from a

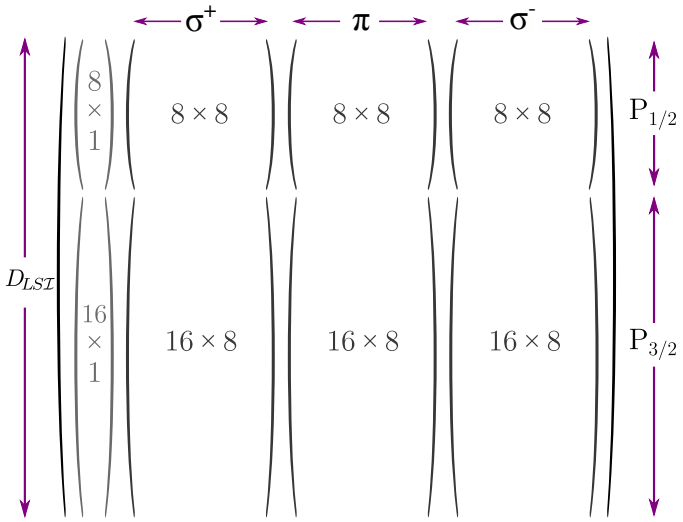

Figure 3.2: A schematic of the n^2P term matrix for ^{87}Rb obtained once diagonalized. The first column gives the eigenenergies which are added to the left of the matrix. The corresponding rows give the coefficients of the (completely uncoupled) basis states that make up the eigenstate. Certain parts of the matrix correspond to allowed final states for transitions, and so are post selected when finding transition strengths. In this case the sub-matrices are 8 by 8 for a D_1 transition and 16 by 8 for D_2. Adapted with permission from a figure in [120]

global linecentre we need to recentre this energy. We therefore calculate the Hamiltonian as

$$\hat{H}_{\mathrm{P}} = \frac{\gamma_{\mathrm{f}}}{\hbar^2}\left(\boldsymbol{L}\cdot\boldsymbol{S}\right) + \hat{H}_{hf} + \hat{H}_{\mathrm{Z}} + \begin{cases} \gamma_{\mathrm{f}} \otimes \mathbb{I}_{D_{LS\mathcal{I}}}, \text{for } \mathrm{n}^2\mathrm{P}_{1/2}, \\ -\gamma_{\mathrm{f}}/2 \otimes \mathbb{I}_{D_{LS\mathcal{I}}}, \text{for } \mathrm{n}^2\mathrm{P}_{3/2}, \end{cases} \tag{3.29}$$

where $\mathbb{I}_{D_{LS\mathcal{I}}}$ is the identity matrix. Figure 3.2 shows a schematic of the $\hat{H}_P$ matrix after it is diagonalized. When calculating transition strengths, certain parts of the $\hat{H}_P$ matrix are selected depending on whether we want to calculate σ^+ or σ^- transitions, and which D-line. Each strength factor (C_i) is then calculated by performing the dot product between one of the rows of $\hat{H}_{\mathrm{S}}$ with one of the post-selected rows of the excited state matrix. Many strength factors will be zero (with some numerical computing error) and as such a lower bound on the strength is placed in order to reject these transitions and save computing time. Also, the transition strengths corresponding to π transitions are not calculated since they are forbidden for the considered magnetic field orientation. It should be noted that in the case of a zero

magnetic field ElecSus adds a very small magnetic field (10^{-4} G) in order to discriminate between the energy levels. This is necessary in order to perform the post-selection. It should also be highlighted that even though we calculate the full P-term Hamiltonian, we cannot use this to calculate both D_1 and D_2 spectra at the same time, as might be expected. This is because the hyperfine coefficients used for the $n^2P_{1/2}$ term are different to those for the $n^2P_{3/2}$ term. The omission of lithium spectra from the current version of ElecSus is partly due to this reason. ElecSus treats D_1 and D_2 spectra separately, but lithium D_1 and D_2 lines are sufficiently close ($\sim 10\,\text{GHz}$) that they need to both be included when predicting a single spectrum.

3.3.3 Fitting experimental spectra and timing information

The user provides experimental data, in csv format, as two columns of values. The first column specifies the linear detuning (in GHz) while the second gives the spectrum data. If a different linecentre value (from that specified in B.2) has been used to make the linear detuning axis, the user can specify a global shift in the run card in order to take this into account.

Fitting theory to experiment involves defining a 'cost' function, which quantifies how far the theory curve deviates from the experimental. This is often defined as the square of the difference between theory and experiment summed at each point along the curve [118]. The cost function is then minimized by changing the parameters which define the theory curve. It is useful to think of this as finding the global minimum in a parameter space. There are three different fitting routines that can be used and should be selected based on the complexity of the fitting problem. A more complex fitting problem will tend to be one with many fit parameters.

In simple cases the option of fitting via the Marquardt-Levenberg (ML) method [118] should be chosen. This method is a 'hill-climbing' algorithm, which will quickly find the local minimum (or maximum, hence the name). Figure 3.3 shows four different experimental transmission spectra (the methods and apparatus used to take the data will be described in chapter 4). The data were taken at different temperatures, and these temperatures were then

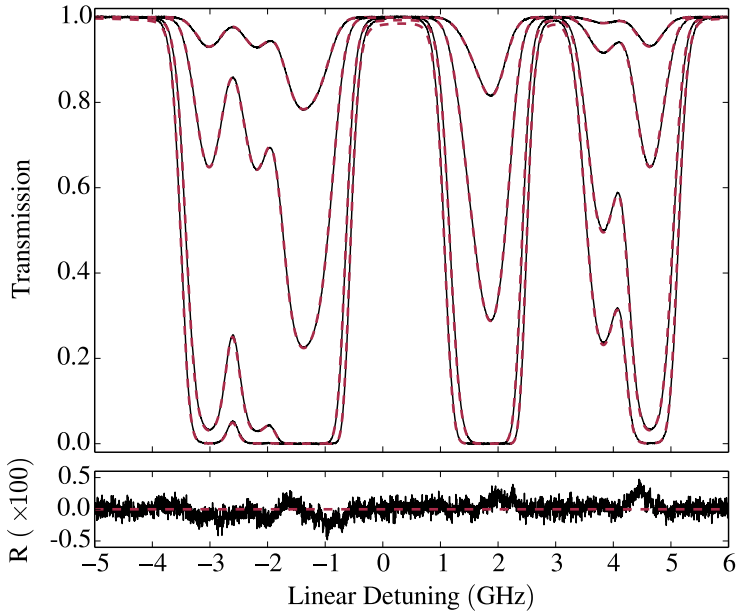

Figure 3.3: Plots of transmission versus detuning on the D_1 line (795 nm) for four different temperatures of a 75 mm long rubidium vapour cell with natural isotopic abundance. The (black) solid lines show the experimental data while the (red) dashed curves are theoretical results using ElecSus with temperature as the only fit parameter. Lower curves correspond to higher temperatures; the temperatures were found to be 18.6 °C, 36.1 °C, 59.8 °C and 69.3 °C. Underneath, the residuals (R) between experiment and theory are plotted for the 18.6 °C data set (rms deviation of 0.1%). The magnetic field was assumed to be zero.

found by fitting using the ML method. Typically, when fitting one parameter we find no further improvement by using the global fitting routines. One exception to this is the case of fitting high magnetic fields, where the ML technique can fail unless the initial guess is accurate. This is because there may be little or no overlap between the experimental and initial theoretical prediction, creating a plateau in parameter space which is known to be hard for hill-climbing algorithms to deal with [121].

For more complicated fits of more parameters the ML technique may fail to find the global minimum, and so a global fitting routine should be used. Figure 3.4 shows the result of fitting three experimental parameters using the ML method and the random-restart [121] (RR) method. The random-restart method is a meta-algorithm which simply performs an ML fit for a range of randomly generated initial states, then picks the best fit. In this way the

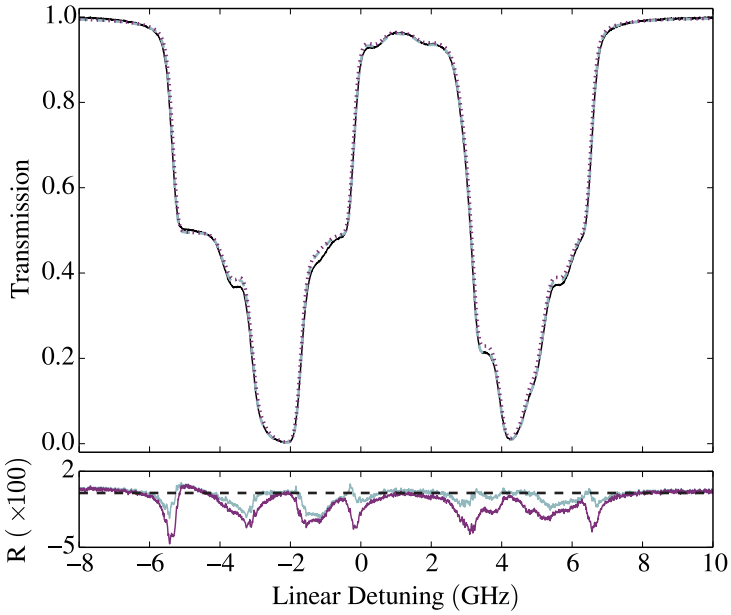

Figure 3.4: Transmission as a function of linear detuning on the D_1 line (795 nm) for a ^{87}Rb cell (99.0 % ^{87}Rb, 1.0 % ^{85}Rb) with a length of 1 mm. The solid (black) curve shows the experimental data while the dashed (blue) and dotted (purple) curves show fits to the theory using the RR and ML fitting routines. rms deviations from the experimental data of 0.5% and 1% were found for the RR and ML fits respectively. The fit parameters were the magnetic field, cell temperature, and increased Lorentzian broadening due to buffer gases.

RR technique has the possibility of escaping the nearest minimum. Another advantage of this method is that it is easily parallelized and can therefore be more time efficient; ElecSus will use all available cores of the computer's CPU in order to perform an RR fit.

Another global fitting routine supplied with ElecSus is based on simulated annealing (SA) [122]. It uses the Metropolis algorithm [123] with a $T_{n+1} = T_n/(1 + \delta T_n)$ cooling schedule [124] where δ is simply a small number. Figure 3.5 shows an experimental S_1 spectrum fitted to theory with four fit parameters, using both the ML and SA techniques. The ML method clearly does not perform as well as the SA method. ElecSus' RR routine was found to be unreliable when applied to these particular data, but on occasion did manage to find a good fit. Note the data in figure 3.5 are being used in this context simply as test data. However this spectrum has underlying interesting physical properties which will be studied in detail in chapter 5.

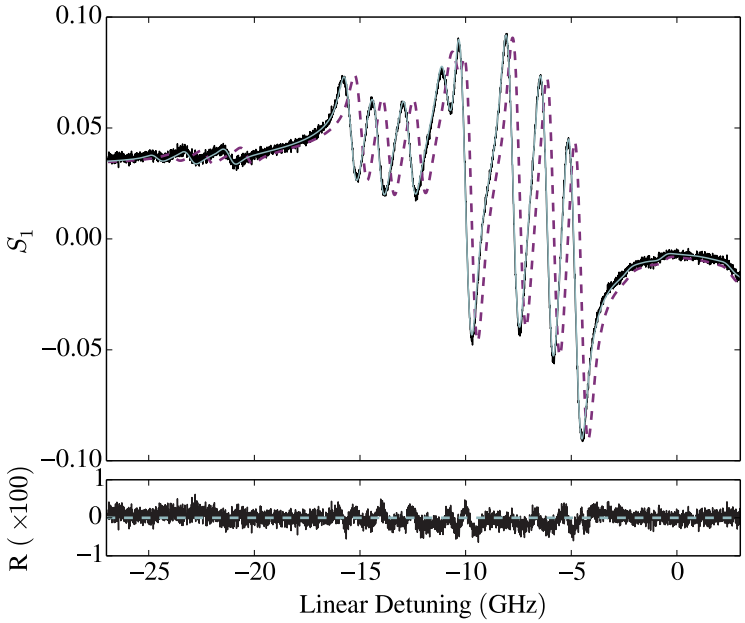

Figure 3.5: S_1 Stokes parameter as a function of linear detuning on the D_2 line (780 nm) for a ^{87}Rb cell (99.0 % ^{87}Rb, 1.0 % ^{85}Rb) with a length of 1 mm. The solid (black) line is the experimental data while the solid (blue) and dashed (purple) lines are the fits to theory using the SA and ML techniques respectively. The ML fit is clearly poor; shown underneath are the residuals for the SA fit. The rms deviations of the ML and SA fits were 2.2% and 0.16% respectively.

To compare the speed of the different fitting routines the data provided in figure 3.4 were fit to theory using all three fitting routines, with the same precision (10 MHz) and the same number of points (4774). A computer with an Intel® Core™ i3-3220 processor was used. The time taken was found to be 13 seconds, 80 seconds and 10 minutes for the ML, RR and SA techniques respectively. Note that the RR technique involves evaluating spectra in parallel (4 parallel processes in this case) whilst the other two are sequential.

Uncertainties in fit parameters

When fitting experiment to theory a 'χ^2' analysis [118] is often used to extract the statistical uncertainty in the fit parameters. This requires knowledge of the uncertainty of the data points which will vary between different experiments. The current version of ElecSus has no facility to accept these uncertainties as an input and so does not provide uncertainties in the fit pa-

rameters. However, since ElecSus outputs the theoretical curve as a csv file, the user can perform this analysis manually (see [118]).

Another method to extract the statistical uncertainty in the fit parameters is to take several data sets under nominally the same experimental conditions and fit them independently. This gives several values for each fit parameter. Then the mean and standard error of each parameter can be found from this set of values. By this method we have found that our experimental technique typically gives statistical uncertainties of $\sim 0.1^\circ$ C for temperature and ~ 1 G for magnetic field [45] (at large magnetic field values).

3.4 Installation and usage

The program can be downloaded from `http://www.jqc.org.uk/research/project/elecsus/12683` as a zip file named `ElecSus.zip`. Installation should be complete after simply extracting the `ElecSus.zip` file. No further action is required since it is assumed that the prerequisites (NumPy, SciPy and Matplotlib) are installed, and are found by the python interpreter. To use the program, the following steps should be taken.

1. Open a command prompt window and move to the directory extracted from the zip file (main directory).
2. Copy the file `runcard.py` to create your own file `myruncard.py`.
3. If fitting is required, place the csv file containing the data in the main directory.
4. Change the values and options in the file `myruncard.py` to the desired ones.
5. Execute the following command in the prompt window:

   ```
   python elecsus.py myruncard.py
   ```

   If the `myruncard.py` option is omitted the program will, by default, look in `runcard.py` for parameter values and options.

3.4.1 Run card parameters and options

In the run card the user must specify which alkali element, D-line and spectrum they want to compute. The choices of spectra for ElecSus to compute are the refractive indices, $n^{\pm}$, the group indices, $n_g^{\pm}$, Stokes parameters and the individual I_x and I_y spectra. The user can then specify parameters such as temperature, cell length, etc. and whether they would like to fit experimental data or simply produce a theoretical prediction. The variables in the run card are python variables, and as such the order in which they are specified does not matter.

We should note that there are two temperature variables, one which parameterizes the number density (see B.1) and one which parameterizes the Doppler broadening, where the second is constrained to the first by default. The option to treat these two temperatures separately is included for two reasons. The first reason is that non-uniform heating of vapour cells can cause the vapour temperature near the laser beam to be different to the temperature at or near the metal reservoir. As we will see in chapter 4, a small inhomogeneity in cell heating is desired to avoid metal condensing on the windows. The second reason is that the number density formulas used are only quoted to be accurate to about 5% [6], and so when fitting to a sufficiently accurate and precise experimental spectrum we would expect the two temperatures to disagree even if the whole cell is in thermal equilibrium. This disagreement would correspond to the systematic error in the vapour pressure formula.

It should also be noted that not all the options are relevant, and in these cases ElecSus will ignore those entries. For example when fitting to data the options that define the detuning axis are ignored since this is defined by the first column of the csv data file provided by the user. However, these variables should not be deleted from the run card.

3.4.2 Test runs

Provided with ElecSus are two sets of experimental data taken using the same experimental procedure described in chapter 5. Also provided are two

sample run cards, which can immediately be used by the user to ensure the program is working on their computer.

The first example can be run by executing the following command in a prompt window whilst in the main directory:

```
python elecsus.py runcard_D1sample.py
```

This will use the data provided in the data file `SampleDataRbD1.csv`, and then fit three parameters using the RR method. Since these data are the same as shown in figure 3.4, and the same parameters are being fitted, the result should be very similar to that found in figure 3.4. Fitting should not take longer than a few minutes.

Similarly, the user can run the second example with the `runcard_D2sample.py` file. This will use data from the `SampleDataRbD2.csv` file, which is the same as the data shown in figure 3.5. Running this example will fit the data using the SA technique and should give a correspondingly similar result to that seen in the figure. Note that this example can take up to 30 minutes to run.

3.5 An example application: Faraday filtering

Faraday filters are made by placing a Faraday rotator between two crossed polarizers [53]. Using an atomic medium as the Faraday rotator means typically only frequencies close to a resonance line are rotated and hence creating an ultranarrow filter. Here we predict Faraday filtering spectra on the D_2 line for all four alkali metals programmed in ElecSus.

To generate a Faraday filtering spectrum in ElecSus we first need to emulate the effect of the first polarizing beam splitter cube by setting p to 50% (see equation (3.21)) and θ_0 to 90°. This defines the light before the medium as linearly polarized in the y-direction. We then choose to plot the I_x spectrum which corresponds to light transmitted through a second polarizer crossed with the first. Note that choosing $\theta_0 = 0$ and plotting I_y gives the same result.

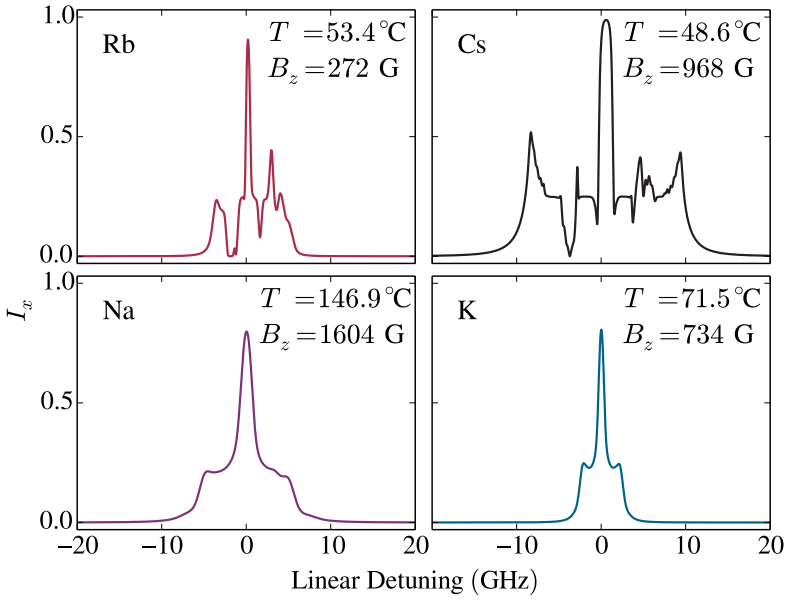

Figure 3.6: Faraday filtering. The intensity of light polarized in the x-direction (I_x) after propagating through a 75 mm long atomic medium. The incident intensity is normalized to one and the light is linearly polarized ($p = 50\%$) in the y-direction ($\theta_0 = 90°$). The vertical axis of each plot ranges from 0 to 1. Each horizontal axis shows the linear detuning from the D_2 global linecentre of each element (see B.2), ranging from -20 to 20 GHz. The temperatures parameterising number density and Doppler broadening were constrained to be the same, while isotopic ratios were set to their natural values.

The spectral profile of the filter can be controlled by changing cell length, magnetic field and temperature. The optimal spectral profile is dependent on the application; we have chosen to emulate filters in the line-centre operation [98], where the main filter transmission occurs at the weighted line centre. Figure 3.6 shows the results for a 75 mm long atomic medium with all four alkali-metal vapours. Figure 3.7 shows the potassium filter profile taken from figure 3.6 along with the corresponding rotation angle and transmission curves for the two hands of light. We can see that transmission through this line-centre type filter occurs because of two effects. One is that the magnetic field is large enough to separate the σ^+ and σ^- transitions enough for there to be little attenuation at line-centre. The second is that the magnetic field causes a significant Faraday rotation (near 90°) for frequencies near line-centre. Notice that at frequencies where the medium is opaque for one polarization but transparent for the other, approximately 1/4 of the

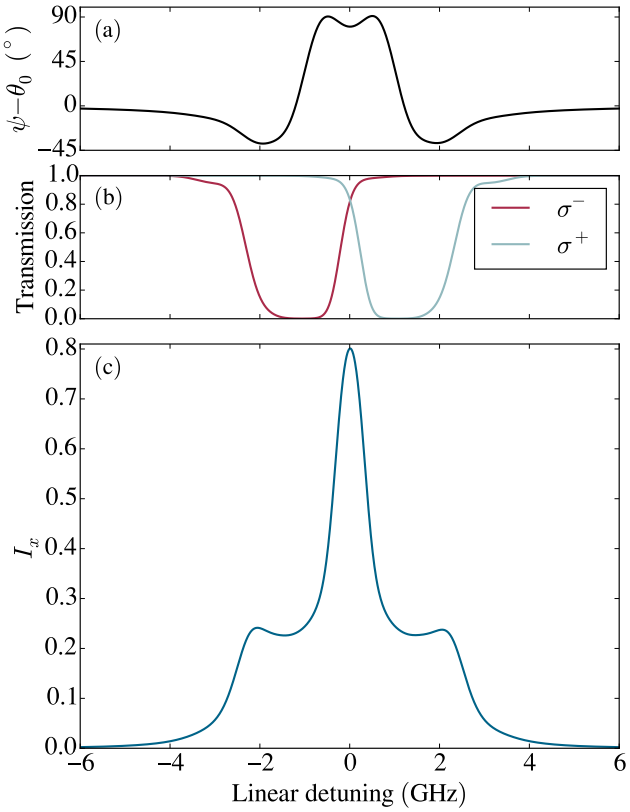

Figure 3.7: Faraday filtering on the potassium D_2 line. The vapour is modelled at natural abundance with a length of 75 mm, a temperature of 71.5°C and a magnetic field of 734 G. The light is modelled as initially linearly polarized ($p = 50\%$) in the y-direction ($\theta_0 = 90°$). Panel (a) plots $\psi - \theta_0$ (see equation (3.22e) which corresponds to the rotation angle of the plane of linearly polarized light (when circular dichroism is small). Panel (b) shows the transmission of the two circular polarizations which drive σ^+ or σ^- transitions. Panel (c) shows the intensity polarized in the x-direction (I_x) after propagating through the medium.

light gets through the filter. This is because at these frequencies the atomic medium scatters half of the light, while the linear polarizer only allows half the intensity of the remaining circular component through.

Faraday filtering is investigated in more detail in chapters 6, 7 and 8.

3.6 Discussion

We have presented a computer program to calculate the electric susceptibility of an alkali-metal vapour on the both the D-line transitions. The program can

be used to design optical devices such as Faraday filters, and laser-frequency stabilising references (see chapters 6 and 7, and section 5.4). The fitting routines provided in the program allow the user to measure experimental parameters (such as temperature or magnetic field). The program is fast which makes processes such as fitting or other kinds of optimization problem practical (the speed of the program is found to be particularly important for the applications shown in chapters 6 and 7).

We have modelled the D lines of Na, K, Rb and Cs; a future version will include Li. Also, extending the program beyond D-line transitions will prove useful. For example, including transitions from the nS ground state to the $(n+1)$P excited states will be useful for modelling Faraday filtering on these lines [125] as well as experiments utilizing these transitions for creating high phase-space density magneto-optical traps [126–128]. Also, extending the model to include transitions between excited states may allow modelling of excited state Faraday anomalous dispersion filters (ESFADOF) [28, 129, 130].

Working with atoms in confined geometries such as nanometric thin cells [19] or hollow-core fibres [131–136], introduces deviations of the atomic lineshape from the simple Voigt profile. This is due to effects such as atom-surface interactions [137–139] and Dicke narrowing. Extending the model to allow different atomic lineshapes has already been shown to accurately account for these effects [10, 139], and so we intend to extend ElecSus to include them.

Part II

Experimental applications

Chapter 4

Experimental techniques and apparatus

In the previous part of this thesis the underlying theory and computational methods were discussed. In this part of the thesis we look at physical applications realized by proof-of-principle experiments. To perform these experiments there are many common experimental techniques used. This chapter describes these experimental techniques and the apparatus.

Using the theory described in the earlier part of this thesis it is possible to design an atomic medium which has the desired circular dichroic and birefringent properties. On the experimental side, this means that the atomic medium needs to be prepared with a given length (ℓ), cell temperature (T) and axial magnetic field (B). This requires usage of various vapour cells for which heaters and permanent magnets are designed and mounted.

To test that the atomic medium is behaving as designed we also need to probe the medium optically. This is done by sending a laser beam of known frequency through the medium and detecting it on the other side. This can either be done with continuous-wave (CW) or pulsed light.

Here we describe the apparatus used to heat the vapour cells and to provide uniform magnetic fields. Also we describe the technique for calibrating the laser frequency and the apparatus employed to generate optical pulses from CW laser beams.

Figure 4.1: A vapour cell containing rubidium. The internal distance between the windows is 75 mm.

4.1 Vapour cells and heaters

In this section we will look at the three choices of vapour cell and also the heaters used to control their temperature. Different applications require different cell types. Each cell type requires a different heater, due to their vastly differing dimensions. However, a common feature of all the heaters is that they ensure the cell windows are not the coldest part of the cell. This is important because it prevents the alkali metal condensing on the windows and forming a reflective coating.

4.1.1 Vapour cells with a 75 mm long internal path

Figure 4.1 shows a typical 75 mm long vapour cell. These cells are commercially available and are made from borosilicate glass and contain the alkali metal[1] in a vacuum. These cells are typically long enough to provide a signal without heating, which makes them useful for laser frequency calibration (see section 4.3). However, as we will see in chapter 7, the cell needs to be heated, and an axial magnetic field applied, when using it as part of a Faraday filter. This is achieved by using a solenoid, which provides Ohmic heating as well as an axial magnetic field.

The solenoid is shown in figure 4.2. It is very similar to that described in [44] which is in turn based on a design described in [140]. The two coils of the solenoid are 43 mm in length and are mounted with a 12 mm separation between them. The nipple, in the centre of the cell, is somewhat exposed to

[1]Either rubidium or caesium were employed for the investigations presented in this thesis.

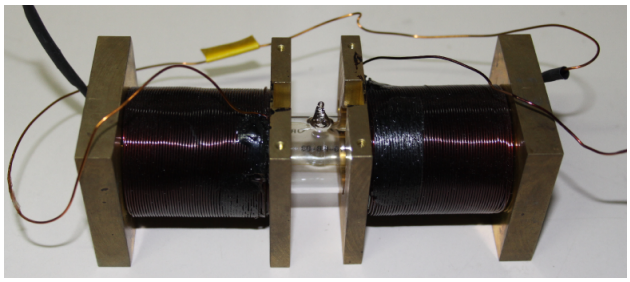

Figure 4.2: Photograph of a 75 mm long vapour cell inside the solenoid; the two sections of the solenoid are separated slightly to show the cell, but are usually mounted together. A solenoid, made from two sections, heats the vapour cell and provides an axial magnetic field.

the ambient air to ensure it is the coldest part.

The axial magnetic field produced by the solenoid can be estimated by modelling each turn of the coil as a ring and superimposing the field produced by each. The axial magnetic field for each circular ring is given by the well known formula [141],

$$B(z) = \frac{\mu_0 I r^2}{2\left((z - z_0) + r^2\right)^{\frac{3}{2}}}, \tag{4.1}$$

where z_0 is the position of the ring and r is its radius. Figure 4.3 shows the result of this model. The field variation is in agreement with numbers quoted in [44] and the profile qualitatively agrees with measurements made with the similar design shown in [140].

The standard deviation of the field across the length of the cell is $\sim 9\,\%$ of the average value. The model presented in part I of this thesis assumed a uniform field profile and so we may expect that experimental spectra will deviate from the theoretical spectra. The variation of the field along the cell length can be taken into account by modelling the vapour as sufficiently thin layers such that the field variation is negligible within a layer. Such modelling reveals that some experimental spectra can be very insensitive to field inhomogeneity (see chapter 7), meaning that treating the vapour as having a uniform field of the same strength as the average can be a good approximation.

Besides the variation in the axial magnetic field, it is possible to have a

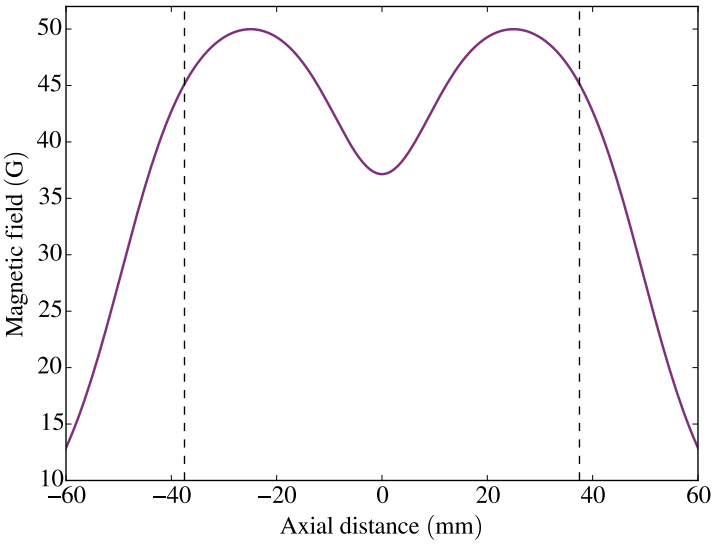

Figure 4.3: Axial magnetic field produced by the solenoid (shown in figure 4.2). The curve is the result of a model which approximates each turn of the coils as circular current loops and superimposing the result of equation (4.1) for each. The range within the vertical dashed lines show the extent of the atomic medium. With a current of 0.65 A, the average field across the length of the vapour is 46 G and the standard deviation is $\sim 9\,\%$ of the mean.

radial component of the magnetic field for parts of the laser beam profile which are off-axis. This radial component is not considered in the model presented in the last part of this thesis. Estimating the radial part of the magnetic field is complicated, but possible. Using the formulas provided in ref. [142], we estimate that the standard deviation of the radial component is $\sim 3\,\%$ of mean value of the axial component in the volume. Since this radial component is much smaller than the axial, we have ignored it.

4.1.2 2 mm long vapour cell and heater

For applications that require shorter path lengths (see section 1.1) a 2 mm long vapour cell can be used. Figure 4.4 shows the dimensions of the vapour cell. These vapour cells are also commercially available and are made from borosilicate glass. Heating of the vapour cell is usually required since the vapour is optically thin at room temperature on the D lines. This is again done via Ohmic heating. Ceramic resistors are used since they can withstand

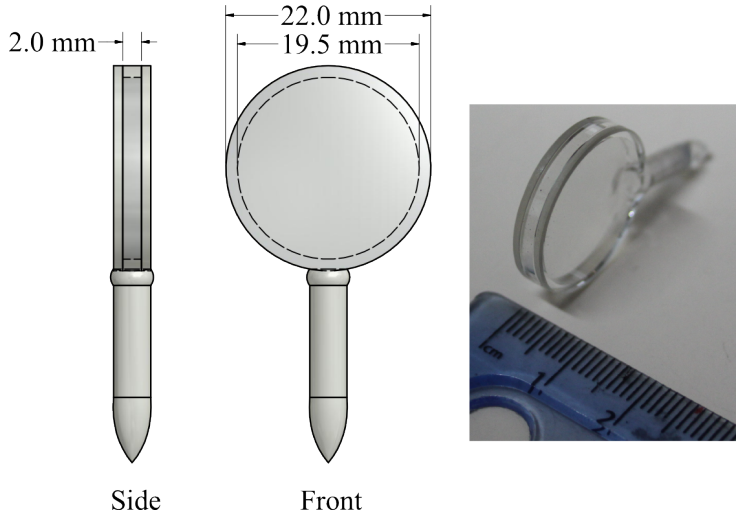

Figure 4.4: Schematic and photograph of the typical 2 mm long vapour cell. The metal reservoir is kept in the stem.

high temperatures (up to $\sim$ 350°C). Figure 4.5 shows a photograph of a mount constructed for a 2 mm long vapour cell and ceramic resistors. The mount is composed of two halves which are screwed together. The resistors are mounted above and below the cell. Slots have been cut out, below where the cell windows would sit, in order to thin the aluminium material and slow the heat flow between the upper and lower sections. In this way the top part can be kept at a different temperature to the bottom, which allows the cell windows to be hotter than the stem.

Three holes, each with a diameter of 2 mm, are drilled though the aluminium for laser beams to pass through the vapour cell. Two of the holes are drilled such that beams can pass through the 2 mm length vapour, one at the centre of the windows and the other at the edge. The third hole is drilled perpendicular to the first two such that a beam passing though would enter the medium from the curved face.

4.1.3 Mircro-fabricated cell and heater

For chapters 5 & 6 the experimental cells were micro-fabricated $1 \times 1 \times 1$ mm cube cells [21], provided by S. Knappe from NIST. Figure 4.6 shows the cell and heater used for the experiment in chapter 5. A single ceramic resistor is mounted along with the mirco-fabricated vapour cell in a copper holder.

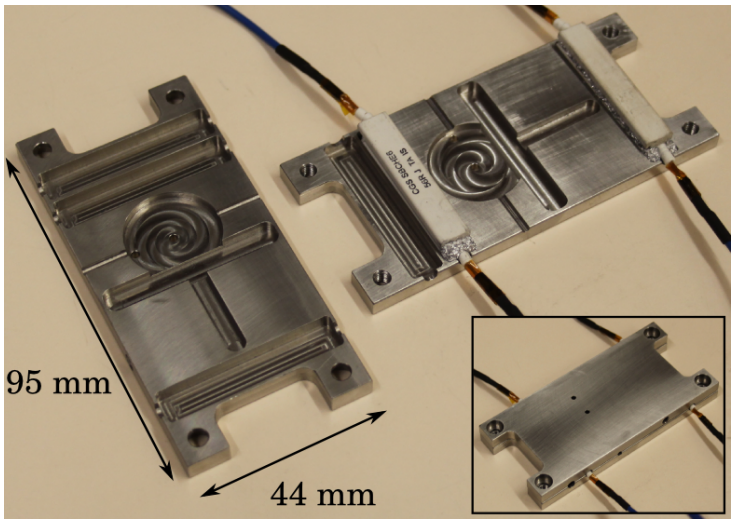

Figure 4.5: Photograph showing the aluminium mount for the cell and ceramic resistors made from two parts. There is space for two resistors above the cell and one below. Two of the typical ceramic resistors are also shown. The windows of the cell should be kept hotter than the stem to stop the alkali metal condensing on the windows. The inset shows the mount once the two parts are screwed together, giving a total thickness of 9.5 mm.

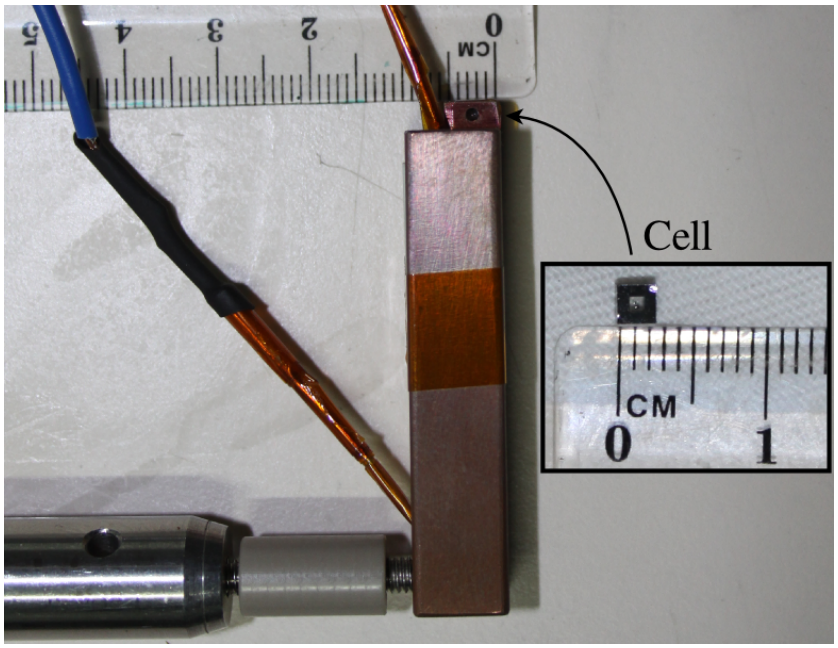

Figure 4.6: Photograph showing the copper mount for a ceramic resistor and the $1 \times 1 \times 1\,\mathrm{mm}$ cube vapour cell. The copper mount is held up with a post via a plastic (polyether ether ketone) connector which insulates the copper from the steel post.

A hole is drilled to allow a laser beam to pass through the vapour cell. The cell does not have separate compartments and so the metal reservoir may condense on the cell windows. Therefore, we focus the light with a lens to allow the probe beam to pass through the cell and miss the area where the metal reservoir has condensed. We use 30 cm focal length lenses, which in our experiment, give a beam waist of $\sim 80\,\mu$m.

The cell and heater used in chapter 5 is described in detail on page 91 of [120], and is similar to that described here.

4.2 Permanent magnets to apply an axial magnetic field

With the exception of the long 75 mm cells, permanent magnets are employed to create axial magnetic fields across the atomic vapour. We use axially magnetized ring magnets made from N52 grade NdFeB alloy. By using two ring magnets placed around the vapour cell, the magnetic field strength is changed by changing the distance between the magnets.

A formula to describe the field profile from the magnets aids in the magnet design such that the required field and uniformity can be realized. The magnetic field is a vector quantity, $\boldsymbol{B} \equiv (B_x, B_y, B_z)$, but if we remain on axis with a magnet with cylindrical symmetry, then $B_x = B_y = 0$. Assuming uniform magnetization, the following formula [143] calculates $B_z(z)$ along the axis of an axially magnetized cylinder,

$$B_z(z) = \frac{B_0}{2}\left(\frac{z - z_0 + d}{\sqrt{(z - z_0 + d)^2 + R^2}} - \frac{z - z_0 - d}{\sqrt{(z - z_0 - d)^2 + R^2}}\right), \qquad (4.2)$$

where $2d$ is the length of the cylinder, R is its radius, B_0 is the remanence field, and z_0 is the position of the cylinder's centre along z-axis (which points along the cylinder's axis). The field for a ring magnet is simply given by the principle of superposition. For a ring magnet with outer radius R_o and inner radius R_i the field is that from a cylinder of radius R_o minus the field from a cylinder with radius R_i. In a similar way, the field profile of any magnets with cylindrical symmetry can be calculated.

4.2.1 Achieving the hyperfine Paschen-Back regime for the micro-fabricated cell

Large fields can be achieved with a single compact magnet if the cell is placed within the bore of the magnet [29]. In chapter 5 we will use this technique to put an atomic vapour of ^{87}Rb into the hyperfine Paschen-back (HPB) regime (which we defined in section 2.4.1). We require a field approximately greater than 5 kG. The magnet used was identical to that described in [26], which gave a peak magnetic field of $\approx 5.5\,\mathrm{kG}$ and a field variation of $\approx 2\,\%$ across the length of the cell. A 2 % field inhomogeneity is sufficiently small for the purposes of our study, but for narrow spectroscopic signals [144] inhomogeneous magnetic fields may cause unwanted broadening. Here we show that by using a longer ring magnet it is possible to reduce the field variation.

Using the simple model described in the previous section a ring magnet was designed which reduced the field variation across the length of the cell. This was done by allowing the magnet dimensions and separation to vary whilst minimizing the standard deviation of the magnetic field across the 1 mm range where the cell would be mounted. The magnitude of the field profile was calculated using a previous measurement of the remanence field [26], $B_0 = (14.2 \pm 0.7)\,\mathrm{kG}$. Across the length of the 1 mm cell, the mean of B_z was designed to be 5.55 kG while the standard deviation was 0.36 G. The magnet was custom made and purchased from Magnet Expert Ltd. A Hall probe was used to measure B_z as a function of z. Figure 4.7 shows the measured field profile of the magnet as well as the designed profile. Since the magnet dimensions may not have been made identical to that specified, and/or the remanence may be different, these parameters were extracted using a Marquardt-Levenberg fit [118]. The fitted field profile and parameters are also shown in figure 4.7. Since the fitted field profile well describes the data, any inhomogeneity in the magnetization of the magnet is small. From the fitted profile, the mean magnetic field across the cell is $B_z = (5.48 \pm 0.03)\,\mathrm{kG}$ with a standard deviation of $(0.29 \pm 0.02)\,\mathrm{G}$ across the same region. This shows that the magnet will give a sufficiently large field and a field inhomogeneity of less than 0.01 %.

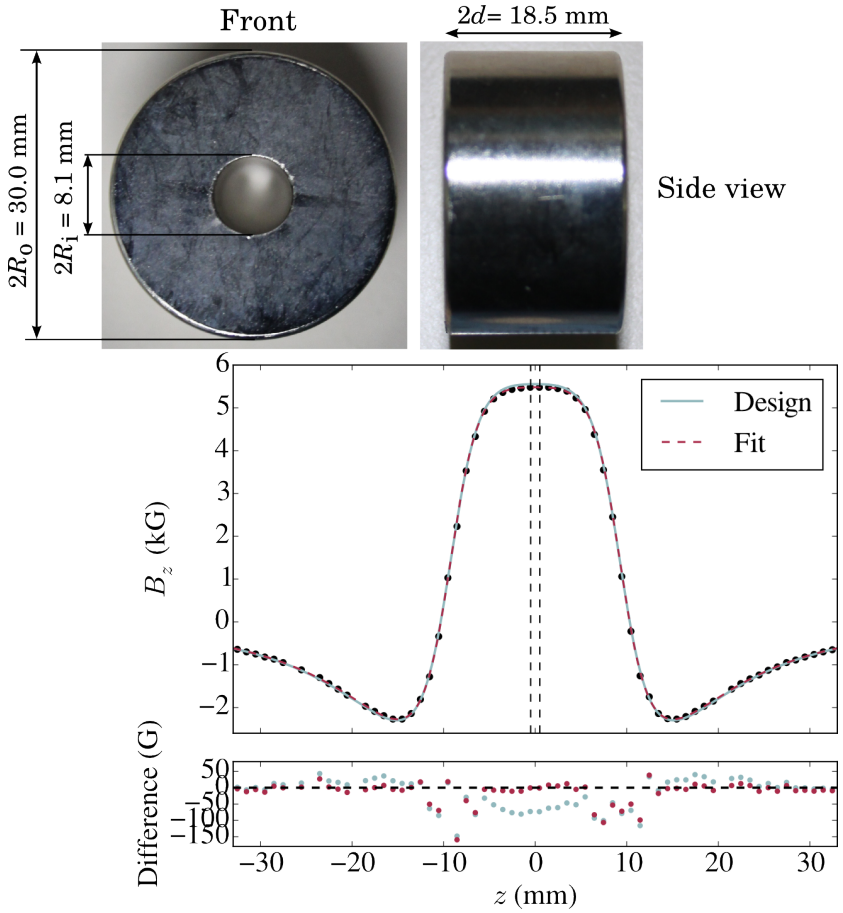

Figure 4.7: Axial magnetic field (B_z) as a function of axial distance z. The black dots show the Hall probe measurements while the blue solid line shows the designed profile. The red dashed line is the result of a Marquardt-Levenberg fit with fit parameters: $2R_\mathrm{i} = (7.81 \pm 0.04)$ mm, $2R_\mathrm{o} = (30.49 \pm 0.08)$ mm, $2d = (18.519 \pm 0.009)$ mm and $B_0 = (13.63 \pm 0.06)$ kG. The uncertainties in the fit parameters are quoted as the square root of the diagonal elements of the covariance matrix [118]. The vertical dashed lines show the extent of the cell. Underneath the main graph is a plot of both the difference between the experimental data and design values (blue), and the difference between the experimental and fit values (red). Any inhomogeneity in the magnetization only affects the residual between theory and experimental data at the 2% level.

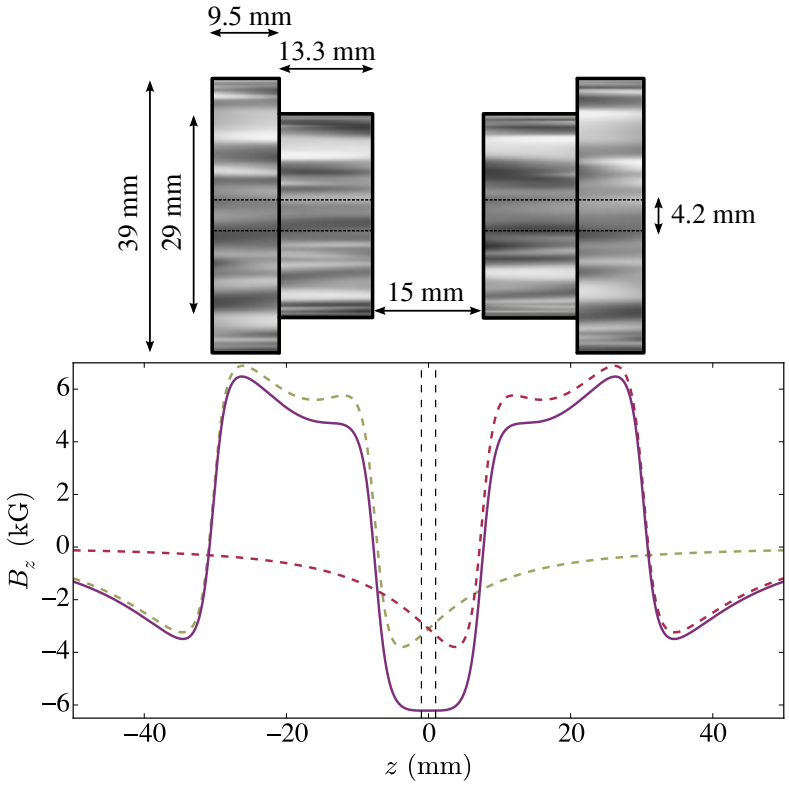

Figure 4.8: Schematic of the 'top-hat' magnet pair used to give a uniform magnetic field of 6.21 kG across the length of a 2 mm cell. A schematic of the magnet pair is shown. Each magnet has a 4.2 mm diameter axial bore for the laser beam to pass through. Underneath, the field profile produced by the magnet pair in the axial direction is plotted as a function of axial distance (solid purple line). The dashed olive and red lines show the field profile from each magnet individually. The vertical dashed black lines show the extent of the atomic vapour in the 2 mm cell. The average magnitude of the magnetic field across the cell is 6210 G with a standard deviation of less than 0.06 G. The schematic is to scale with the plot.

4.2.2 Achieving the hyperfine Paschen-Back regime for the 2 mm cell

Placing the 2 mm type of cell within the bore of a ring magnet is not possible without having a prohibitively large magnet. However, here we will show that a large and homogeneous magnetic field can be achieved using a pair of displaced ring magnets. This configuration also has the advantage of allowing optical access to the side of the vapour cell if desired.

When designing the magnet pair, we use the same procedure as described in

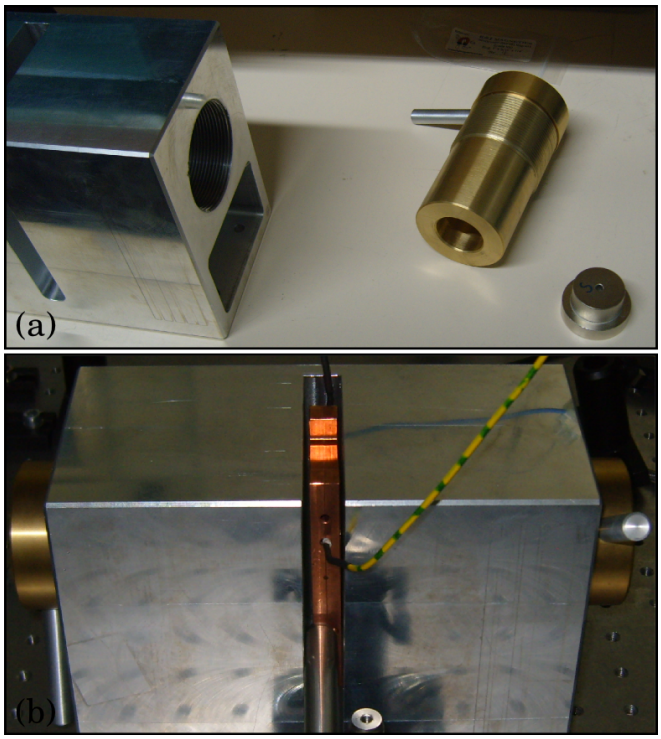

Figure 4.9: Panel (a) shows a photograph of one of the magnets (right), a brass magnet holder (centre) and the aluminium block (left). The magnets slot into the brass magnet holder such that the smaller diameter part can fit through the hole at the end but the rest cannot. The two brass magnet holders are threaded allowing them to screw into the aluminium block. Panel (b) shows the experimental arrangement. A copper version of the cell heater, shown in figure 4.5, is shown mounted between the magnets. Once the brass holders are fully screwed in the magnets are separated by the required 15 mm.

the previous section whilst constraining the dimensions of the two magnets to be the same and introducing their separation as a fit parameter. The magnetization of the two magnets is chosen to be in the same direction, such that the magnets attract each other. Figure 4.8 shows the result of this optimization. The field profile from a pair of magnets that have a 'top-hat' shape is shown along with the dimensions of the magnets. The top-hat shape can simply be modelled as adjacent ring magnets.

The field variation across the length of the cell can in theory be made arbitrarily small. The uniformity will be limited by the precision of the magnet manufacture and how accurately they can be positioned, along with the accuracy of the vapour cell positioning. Assuming a 0.1 mm error in all magnet dimensions and separation, along with a 0.5 mm shift in the vapour cell po-

sition, in the worst case the standard deviation of the field is 0.03% (2 G) of the average field across the length of the vapour cell.

The force between the magnets is considerable. By approximating each magnet as a cylinder with a 34 mm diameter, and using a Mathematica code provided from [145], we get an order of magnitude estimate of the force as $\sim 100\,\mathrm{N}$. Therefore a robust mount is required that allows one to mount the magnets safely without them snapping together. Figure 4.9 shows a magnet holder design made from an aluminium block. The design allows the magnets to be screwed in and out with a lever, making it easy to overcome the large attractive force and separate the magnets.

4.3 Laser calibration

Throughout this thesis, external cavity diode lasers (ECDL), with diffraction gratings providing the frequency selective element, are used (see chapter 8 for further discussion about ECDLs). The frequency of the lasers can be scanned but the frequency needs to be calibrated. The method of calibrating the laser scans was identical to that shown in [120]. Here we briefly describe this method.

Figure 4.10 shows an illustration of the experimental arrangement for calibrating the laser scan. The laser beam from the ECDL is incident on a beam splitter (BS). The reflected beam passes through an optical cavity and onto a photodetector (PD1). The light transmitted at the BS is incident on a polarizing beam splitter cube (PBS). The light transmitted after the PBS is sent to the experiment. The reflected beam is used to perform sub-Doppler hyperfine pumping spectroscopy [87, 146]. This beam is intense enough to optically pump atoms as it passes through a 75 mm long vapour cell. The beam is then attenuated by a neutral density filter (ND) before passing through a quarter-wave plate ($\lambda/4$). The beam is then reflected directly back onto itself, passing again through the $\lambda/4$, ND, and vapour cell. The double pass through the $\lambda/4$ causes a $\pi/2$ rotation in the plane of polarization, ensuring the light is now transmitted through the PBS and onto another photodetector (PD2). Each photodetector consists of a photo-

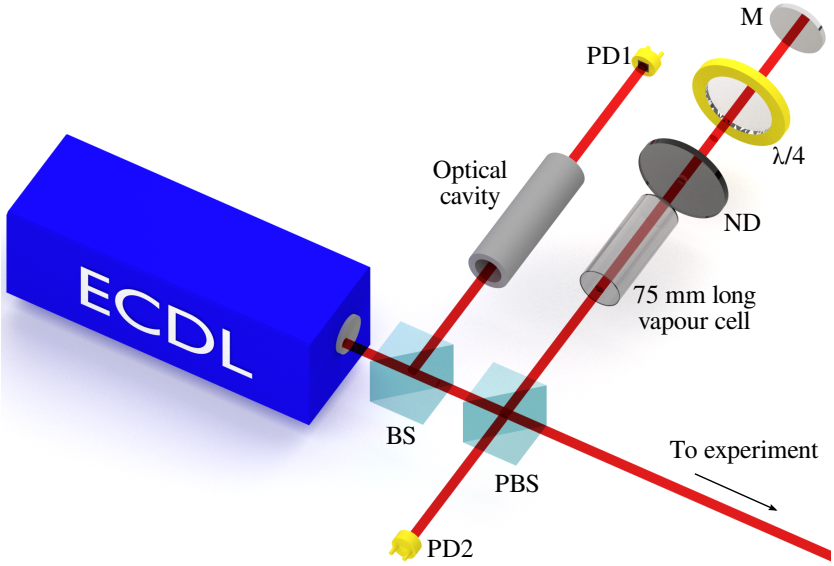

Figure 4.10: The experimental arrangement for laser calibration. ECDL – external cavity diode laser, BS – beam splitter, PBS – polarizing beam splitter, ND – neutral density filter, $\lambda/4$ – quarter-wave plate, M – mirror, PD1/PD2 – Photodetector number 1/2.

diode with a transimpedance amplifier. The voltage output PD1 and PD2 are recorded on an oscilloscope simultaneously. Figure 4.11 shows the two signals detected on the oscilloscope whilst the laser is scanned.

The peaks seen in the cavity transmission signal should occur at fixed frequency intervals. However, the peaks seen in figure 4.11 do not occur at fixed intervals in time, indicating that the laser frequency is non-linear with time. We can then use the cavity transmission peaks to 'linearize' the laser scan. This leaves us with a linear but arbitrary frequency axis. In order to turn this into an absolute frequency reference we use the sub-Doppler spectrum (also shown in figure 4.11). The sharp peaks in this spectrum correspond to well known atomic transition frequencies (and cross-over resonances [87]). As such the arbitrary frequency axis is shifted and scaled such that it fits to where the sharp peaks should lie. This leaves us with an absolute frequency axis. Figure 4.11 shows a scan over the rubidium D_1 line, but the technique is applicable to other elements and transitions from the ground manifold.

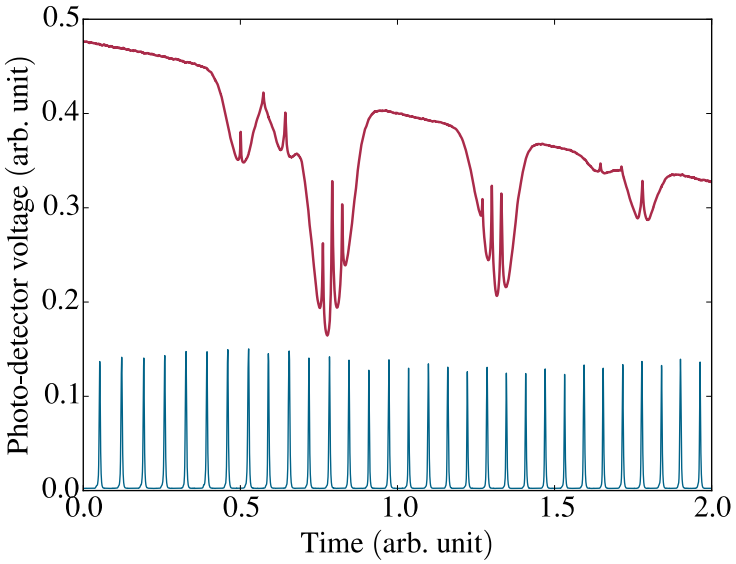

Figure 4.11: The red curve shows the sub-Doppler hyperfine-pumping spectrum recorded on PD1, whilst the blue curve shows the cavity transmission signal recorded on PD2. The vapour cell contained naturally abundant rubidium. The laser frequency is increasing with time, and is scanning over the rubidium D_1 line.

4.4 Generation of pulses with nano-second width

In chapter 9 we will be concerned with how optical pulses propagate through an atomic vapour. Interesting effects are seen for short pulses of the order of 1 ns. Here we describe the experimental technique used to generate the optical pulses.

To generate pulsed light we use the same continuous-wave ECDLs as before, but employ a technique that works like a fast shutter. Figure 4.12 shows an illustration of the apparatus used to generate pulses with a nano-second width. The CW laser beam passes through a Glan-Taylor polarising beam splitter (PBS), linearly polarising the beam. The beam then enters a Pockels cell [116], which rotates the plane of polarization when a large voltage is applied. The beam is then incident on another Glan-Taylor PBS which is crossed with respect to the first PBS. The extinction ratio, when the Pockels cell is inactive, is at the 10^{-3} level. The Pockels cell is attached to a voltage supply which can rapidly switch a large voltage. The Pockels cell acts as a

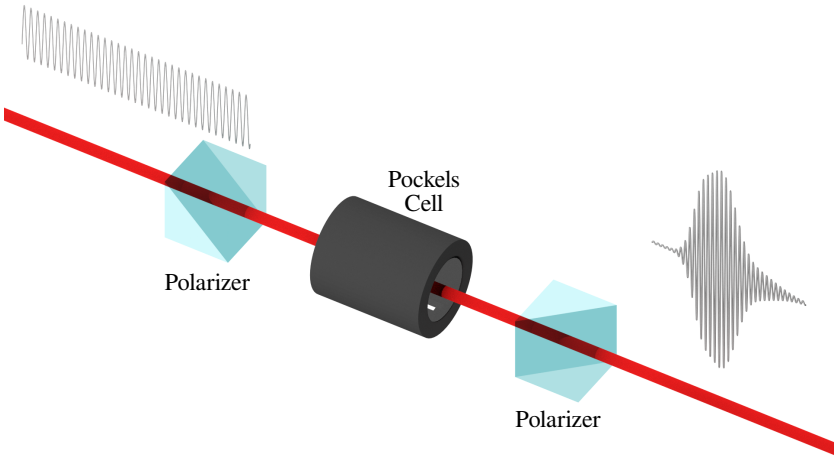

Figure 4.12: Illustration of the experimental arrangement for generating nano-second pulses. A CW beam is incident on crossed polarizers blocking the beam. A Pockels cell placed between the crossed polarizers is used to rapidly rotate the plane of polarization. This causes transmission through the second polarizer.

variable waveplate, and as such causes the plane of polarization of the beam to rotate and allow some transmission through the second PBS. Due to the short voltage pulse sent to the Pockels cell, a short optical pulse is created. Typically we measure pulse widths of the order of $\sim 1\,\mathrm{ns}$.

The detection of the optical pulses is done using single-photon counting modules (SPCMs) where the pulse profile is built up as a histogram over many repetitions. Further details of how this is done is given in appendix A.

4.5 Discussion

The apparatus used to heat the vapour cells has been described. Where possible, the windows of the cells are kept hotter than the other parts to avoid the alkali-metal vapour condensing on them. We should note that this inhomogeneous heating of the vapour cell will cause the gas temperature to be larger than the metal reservoir temperature. In general this will cause the temperature which parameterizes the Doppler width to be larger than the one which parameterizes the number density (as was briefly discussed in section 3.4.1). However, with the exception of chapter 9, treating the cell as having a single temperature value was sufficient.

Magnetic fields are applied to the vapour cells primarily from permanent magnets. The method used to design the magnets was discussed. We have shown that field inhomogeneity can be kept below 0.03% while achieving magnetic fields of up to 6.2 kG.

Also we have described the technique used to calibrate the laser frequency. This method has been used to calibrate all the experimental spectra in this thesis.

We have also described the apparatus used to generate optical pulses from CW laser beams. This is relevant for chapter 9 where the propagation of optical pulses through atomic vapour will be studied.

Chapter 5

The hyperfine Paschen-Back Faraday effect

5.1 Introduction and theory

In section 1.3 we explained that the Faraday effect is important for many applications involving atomic vapours. Some applications require very large fields [28, 29] of the order of 10 kG. As we saw in section 2.4.1, magnetic fields of this magnitude will cause alkali-metal atoms to enter the hyperfine Paschen-Back (HPB) regime. In this chapter we compare theory and experiment for the Faraday effect of an atomic vapour in the HPB regime. This extends previous work on absolute absorption [89] and dispersion [147] at high densities [10, 91] and high magnetic fields [26]. The Faraday effect in very strong magnetic fields has been studied before in the case of Rydberg transitions [148, 149]. However, to the best of our knowledge, it has not been studied for the main resonance lines (D lines).

5.1.1 The HPB Faraday effect

As we will see in the following sections, the HPB regime has some interesting consequences for the Faraday effect. By applying such a large magnetic field σ^+ and σ^- transitions are separated by a large frequency. This makes it possible to address σ^+ independently of σ^-, and vice versa.

Transition	$m_\mathcal{I}$	$\partial\nu_0/\partial B$ (MHz/G)		m_J	m'_J
		Hamiltonian	Approximation		
1	3/2	−1.46	-1.40	$-\frac{1}{2}$	$-\frac{3}{2}$
2	1/2	−1.52			
3	−1/2	−1.54			
4	−3/2	−1.40			
5	−3/2	−2.19	−2.33	$+\frac{1}{2}$	$-\frac{1}{2}$
6	−1/2	−2.21			
7	1/2	−2.27			
8	3/2	−2.33			

Table 5.1: Good quantum numbers characterising the σ^- (negatively detuned) HPB transitions 1 to 8, as labelled in figures 5.3 and 5.4. m_J and m'_J refer to the projection on the magnetic field axis of the total electronic angular momentum J in the ground and excited state respectively. Also given is the shift of the transition line-centre with a magnetic field around 0.55 T, as calculated with the Hamiltonian model described in section 2.3.4 and by the approximation of equation (5.1).

The HPB regime is defined when the Zeeman interaction is larger than the hyperfine splitting ($\mu_\mathrm{B}B > \frac{A_\mathrm{hf}}{\hbar^2}\boldsymbol{\mathcal{I}}\cdot\boldsymbol{J}$). However, we will define the hyperfine Paschen-Back Faraday effect as the situation where the Zeeman shift, Δ_Z, is larger than the Doppler width, Δ_D, as well as the hyperfine splitting. In this way we emphasise the importance of the splitting of σ^+ and σ^- transitions. This HPB Faraday effect is distinct from the resonant Faraday effect [46] where the laser detuning, Δ, is in the regime $|\Delta| < \Delta_\mathrm{D} \approx |\Delta_\mathrm{Z}|$, or the off-resonant Faraday effect [47] where $|\Delta| > \Delta_\mathrm{D} \approx |\Delta_\mathrm{Z}|$. In our experiment we use ^{87}Rb on the D_2 line ($5^2S_{1/2} \rightarrow 5^2P_{3/2}$) to investigate the effect.

5.1.2 Approximation for energy level shifts in the hyperfine Paschen-Back regime

When the hyperfine interaction is small compared to the magnetic field interaction we can approximate the shifts in the energy levels (ΔE) due to shifts in magnetic field (ΔB) using

$$\Delta E \approx (g_J m_J + g'_\mathcal{I} m_\mathcal{I})\mu_\mathrm{B}\Delta B, \tag{5.1}$$

which derives from equation (2.39). The values of the constants can be found in section B.2. Equation (5.1) can be useful to quickly estimate line-shifts with changes in magnetic field, since the line shift is given by the difference of the excited-level shift to the ground-level shift. Table 5.1 shows a comparison of this approximation to the more accurate Hamiltonian method at the magnetic field of our experiment.

5.2 Faraday rotation as a direct measure of refractive index

The Faraday effect has already been shown to be a good direct measure of absolute differential dispersion $(n^+ - n^-)$ [47, 54]. Measuring a spectrum (e.g. transmission) and fitting to the comprehensive model implemented by ElecSus allows the individual refractive indices, n^+ and n^- to be extracted indirectly. In general Faraday rotation cannot be used as a direct measure since both n^+ and n^- tend to change with detuning; other techniques need to be used [150, 151]. However, we show that measuring Faraday rotation in the HPB regime gives a good approximation to the individual refractive indices of the medium.

The output polarization is conveniently parameterized in terms of the Stokes parameter [111] S_1. Recalling equation (3.22b), for linearly polarized light incident on the medium, S_1 is calculated using the equation

$$S_1 = \cos(2\psi) \exp\left[-\frac{1}{2}\left(\alpha^- + \alpha^+\right)\ell\right], \tag{5.2}$$

where the rotation angle is simply given by $\psi = \frac{1}{2}(n_+ - n_-)k_0\ell + \theta_0$, where θ_0 is the initial angle with respect to the x-axis. Performing a Taylor-series expansion of the cosine (around $2\theta_0$) and exponential parts of equation (5.2), and writing explicitly in terms of the real and imaginary parts of n_c^+ and n_c^- gives

$$\begin{aligned}\cos(2\psi) = \cos(2\theta_0) - k_0\ell\left(n^+ - n^-\right)\sin(2\theta_0) \\ - \frac{1}{2}\left[k_0\ell\left(n^+ - n^-\right)\right]^2\cos(2\theta_0) + \dots,\end{aligned} \tag{5.3}$$

$$\exp\left[-k_0\ell\left(\beta^+-\beta^-\right)\right] = 1 + k_0\ell\left(\beta^+-\beta^-\right) + \frac{1}{2}\left[k_0\ell\left(\beta^+-\beta^-\right)\right]^2 + \dots . \tag{5.4}$$

Condition 1: We assume that the σ^+ and σ^- transitions are far from each other in frequency space, which is the case when in the HPB regime. If we consider the part of the spectrum far from σ^+ transitions then $n^+ \to 1$ and $\beta^+ \to 0$.

Condition 2: The optical depth of the medium is small implying that $k_0\ell\,|(n^- - 1)|$ and $k_0\ell\beta^-$ are small, such that we can neglect terms higher than first order in the Taylor series expansions. Note that by inspection of equation (5.3) this also requires θ_0 be set close to 45° (balanced polarimetry [46]), otherwise the spectrum will be insensitive to rotation. This leaves us with

$$S_1 \approx \left(n^- - 1\right) k_0\ell\left(1 + \beta^- k_0\ell\right). \tag{5.5}$$

Condition 3: If we further restrict β^- such that $\beta^- k_0\ell \ll 1$ then we derive our final result,

$$S_1 \approx \left(n^- - 1\right) k_0\ell. \tag{5.6}$$

If we instead consider the spectrum far from σ^- transitions, we change condition 2 such that $n^- \to 1$ and $\beta^- \to 0$. Repeating the derivation would give us the complimentary result,

$$S_1 \approx \left(1 - n^+\right) k_0\ell. \tag{5.7}$$

Note that the validity of equations (5.6) and (5.7) improves for larger magnetic fields, since condition 1 will be better satisfied. Figure 5.1 plots $S_1/k_0\ell$ along with $n^- - 1$ and $1 - n^+$ against detuning. S_1 was calculated without approximation using equation (5.2). In panel (a) we have modelled a simple system of three-level atoms with a single σ^+ and σ^- transition far detuned from each other. $S_1/k_0\ell$ gives an excellent approximation to the refractive indices when close to their respective transitions. Panel (b) shows the model of ^{87}Rb vapour on the D_2 line at 5.5 kG. We can see that $S_1/k_0\ell$ gives a reasonable approximation to $n^- - 1$ and $1 - n^+$, except in the region around zero global detuning, where the frequency of light is not sufficiently far from

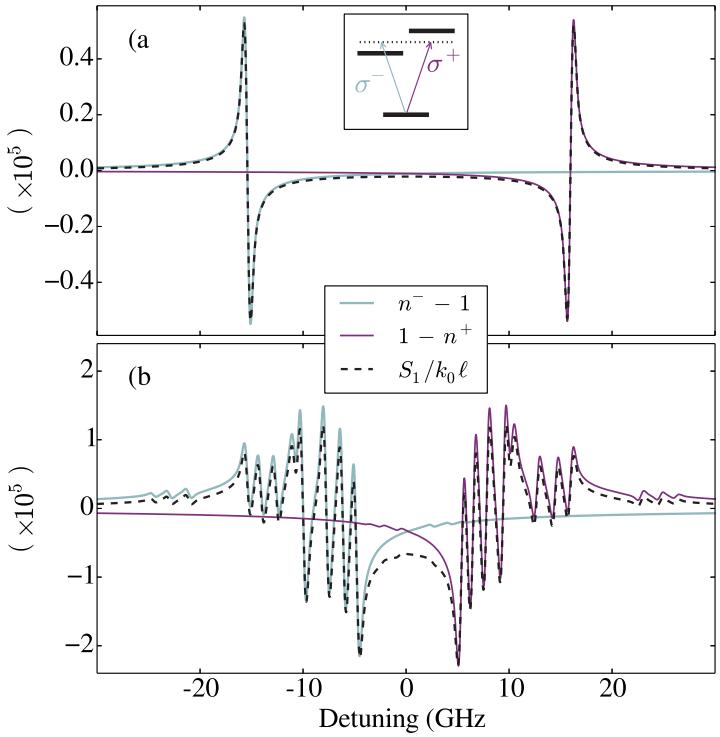

Figure 5.1: Faraday rotation signal $S_1/k_0\ell$ and circular refractive indices plotted against detuning. Panel (a) is modelled for a single σ^+ and σ^- transition each. Panel (b) is modelled for ^{87}Rb in a 1 mm long cell at a magnetic field of 0.55 T and a temperature of 70 °C (this fixes both the Doppler width and the number density [6]). The dashed black line corresponds to $S_1/k_0\ell$ while the light blue and purple lines correspond to $n^- - 1$ and $1 - n^+$ respectively.

resonance for either refractive index to be close to 1. We now investigate such Faraday rotation spectra experimentally.

5.3 Experimental apparatus and results

The experimental apparatus used was similar to that used in references [26, 29]. Figure 5.2 shows a schematic of the experimental set-up. An external cavity diode laser was scanned by ~ 30 GHz around the rubidium D_2 transition. Due to the limited mode-hop free tuning range of the laser, we restricted the scan to the negatively detuned part of the spectrum. The method described in section 4.3 was used to calibrate the laser scan. The beam was attenuated by a neutral-density filter ensuring the weak-probe

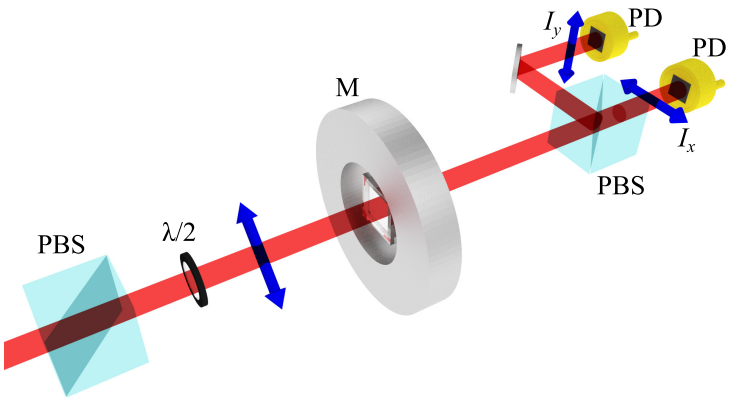

Figure 5.2: Schematic of the experimental set-up. PBS = polarizing beam splitter cube, $\lambda/2$ = half-wave plate, M = permanent magnet, PD = photodiode. Linearly polarized light set at an angle of 45 ° is incident on the thermal vapour cell. After the cell the horizontal and vertical polarizations of the beam are separated and measured on separate PD detectors.[*The experiment was set-up by Rebecca Andrews.*]

regime [87, 88] was achieved. The beam then travelled through a lens of focal length 30 cm, a polarising beam splitter cube (PBS) and a half-wave plate ($\lambda/2$) before being focussed onto the experimental cell. The $1 \times 1 \times 1$ mm^3 micro-fabricated vapour cell [21] was held within a permanent magnet. The cell was heated with similar apparatus shown in section 4.1.3 (see [120] for details of the heater used). After the cell the beam was collimated using another lens before being split into its horizontal (I_x) and vertical (I_y) polarizations with a PBS. These two beams were then measured on separate photodiodes (PD).

Figure 5.3 shows an example transmission and S_1 signal measured for a single laser scan. Excellent agreement between experiment and theory can be seen. Also shown in figure 5.3 are the atomic energy levels labelled by their eigenstates in the m_J basis ($m_\mathcal{I}$ labels are not included). The diagram of the energy levels shows that the weak transitions arise from small components of the eigenstates giving allowed $\Delta m_J = \pm 1$ transitions. It should be noted that the eight strong HPB transitions are insensitive to the nuclear magnetic moment while the weak transitions are sensitive. This can be seen from equation 5.1 and recalling the $\Delta m_\mathcal{I} = 0$ selection rule. The fact that the energy of the eigenstates are mostly governed by the largest contribution to the state, necessarily implies this difference in sensitivity.

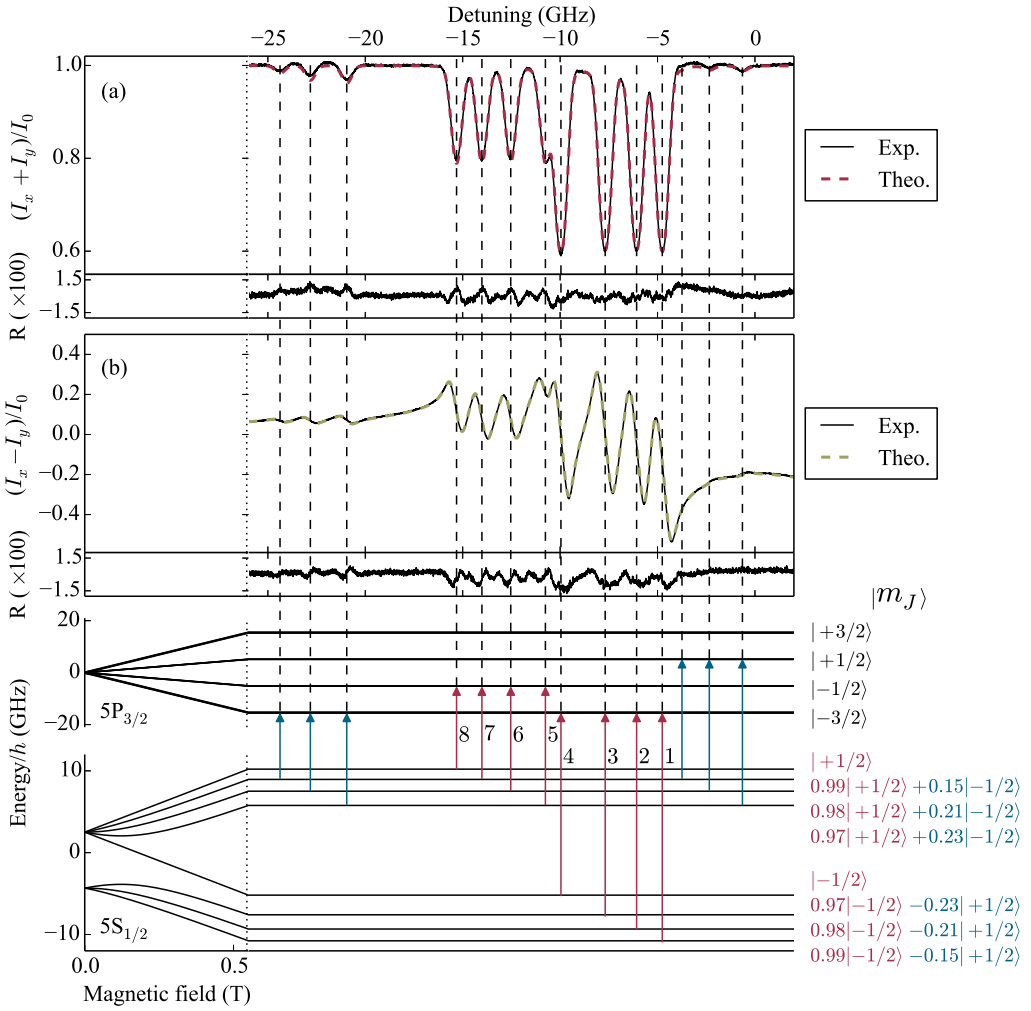

Figure 5.3: Experimental and theoretical transmission and Faraday rotation spectra for the 1 mm long Rb vapour cell (99 % ^{87}Rb, 1 % ^{85}Rb) with rubidium vapour number density of $\mathcal{N} = 3.10 \times 10^{12}\,\mathrm{cm}^{-3}$. Panel (a) shows the sum of the horizontal (I_x) and vertical (I_y) components of the probe beam divided by the initial intensity (I_0), equivalent to transmission. The solid black curve shows the experimental data, while the dashed red curve is the result of a fit to the model. Panel (b) shows $(I_x - I_y)/I_0$, the Stokes parameter S_1, using the same experimental data as that in panel (a). The dashed olive line is an independent fit to the model. The bottom sections of panels (a) and (b) show the residuals (R). We see excellent agreement between experiment and theory with rms deviations of 0.5 % and 0.7 % for the fits in panels (a) and (b) receptively. From fitting the transmission spectrum, the magnetic field was found to be (5.453 ± 0.002) kG, the cell temperature was $(89.95 \pm 0.05)\,^{\circ}$C, the buffer gas broadening was $\Gamma_{\mathrm{buf}}/2\pi = (47 \pm 2)$ MHz. From fitting the S_1 spectrum, the magnetic field was (5.454 ± 0.002) kG, the temperature was $(89.77 \pm 0.07)\,^{\circ}$C, the buffer gas broadening was (60.6 ± 0.3) MHz and the initial polarization angle was $(44.515 \pm 0.006)^{\circ}$. Below panel (b) the energy levels are shown with their eigenstates (labelled by m_J) calculated at 5.5 kG. The excited state manifold shows 16 levels in four groups of 4 but the spacings between levels in a group are too small to be resolved in the diagram. The transitions labelled 1 to 8 correspond to table 5.1. Note that the transitions are σ^- except for the three weakly allowed transitions on the right, which are σ^+.

Five data sets were taken in quick succession and each one was fitted to the model. We used a method similar to random-restart hill climbing [121] to avoid fitting to a local minimum, with the Marquardt-Levenberg method used to perform χ^2 minimisation and find the optimum parameters [118]. See the caption in figure 5.3 for the values of the fit parameters with their standard errors. These statistical uncertainties were found to be very small; systematic uncertainties are likely to dominate. See section 5.5 for further details on the systematic uncertainties.

The value of the magnetic field we extract corresponds to the average magnetic field across the beam path. By measuring the field profile produced by our magnet [26], we estimated a ~ 2 % magnetic field variation across the beam path. We achieve a small fractional statistical uncertainty in the average magnetic field of 4×10^{-4}.

Figure 5.3 shows that the individual transitions are separated by more than their Doppler width, making each transition separately addressable. This is due the fact that the hyperfine interaction is larger than the Doppler width. This individual separability is not a general feature of alkali-metals in the HPB regime, it will only be seen for vapour cells containing ^{87}Rb or Cs metal[1].

5.4 Laser-frequency stabilisation at large detuning

It has already been shown by Marchant *et al.* [44] that a Faraday rotation signal can be used as a laser-frequency reference at large values of detuning. In that system, with relatively low magnetic fields, zero crossings are achieved when the Faraday rotation is a multiple of 90°, but not at zero rotation. Since all the atoms in the path of the laser beam take part in rotating the plane of polarization, these zero crossings are sensitive to number density. Since number density is a near exponential function with temperature [6], the frequency where the zero crossings occur change rapidly with temperature

[1]There is an exception when using very thin cells where the Dicke narrowing reduces the line broadening [152, 153].

($\sim$ 0.2 GHz/°C [44]). Therefore, the cell temperature must be controlled carefully and may require active stabilisation.

In contrast, figure 5.3 shows an S_1 spectrum with zero crossings that occur for zero rotation angle. They occur due to the fact that $n^- - 1$ changes sign when the detuning is scanned over a σ^- resonance, while the refractive index for the light driving σ^+ remains constant at approximately 1. This also happens between resonances. These changes in speed across c cause a change in rotation direction and hence the zero crossings occur when the rotation is zero (when both circular polarizations of the light travel at c). This indicates that the position of these zero crossings should be temperature insensitive. Theoretically, the limiting factors to the temperature stability are the rotation caused by nearby resonances and the small deviation of n^+ from 1.

The effect was characterized theoretically by changing the cell temperature from 65 to 110 °C with all other parameters fixed ($B = 5.5$ kG, $\theta_0 = 45°$, $\Gamma_{\text{buf}} = 23.7$ MHz). This showed that the zero crossings typically move by less than 40 kHz/°C.

However, in real experimental conditions there will be more limitations. For example any offset in the signal, which for example could be caused by deviations of the input polarization from 45°, means that the zero crossing will no longer occur exactly at zero rotation. Other limitations arise from correlations between the other parameters and cell temperature. For example an increase in cell temperature is likely to cause heating of the surrounding neodymium magnet, which in turn will cause reversible demagnetisation [154]. To investigate these effects experimentally, transmission and S_1 spectra were taken at cell temperatures ranging from 60 to 125 °C. By fitting the spectra, a linear correlation between the cell temperature and the magnetic field was found with a gradient of (-2.21 ± 0.03) G/°C. From the manufacturer's specifications we expect $\sim$ 7 G change in magnetic field per degree change in magnet temperature. This shows that the magnet temperature increased by about 0.3 °C per one degree increase in cell temperature. It should be noted that there was no attempt to insulate the permanent magnet from the cell heater [16]. Despite this, the zero crossings were found to move by no more than $\sim$ 5 MHz per one degree change in

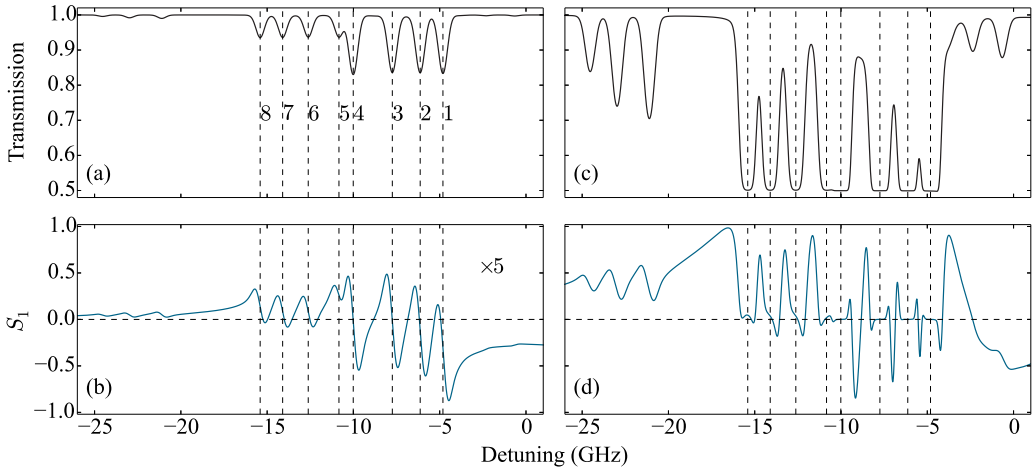

Figure 5.4: Theoretical transmission and S_1 spectra through a 1 mm long rubidium vapour (99 % ^{87}Rb, 1 % ^{85}Rb) with an applied magnetic field of 5.5 kG. Panels (a) and (b) correspond to a vapour temperature of 70 °C, while panels (c) and (d) correspond to 130 °C. The data in panel (b) have been multiplied by a factor of 5 for clarity. Transitions labelled 1 to 8 correspond to table 5.1. These transitions are the σ^- (negatively detuned) HPB transitions for which m_J and $m_\mathcal{I}$ are good quantum numbers. In the higher-temperature case, the increase in number density has caused the medium to be optically thick at some frequencies for one circular polarization. Also, at higher temperatures the S_1 spectrum (d) no longer approximates the refractive index since both absorption and rotation are large.

cell temperature. Note that this frequency shift can be estimated by using our determined (-2.21 ± 0.03) G/°C value along with the largest shift of -2.33 MHz/G shown in table 5.1 to estimate that the magnitude of the largest shift should be ~ 5 MHz/°C.

At high cell temperatures the medium starts to become optically thick for one circular polarization. When this happens the sharp zero crossings seen directly on resonance in the S_1 spectrum disappear. Figure 5.4 shows the effect on the atomic spectra when moving from the low-density regime to the high-density/optically-thick regime. However, the zero crossings between resonance can still be seen, with additional ones forming as a result of Faraday rotation of 90°. It is worth noting that the zero crossing between transitions 3 and 4 becomes a good reference at this high optical depth. Figure 5.4 clearly shows that when increasing the temperature of the vapour cell the amplitude of the signals arising from the three weak, far-detuned transitions (at -25 to -20 GHz) become significant. However, the Faraday rotation

induced from these resonances is always weaker than the off-resonant rotation of the stronger HPB transitions. This means that one cannot use the weak resonances to make zero crossings that occur at zero rotation. Therefore, these weak transitions cannot be used as highly temperature stable frequency references, in contrast to the HPB transitions.

5.5 Discussion of experimental systematic and statistical uncertainties

The systematic uncertainty in magnetic field was found by estimating shifts due to error in laser scan calibration ($\sim 10\,\mathrm{MHz}$) and buffer gasses ($\sim 8\,\mathrm{MHz}$ [26]), giving a value of $\sim 10^{-3}\,\mathrm{T}$. The systematic uncertainty in the temperature was found to be $0.7\,^{\circ}\mathrm{C}$, given by the uncertainty in the vapour pressure formula used [6]. For the initial polarization angle, the uncertainty in the difference between the collection and detection on the two photodiodes was estimated and equation (5.3) was used to turn this into an uncertainty in angle. This was found to be approximately $0.3\,^{\circ}$. The transmission spectrum was found to give a value of Γ_{buf} that was approximately double the $(23.7 \pm 1.2)\,\mathrm{MHz}$ previously found from fitting spectra with zero applied magnetic field [26]. We attribute this to non-uniformity of the magnetic field across the path length of the beam. Simulating the non-uniform magnetic field was done by averaging many theoretical transmission spectra over a range of field values. Fitting to this average spectrum gave a value of Γ_{buf} that was $\sim 20\,\mathrm{MHz}$ larger for a $2.5\,\%$ field variation. Also, the value of Γ_{buf} found from fitting to the S_1 spectrum was found to give a further $\sim 15\,\mathrm{MHz}$ larger value which was likely to be caused by imperfections in the polarizing optics after the cell. This is justified by simulating an imperfect PBS cube [155], which caused a decrease in contrast in the S_1 signal, which looks like an increase in Γ_{self} when fitting. These imperfections therefore affect the S_1 signal but not the transmission spectrum. In principle the effect of imperfect polarizing optics can be compensated for by multiplying by the inverse Mueller Matrix for the imperfections [155].

The statistical uncertainty in the experiment is largely attributed to detector

noise. If desired, further improvements could be made by modulating the input probe beam and then using a lock-in amplifier to recover the signal [103].

5.6 Discussion

We have investigated the Faraday effect in an atomic medium in the hyperfine Paschen-Back regime. In this regime a Faraday spectrum can be used to measure directly the refractive index of the vapour. ^{87}Rb was chosen to model the effect both experimentally and theoretically, finding excellent agreement between theory and experiment. We have also demonstrated sensitivity to fields of the order of 10 kG with a precision of the order of 1 G. In addition we note that the Faraday spectra have zero crossings that can be used to make laser-frequency error signals which are temperature insensitive, with a theoretical stability of the order of tens of kHz/°C.

Chapter 6

The effect of line-broadening on the performance of atomic Faraday filters

6.1 Introduction

Devices utilizing thermal atomic vapour cells are of increasing interest since they offer high precision with compact and relatively simple apparatus. Making these devices more compact, power efficient and lighter is currently a burgeoning area of research [16–18], since it allows them to become practical consumer products. However, when confining the atomic vapour in small geometries, additional effects may need to be taken into account. For example, atom-surface interactions become important for atoms in hollow-core fibres [134] or nano-metric thin cells [139]. Also, cells with a shorter path length require the medium to be heated more to increase the atomic number density. Not only will this increased heating cause more Doppler broadening but the increased number density will mean that self broadening [91, 156] must be taken into account. In this chapter we investigate the effects of these homogeneous and inhomogeneous broadening mechanisms on the performance of Faraday filters.

The Faraday-filter spectrum is sensitive to many experimental parameters and so a theoretical model is useful for designing filters. However, there are

only a few articles describing computer optimization [157]. In this chapter we use computer optimization to find the best working conditions for compact Faraday filters. We find homogeneous broadening is particularly important for Faraday filters in 'wing' operation [73, 99], where the filter transparencies occur just off-resonance from the atomic transitions, and less important for 'line-centre' operation [98, 157] (which we saw in section 3.5). The homogeneous broadening mechanism of self broadening is particularly important to include since it is unavoidable at high density. Previous theoretical treatments of Faraday filters [99, 158, 159] have not included the effect of self broadening; we find that self broadening is important for short cell lengths and must be included in the model in order to find the best working parameters.

6.2 Background

As we saw in section 3.5, the Faraday effect can be utilized to create a narrowband optical filter by placing an atomic medium between two crossed polarizers and applying an axial magnetic field. For a dilute atomic medium the Faraday effect is usually negligibly small except near resonances, and since atomic resonances are extremely narrow, this results in a narrowband filter. If the signal being detected is unpolarized then half of the light will not pass through the first polarizer. This limits the filter transmission to 50%. However using a polarizing beam splitter allows one to arrange two Faraday filters to allow each polarization component through with little loss [57].

For a given cell length the parameters that affect the Faraday filter transmission spectra are the applied field (B) and cell temperature (T). The effect of T is primarily to change the atomic number density [6] and secondly the Doppler width, while B causes the circular birefringence and dichroism. In general the filter spectrum is a complicated function of these two parameters which requires a computer program to calculate [72, 99, 157].

It should be noted that, in a similar way to using the Faraday effect, if the magnetic field is perpendicular to the light propagation direction, one can also make a 'Voigt filter' [160] which exploits the Voigt effect [161]. However,

in this chapter we will only consider Faraday filters. We have chosen to consider the D_2 ($n^2S_{1/2} \rightarrow n^2P_{3/2}$) lines of potassium and rubidium where $n = 4$ or 5 respectively.

6.3 Optimization

6.3.1 The simple approach

The optical signal in a vapour cell device comes from the interaction of the light with all the atoms in the beam path. This means that for compact vapour cells with shorter path lengths, the atomic number density must increase to compensate for the loss of signal. For example the linear Faraday-filter spectrum can be thought of as some function of the product $\sigma\mathcal{N}\ell$, where $\mathcal{N}$ is the number density, ℓ is the length of the medium and σ is the average microscopic atomic cross-section (describing the effect of extinction and dispersion due to a single atom). Assuming σ remains constant, when reducing ℓ we can achieve the same filter by increasing $\mathcal{N}$ by the same factor. Therefore, once good parameters of B and T are found for a particular cell length, we can find the new appropriate parameters by changing the temperature such that $\mathcal{N}\ell$ remains constant.

However, this argument will break down at some point since σ is not generally constant. By increasing the cell temperature we also change the amount of Doppler broadening. Also, at high densities interactions between atoms cause self broadening, which can be modelled as $\Gamma_{\text{self}} = \beta_{\text{self}}\mathcal{N}$, where β_{self} is the self-broadening parameter [91]. Both the Doppler and self broadening will affect σ. To find where these effects become important, we need to compare this simple approach of keeping $\mathcal{N}\ell$ constant, with a computer optimization technique which can find the best parameters at each cell length.

6.3.2 Computerized optimization procedure

Efficiently finding the optimal experimental conditions for a Faraday filter requires three tools. Firstly, a computer program is needed which can calculate the spectrum with the experimental conditions as parameters. Sec-

ondly, a definition of a figure of merit (or conversely a 'cost function' [121]) is then needed to numerically quantify which filter spectra are more desirable. Finally, this figure of merit is then maximized (or the cost function is minimized) by varying the parameters according to some algorithm.

We used a global minimization technique [118] which includes the random-restart hill climbing meta-algorithm [121] in conjunction with the downhill simplex method [162] to find the values of B and T which maximized our figures of merit. This routine was used in conjunction with the ElecSus program [72] which calculated the filter spectra. ElecSus was used because it includes the effect of self broadening, which is essential for this study, and also because it evaluates the filter spectrum quickly ($< 1\,\mathrm{s}$) which makes this kind of optimization practical, since the filter spectra need to be evaluated a few thousand times.

6.3.3 Figure-of-merit choices

The signal-to-noise ratio of a narrowband signal in broadband noise is greatly improved by using a bandpass filter. For the case of white noise, the noise power is directly proportional to the bandwidth of a top-hat filter. For a more general filter profile, the equivalent-noise bandwidth (ENBW) is a quantity which is inversely proportional to the signal to noise ratio, and is defined as

$$\mathrm{ENBW} = \frac{\int_0^\infty I_x(\nu)\mathrm{d}\nu}{I_x(\nu_s)}, \tag{6.1}$$

where I_x is the light intensity after the filter, ν is the optical frequency and ν_s is the signal frequency. If there is freedom in the exact position of the signal frequency we can set it to the frequency which gives the maximum transmission ($I_x(\nu_s) = I_{\max}$).

Although minimising the ENBW is desirable, this usually comes with a reduction in transmission [157]. Using the following figure of merit,

$$\mathrm{FOM} = \frac{I_{\max}^2/I_0}{\int_0^\infty I_x(\nu)\mathrm{d}\nu} = \left.\frac{I_{\max}/I_0}{\mathrm{ENBW}}\right|_{I_x(\nu_s)=I_{\max}}, \tag{6.2}$$

we can maintain a reasonably large transmission [157], while minimizing the

ENBW. When optimizing using this figure of merit we often find a wing-type filter spectrum [73] (see section 6.3.4). In order to compare with line-centre filters we also use the following figure of merit,

$$\mathrm{FOM}' = \left.\frac{I_x^2(\nu_s)/I_0}{\int_0^\infty I_x(\nu)\mathrm{d}\nu}\right|_{\nu_s=\omega_0/2\pi}, \tag{6.3}$$

where we set ν_s to the desired signal frequency, which in this case is the line-centre frequency.

To calculate these figure-of-merit values we simulate filter spectra with a range of 60 GHz around the atomic weighted line-centre with a 10 MHz grid spacing. The integration is performed by a simple rectangle method. For the temperatures and magnetic fields explored in this chapter, the limitation to the accuracy of the calculated figure-of-merit values comes from the grid spacing; a finer grid spacing of 1 MHz only improves the accuracy by 0.2% at best.

Note that truncating the ENBW integration to the $\Delta/2\pi = -30$ to $+30$ GHz frequency range is justified if the optical noise does not extend to other transitions from the ground manifold (such as to the other D-line), although it is possible to use a Faraday filter in conjunction with an interference filter if this is the case [59].

6.3.4 The importance of using a global fitting routine

Section 6.3.2 describes a computer optimization procedure which is time efficient and will precisely find the global minimum. However, it can be instructive to plot the figure of merit calculated over the entire parameter space. Also, this allows one to check the reliability of the computer optimization technique. Figure 6.1 shows the inverse of the FOM of equation (6.2), for a naturally abundant potassium vapour, plotted as a function of both B and T. There are two deep minima in the parameter space. The one that occurs at a higher magnetic field and lower temperature corresponds to a line-centre filter profile, while the one at a higher temperature and lower magnetic field corresponds to a wing-type filter profile. The global minimum is the wing-type filter minimum. Using a global minimization routine we ensure we do

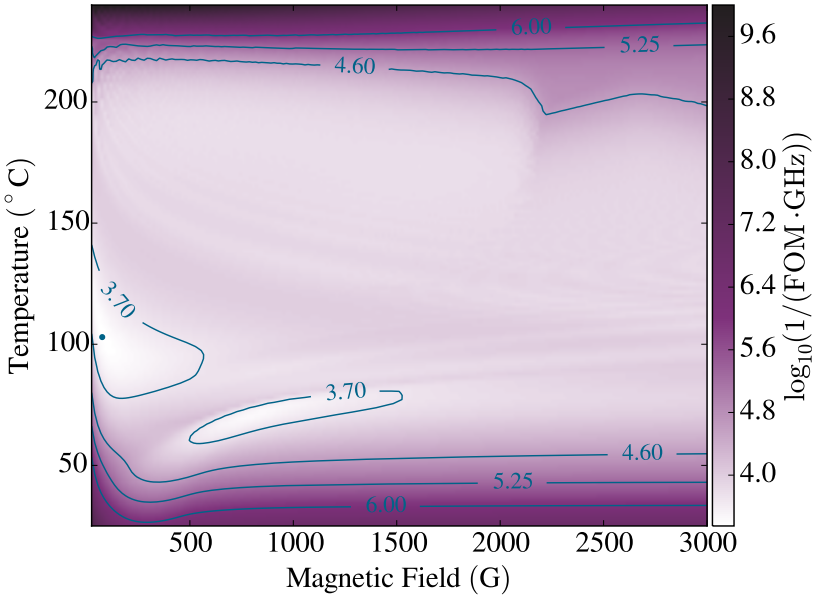

Figure 6.1: The inverse of the FOM of equation (6.2), for a naturally abundant potassium vapour with a length of 100 mm, as a function of magnetic field and temperature. The data were calculated with grid spacings of approximately 15 G and 1.7°C for the magnetic field and temperature ranges respectively. Contours are plotted as blue lines. There are two minima bounded by the contour lines given by $\log_{10}(1/\mathrm{FOM} \cdot \mathrm{GHz}) = 3.70$. The global minimum is plotted as a blue dot at $B = 76.3\,\mathrm{G}$ and $T = 107.3°\mathrm{C}$.

not fit the local minimum.

Figure 6.1 also shows the importance of choosing an appropriate figure of merit. Equation 6.2 should be used when we have the freedom in choosing the exact position of the signal frequency. However, if we need the signal frequency to occur at a specific value, equation 6.3 should be used instead. By choosing to use equation 6.3, with the line-centre as the signal frequency, one can ensure that a line-centre profile will be the global minimum. In the rest of this chapter we choose to use equation 6.2 to optimize wing-type filters for ^{87}Rb and we use equation 6.3 to calculate line-centre profiles for potassium. Potassium is a good element to investigate line-centre filter profiles since the Doppler broadening masks the hyperfine splitting. This is not the case for rubidium or caesium, resulting in more complicated spectra. Wing-type filter profiles on the other hand are straightforward to find for all four elements programmed in ElecSus. ^{87}Rb was chosen to allow comparison with experiment.

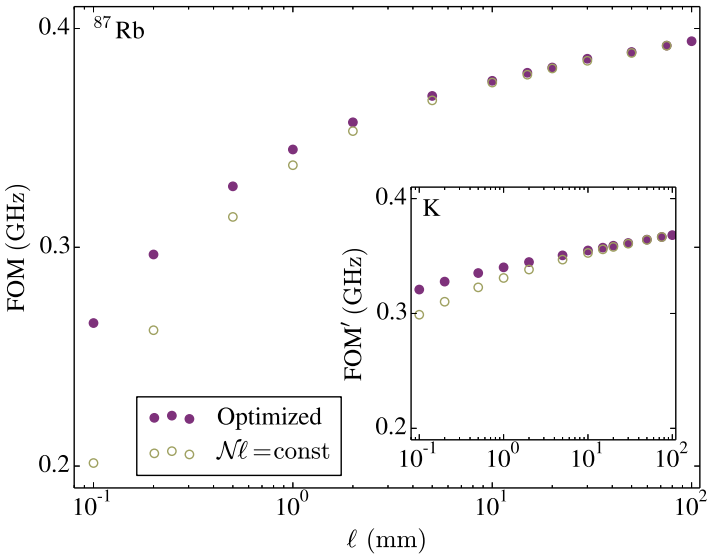

Figure 6.2: The figures of merit of filter spectra found by optimization or extrapolation. The hollow (olive) circles show the figure of merit found by taking the optimal magnetic field and temperature of the 100 mm length cell and changing the temperature such that $\mathcal{N}\ell$ = const. The solid (purple) dots show the figure of merit maximized by changing the magnetic field and temperature for each cell length. The main panel shows the results of a wing-type filter using an isotopically pure ^{87}Rb vapour, the inset shows a line-centre filter with a potassium vapour at natural abundance. Both are modelled for the D_2 line of the respective element.

6.3.5 Results for wing and line-centre filters

The figure of merit of equation (6.2) was maximized while simulating an isotopically pure ^{87}Rb vapour with $\ell = 100\,\text{mm}$, finding the optimal values of B and T to be 67.3 G and 60.9 °C respectively. We then used the simple approach (section 6.3.1) to find the new values of the vapour cell temperature for a range of shorter cell lengths, and then evaluated the figure-of-merit values. In addition the figure-of-merit values were re-optimized (section 6.3.2) for each cell length to see if further improvement could be made. Figure 6.2 shows the comparison of the two methods. We can see that the figure of merit changes with cell length, as is expected, since line broadening means that the filter spectra cannot be made identical for different cell lengths. We can also see that moving to shorter cells has a deleterious effect, but can be somewhat mitigated by re-optimization at each cell length.

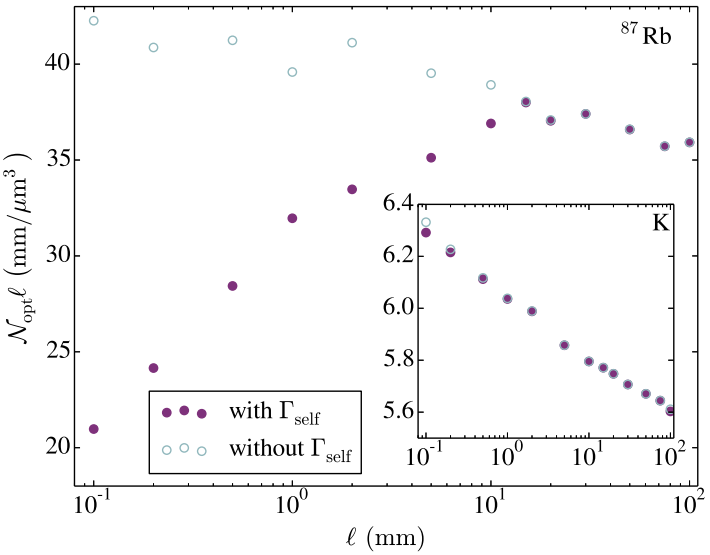

Figure 6.3: Atomic number density after computer optimization ($\mathcal{N}_{\rm opt}$) multiplied by cell length (ℓ), as a function of ℓ. The optimization involves changing the magnetic field and temperature of the cell in order to maximize the figure of merit at each cell length. The purple dots show the results when self broadening is included in the model for the filter spectrum, while the light blue circles show the result without self broadening. The main panel shows results for an isotopically pure ^{87}Rb vapour while the inset gives the results for potassium at natural abundance.

The inset of figure 6.2 shows the result of a similar analysis for a potassium vapour at natural abundance [163], this time using the figure of merit of equation (6.3) to produce a line-centre profile filter. The main difference in the results is that the figure of merit is less affected by decreasing cell length than the wing-type filter.

The reason for the difference between wing-type and line-centre filters can be elucidated by plotting the $\mathcal{N}\ell$ product as a function of ℓ after computerized optimization at each cell length, as shown in figure 6.3. By repeating the optimization with the effect of self broadening 'turned off', we can see that the ^{87}Rb wing-type filter is affected far more by self broadening than the K line-centre filter. One can understand this difference in the behaviour of the two types of filters by inspection of the spectra (see figure 6.4). Increases in Lorentzian broadening cause a decrease in transmission through the vapour cell at the filter frequency. This happens far more for the wing-type than line-centre filters. Changes in transmission on the wing of an

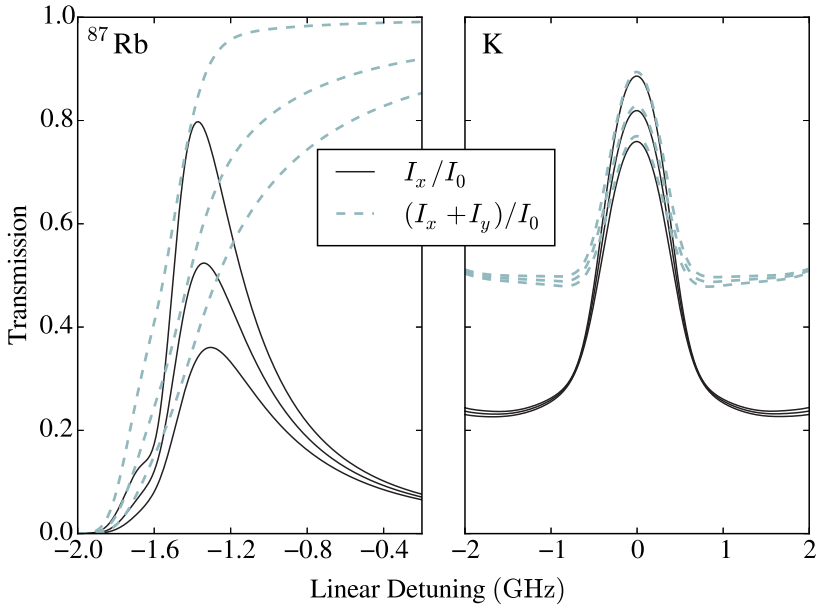

Figure 6.4: Filter transmission (I_x/I_0, solid black curve) and cell transmission ($(I_x + I_y)/I_0$, dashed blue curve) as a function of linear detuning ($\Delta/2\pi$), zoomed around the region of peak transmission. The left panel models a ^{87}Rb vapour on the D_2 line, while the right panel models the K D_2 line; both of length 1 mm. The cell parameters were set to $B = 85.8\,\mathrm{G}$ and $T = 127.8\,^\circ\mathrm{C}$ ($\mathcal{N} = 3.2 \times 10^{13}\,\mathrm{cm}^{-3}$) for ^{87}Rb, and $B = 864\,\mathrm{G}$ and $T = 136.1\,^\circ\mathrm{C}$ ($\mathcal{N} = 6.0 \times 10^{12}\,\mathrm{cm}^{-3}$) for K. The uppermost lines were calculated with a Lorentzian width given by natural broadening only ($\sim 6\,\mathrm{MHz}$) while the middle and lower lines have a further 50 and 100 MHz of Lorentzian width. The global line-centres occur at 384.23042812 THz [144, 164] for the Rb D_2 line and 391.01617854 THz [165] for the K D_2 line.

absorption resonance due to Lorentzian broadening is due to the fact that Gaussian broadening decreases much faster than Lorentzian broadening with detuning from resonance [166]. A higher optical depth transition feature will show this effect more strongly. This is one of the differences between wing and line-centre type filters. Wing-type filters rely on the sharp decrease in transmission caused by the atomic resonances to create narrow filter transparencies. This means that the circular dichroism cannot be too large since both polarizations need be scattered in the cell to sharply reduce the filter transmission to zero. However, a small amount of dichroism means that there is a small relative birefringence, which means that a high number density is required to create the large absolute birefringence necessary for the rotation of $\pi/2$. Conversely, the line-centre filter works by having a large circular

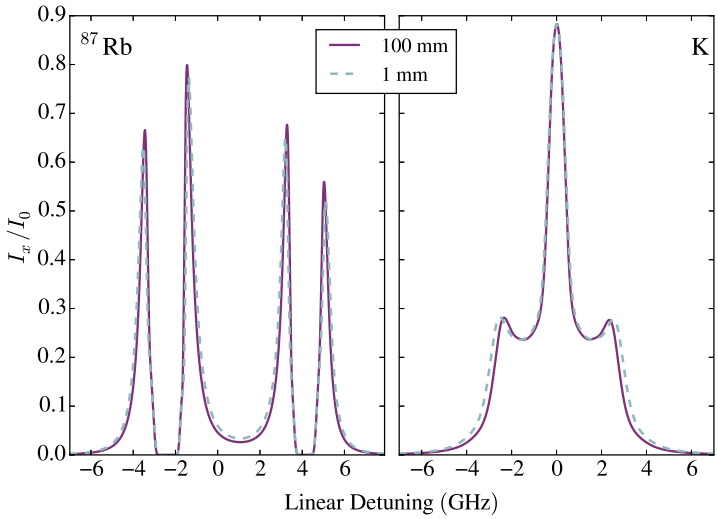

Figure 6.5: Computer optimized Faraday filter spectra as a function of linear detuning. The optimal parameters were found to be $B = 67.3\,\mathrm{G}$ and $T = 60.9\,^{\circ}\mathrm{C}$ for the 100 mm long ^{87}Rb vapour, $B = 85.8\,\mathrm{G}$ and $T = 127.8\,^{\circ}\mathrm{C}$ for the 1 mm long ^{87}Rb vapour, $B = 801\,\mathrm{G}$ and $T = 70.2\,^{\circ}\mathrm{C}$ for the 100 mm long K vapour, and $B = 864\,\mathrm{G}$ and $T = 136.1\,^{\circ}\mathrm{C}$ for the 1 mm long K vapour. The ENBW is 2.0 and 2.2 GHz for the ^{87}Rb vapour at 100 and 1 mm length receptively, whereas for the K vapour the ENBW is 2.4 and 2.6 GHz at 100 and 1 mm length receptively.

dichroism, such that the transitions which absorb each polarisation of light are almost completely separated. We can see this in figure 6.4 where the cell transmission is optically thick for just one circular polarization on either side of the transparency (causing $\approx 50\%$ transmission of linearly polarized light through the cell and $\approx 25\%$ transmission though the filter). This large dichroism comes with a large relative birefringence, meaning that the number density can be lower for a line-centre filter.

Line broadening clearly has a deleterious effect, however, good filter spectra for shorter vapour cells can be found as long as we change both the B and T to re-optimize the filter. This is shown in figure 6.5 where it is evident that the optimal filters achieved for a 1 mm cell length closely match that at 100 mm length.

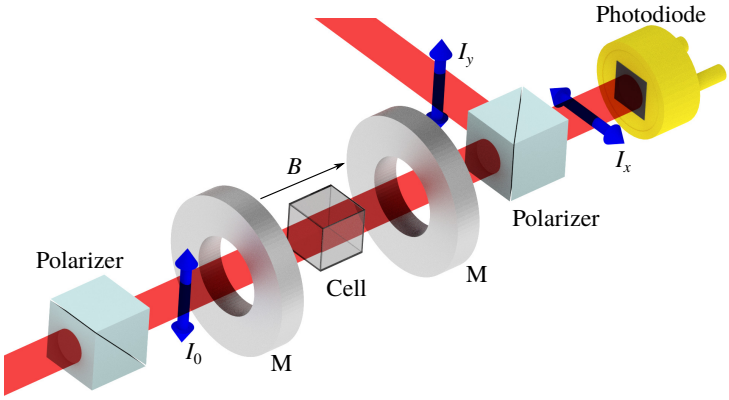

Figure 6.6: Illustration of the experimental arrangement. A micro-fabricated $1 \times 1 \times 1\,\mathrm{mm}^3$ ^{87}Rb vapour cell is placed between two axially magnetized ring magnets. This arrangement is then placed between two crossed polarizers, forming the filter. The filter is tested by passing a laser beam through and onto a photodiode. The filter transmission is defined as the intensity of light transmitted through the second polarizer (I_x) divided by the initial intensity before the cell (I_0). Light out of the passband frequency is either scattered in the cell or rejected at the second polarizer (I_y).

6.4 Experiment

To compare theory with experiment for a compact cell, we used the micro-fabricated $1\times1\times1\,\mathrm{mm}^3$ isotopically enriched ^{87}Rb cell shown in section 4.1.3. The isotopic abundance of ^{85}Rb was found by transmission spectroscopy to be $(1.00\pm0.02)\%$, in a similar way to that shown in [26]. This isotopic impurity affects the filter spectra, therefore the filter parameters were optimized taking this into account. We found the optimal parameters to be $B = 72.0\,\mathrm{G}$ and $T = 137.5\,^{\circ}\mathrm{C}$, which gave a transmission peak at a detuning of 3.1 GHz.

The experimental Faraday filter arrangement is illustrated in figure 6.6. The cell was heated close to the optimal temperature, while an axial magnetic field was applied using a pair of permanent ring magnets. The field inhomogeneity across the cell was less than 1%. Two crossed Glan-Taylor polarizers were placed around the cell to form the filter. A weak-probe laser beam was focussed using a lens (not shown in figure 6.6) with a 30 cm focal length, and was sent through the filter such that the focus was approximately at the location of the cell. After the filter, the beam was focussed using a 5 cm focal length lens onto an amplified photodiode. The laser frequency was

Spectrum	I_{max}/I_0	ENBW (GHz)	FOM (GHz^{-1})
Fit to Experiment	0.55	3.0	0.18
No buffer gas	0.77	2.6	0.29
No self broadening or buffer gas	0.83	2.6	0.31

Table 6.1: Maximum transmission (I_{max}/I_0), equivalent-noise bandwidth (ENBW) and their ratio (FOM) for a 1 mm long isotopically enriched vapour cell. The magnetic field and temperature were 73 G and 138.5°C respectively. The first row represents the fit to the experiment shown in figure 6.7, while subsequent rows give the values after certain physical effects were removed (theoretically).

scanned across the Rb D_2 transition, and was calibrated using the technique described in section 4.3.

Panel (a) of Figure 6.7 shows the experimental filter spectrum plotted with a fit to theory using ElecSus [72]. The fit parameters were found to be $B = 73\,\mathrm{G}$ and $T = 138.5\,^{\circ}\mathrm{C}$. The first thing to note is that, due to the 1% ^{85}Rb impurity, the peak transmission occurs at $\Delta/2\pi = 3.1\,\mathrm{GHz}$ rather than near $-1.3\,\mathrm{GHz}$ which would be the case if the cell were isotopically pure (see Figure 6.5). Also, a further 42 MHz of Lorentzian broadening was added in addition to Γ_0 and Γ_{self}, due to the presence of a small quantity of background buffer gas in the vapour cell. This value was previously measured by transmission spectroscopy to be $\Gamma_{buf}/2\pi = (42 \pm 1)\,\mathrm{MHz}$. Panel (b) of figure 6.7 shows the filter spectrum zoomed in to the main peak. In addition to the experimental data and theoretical fit, the filter spectrum for the optimization that did not include the buffer gas broadening is shown. We can see that the additional broadening drastically affects the filter transmission. Also by removing the effect of self broadening from the theory, we again see a larger transmission. Table 6.1 quantitatively compares the transmission, ENBW and FOM values for the curves shown in figure 6.7. The inset of panel (a) shows the filter transmission at a detuning of 3.1 GHz and the ENBW as a function of Γ_{buf}. The transmission decreases while the ENBW increases, showing that the performance (as measured by the the ratio transmission to ENBW) of this kind of Faraday filter deteriorates quickly with increasing buffer gas pressures.

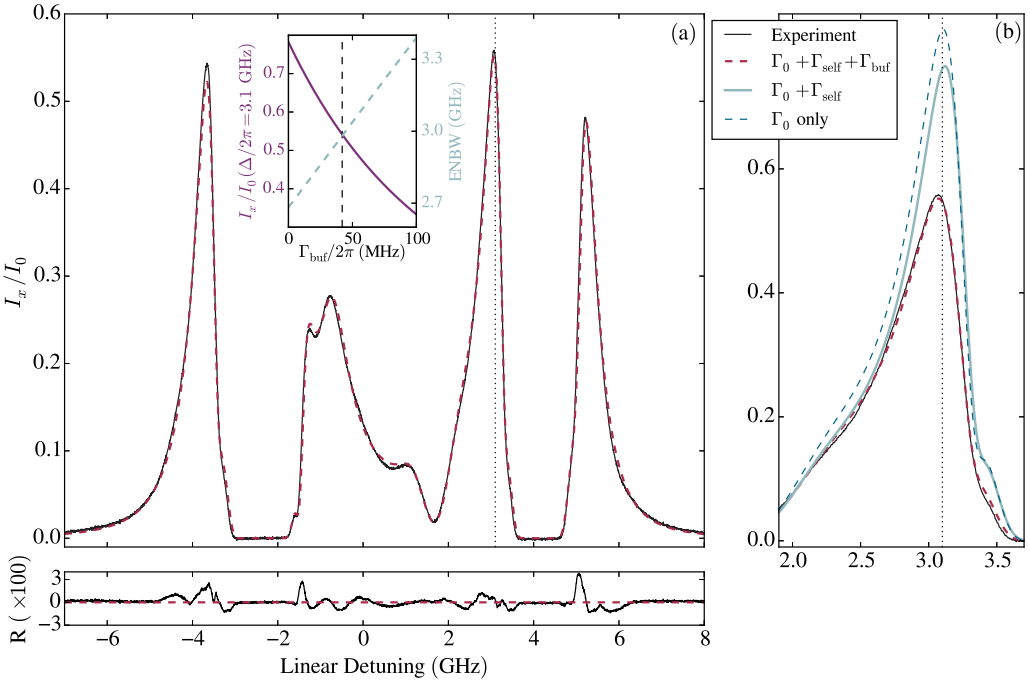

Figure 6.7: Experimental and theoretical Faraday-filter spectra on the rubidium D_2 line as a function of linear detuning ($\Delta/2\pi$) from the weighted line-centre (384.23042812 THz [144, 164]). A 1 mm length vapour cell was used with an isotopic ratio of 99% ^{87}Rb to 1% ^{85}Rb. The solid black line in panel (a) shows the experimental filter spectrum and the dashed (red) line shows the fit to theory that includes the natural, self, and buffer gas induced (Γ_{buf}) Lorentzian broadening effects. Below panel (a) the residuals, R, (the difference between experiment and theory) are plotted. There is an RMS deviation between experiment and theory of 0.6%. The inset of panel (a) shows the effect of Γ_{buf} on transmission (solid purple line) and equivalent-noise bandwidth (ENBW) (dashed blue line) of theoretical filter spectra. The vertical dashed line marks the amount of buffer gas broadening seen in the experiment. Panel (b) shows a zoomed in region around the peak at 3.1 GHz, including theoretical curves with natural homogeneous broadening only (dashed blue) and with natural and self broadening (solid blue).

The amount of broadening due to buffer gas pressure that we observe, typically corresponds to approximately 1-2 Torr of buffer gas [167, 168]. The fact that this small pressure affects the filter spectra by a large amount shows that the wing-type Faraday filter spectra are very sensitive to buffer gas pressure. It has previously been shown that non-linear Faraday rotation can be a sensitive probe of buffer gas pressure [169], being non-invasive and using simple apparatus. Our results show that it may be possible to use the linear Faraday effect instead, which has the advantage of more easily modelling the effect of buffer pressure. However, it is not yet clear if this is more sensitive than using transmission spectroscopy [170].

6.5 Discussion

We have described an efficient computerized method to optimize the cell magnetic field and temperature for short cell length Faraday filters. From theoretical spectra we see that wing-type filters in particular are deleteriously affected by homogeneous broadening, while line-centre filters are less affected. We perform an experiment to realise a wing-type filter using a micro-fabricated 1 mm length ^{87}Rb vapour cell, and find excellent agreement with theory. While buffer gasses can enhance some signals using vapour cells [171], they should be kept to a minimum in order to achieve the narrowest Faraday filters with the highest transmission.

Chapter 7

A Faraday filter on the Caesium D_1 line

7.1 Introduction

In the previous chapter we looked into how to optimize Faraday filters, and we saw how line-broadening deleteriously affects the performance of the filter. In this chapter we design a filter for a specific application, namely quantum-optics experiments utilizing the caesium D_1 line. Only one Faraday filter on the caesium D_1 line has been previously demonstrated [43], however, few details were provided about the filter itself.

Faraday filters have so far been demonstrated experimentally using neon [52], calcium [172], sodium [48, 50, 51, 98, 157, 173, 174], potassium [64, 129, 175], rubidium [53, 99, 176], and caesium [43, 54, 125]. A Faraday filter on the caesium D_1 line (894 nm) could be useful for quantum optics experiments which utilize the Cs D_1 line [177], and could aid filtering degenerate photon-pairs at 894 nm in a similar way to that shown for 795 nm [69].

This chapter uses the computerized optimization technique (see section 6.3.2) to find optimal working parameters for the Faraday filter. Using this technique we find that a Faraday filter working at the Cs D_1 line has superior performance when compared to similar linear Faraday filters working with different elements and/or transitions. Experimentally, we verify the prediction of the model, and achieve a linear Faraday filter with the best perfor-

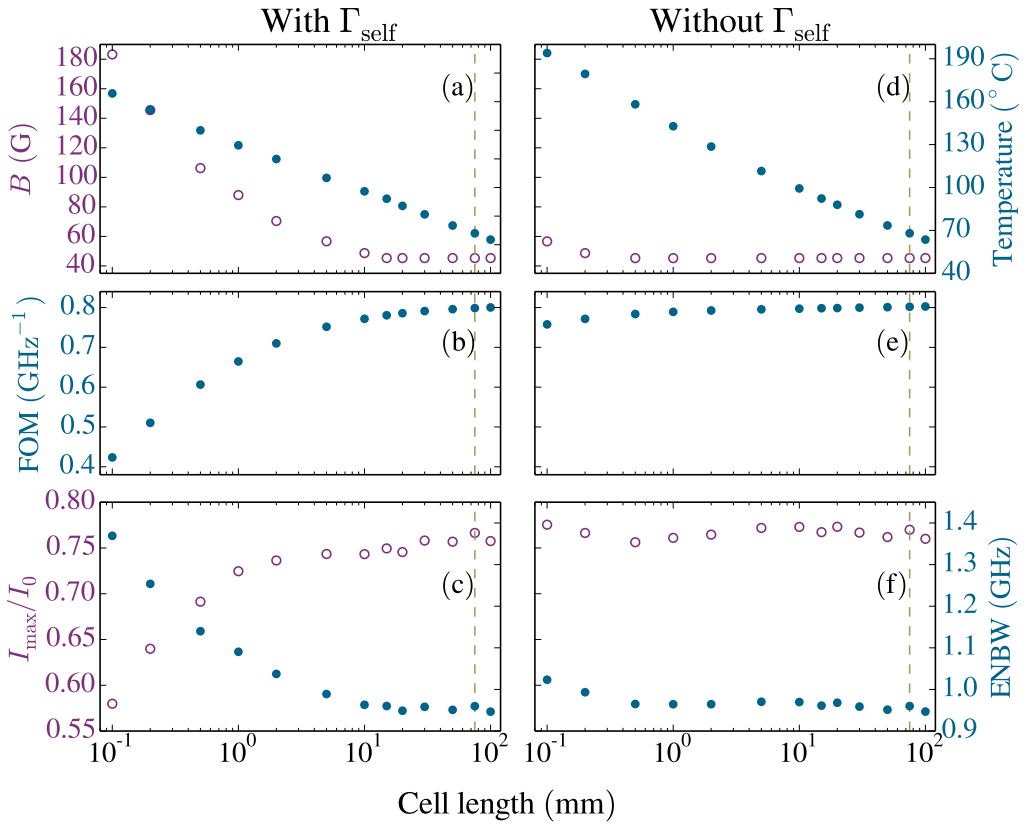

Figure 7.1: Computer optimization of Cs D_1 Faraday filters for different cell lengths. Panel (a) shows the values of the parameters required to maximize the figure of merit (FOM); the hollow (purple) circles show the values of magnetic field while the solid (blue) circles give the temperature. Panel (b) shows the optimum FOM values. Panel (c) shows the corresponding ENBW (solid circles) and I_{max} values (hollow circles). The vertical dashed line marks the length of the experimental cell used to measure the spectrum shown in Fig. 7.3. Panels (d) to (f) are the result of the same optimization but with the effect of self broadening removed.

mance to date.

7.2 Optimization

We use exactly the same computerized optimization technique as described in section 6.3.2. The figure of merit used was that of equation (6.2). This technique used a few thousand evaluations of the filter spectrum from the ElecSus program, taking less than five minutes to complete using a computer with an Intel® Core™ i3-3220 processor.

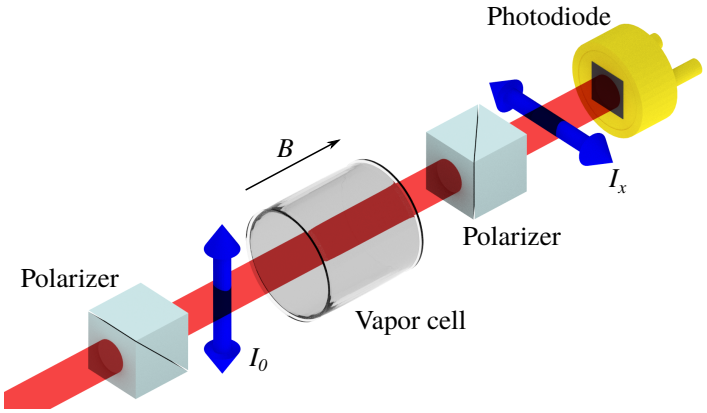

Figure 7.2: Illustration of the experimental arrangement. The vapour cell has an axial magnetic field (B) applied, and is placed between two crossed polarizers. The (blue) arrows denote the polarization of the light. The experiment used a 75 mm long caesium vapour cell.

Panels (a) to (c) of figure 7.1 show the results of the optimization for vapour cell lengths ranging from 100 μm to 10 cm. We can see that for cell lengths above 10 mm, the optimal value of the magnetic field is constant at 45.3 G, while the optimal temperature changes such that the change in number density [6] ($\mathcal{N}$) compensates the change in cell length (L) in a predictable way; $\mathcal{N}L \approx$ constant. However, for cell lengths of 10 mm and less, the optimal magnetic field changes. This is due to self broadening [91] becoming important at higher densities, having a greater effect than Doppler broadening, as discussed in chapter 6. This was was confirmed by repeating the optimization with the effect of self broadening removed; shown in panels (d) to (f) of figure 7.1.

7.3 Experiment

To validate the prediction of the model, an experiment using a 75 mm long Cs vapour cell (similar to that shown in figure 4.1) was performed. Figure 7.2 shows an illustration of the experimental arrangement. The vapour cell was placed in the solenoid as described in section 4.1.1 which produced an axial magnetic field and provided heating of the vapour cell. To measure the filter spectrum a continuous wave Ti:sapphire laser was used to produce a beam of light that could be scanned across the Cs D_1 line. The laser scan was calibrated using the method described in section 4.3.

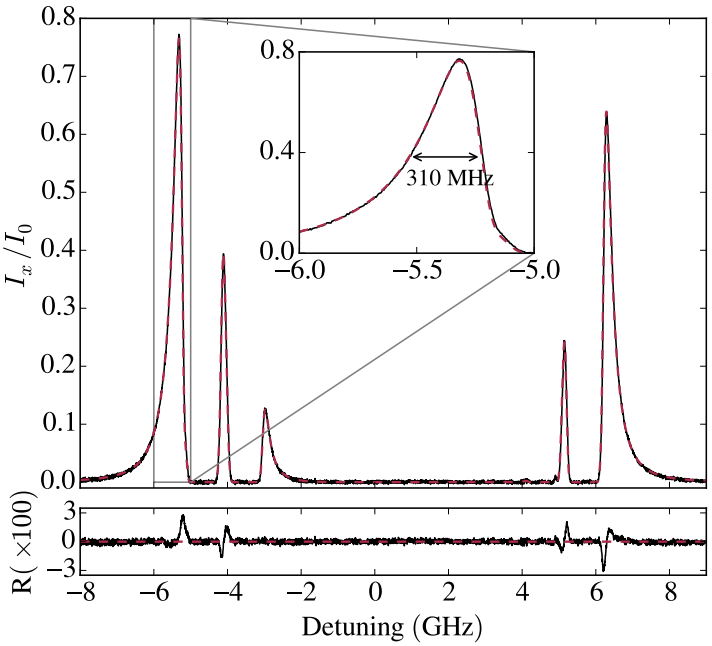

Figure 7.3: Transmission through a Cs D_1 Faraday filter with a 75 mm long atomic medium as a function of linear detuning from the weighted linecentre (335.116048807 THz [178]). The solid back line shows the experimental data while the dashed (red) line is the theory fit. From the fit, the cell temperature and magnetic field are found to be (67.8 ± 0.3)°C and (45.7 ± 0.8) G respectively. The ENBW was found to be (0.96 ± 0.01) GHz and the maximum transmission was (0.76 ± 0.01). Plotted underneath are the residuals (R) between experiment and theory, with a root mean square (RMS) deviation of 0.4%, showing excellent agreement.

Figure 7.3 shows the measured Faraday filter spectrum and a theory fit using ElecSus [72]. Excellent agreement is found between theory and experiment. The full width at half maximum of the passband was found to be 310 MHz, while the ENBW and I_{max}/I_0 were found to be (0.96 ± 0.01) GHz and 0.76 ± 0.01 respectively; in agreement with the theoretical optimum values. This gives a ratio of I_{max}/I_0 to ENBW (FOM) of $(0.794 \pm 0.015)\,\mathrm{GHz}^{-1}$, which, to the best of our knowledge, is the highest demonstrated to date for any linear Faraday filter.

Atom (λ [nm])	B [G]	T [°C]	ENBW [GHz]	I_{max}/I_0	FOM [GHz^{-1}]
Na (589)	128	191	3.1	0.78	0.25
Na (590)	169	198	3.3	0.80	0.24
K[1] (766)	76.3	107	1.8	0.80	0.44
K[1] (770)	92.2	113	1.8	0.82	0.45
^{85}Rb (780)	223	54.4	2.1	0.96	0.45
^{85}Rb (795)	63.8	79.8	1.1	0.75	0.66
^{87}Rb (780)	67.3	64.5	2.0	0.79	0.39
^{87}Rb (795)	61.0	82.4	1.1	0.72	0.67
Rb[1] (780)	53.4	84.1	2.3	0.91	0.40
Rb[1] (795)	72.3	88.6	1.4	0.76	0.53
Cs (852)	55.6	47.2	1.6	0.79	0.51
Cs (894)	45.3	68.0	0.96	0.77	0.80

Table 7.1: Prediction of the optimal values of magnetic field (B) and temperature (T) by computer optimization for different atoms and transition wavelengths (λ). Each atomic medium was set to 75 mm long. The caesium D_1 filter, realized in this work (see Fig. 7.3), shows by far the highest ratio of maximum transmission to ENBW (FOM).

7.4 Comparison with other elements and D lines

The computer optimization was also performed for both D lines of sodium, potassium, rubidium and caesium, for a 75 mm long atomic medium. From Table 7.1, we can clearly see that caesium D_1 line gives the highest FOM value. We also find that the performance of rubidium D_1 line filters [99] could be improved further by using an isotopically pure vapour. One thing to note is that, with the exception of ^{85}Rb at 780 nm, the filter spectra that give the highest FOM value all show 'wing' type operation, where the filter transparencies occur just off-resonance from the atomic transitions. Line-centre operation [157] is found for local FOM maxima (as shown in figure 6.1 in chapter 6.3.4).

[1] At natural abundance [163].

7.5 Discussion

In conclusion, we have introduced Faraday filtering on the caesium D_1 line. The filter shows excellent performance, surpassing other elements and transitions, and could find use in quantum optics experiments. The method used to find the optimal magnetic field and temperature is fast and simple, utilizing publicly available software [72] and could be applied for other figures of merit for other applications.

This type of filter is designed primarily for quantum-optics experiments. Very recently another study has been completed which designs a caesium D_1 line filter for photon emission from quantum dots [179]. This further motivates the use of Faraday filters for quantum-optics experiments in general.

Chapter 8

An external cavity diode laser with an intra-cavity Faraday filter

8.1 Introduction

In chapters 6 and 7 we introduced the concept of Faraday filtering and designed a Faraday filter primarily for the purpose of quantum-optics experiments. In this chapter we will look into using a Faraday filter for laser frequency stabilization. Unlike in chapter 5 where laser frequency error signals were created in an external cell, this chapter will look into putting a Faraday filter into the cavity of a diode laser. The technique of putting a Faraday filter in a laser cavity is one of the first applications of a Faraday filter, having been used to frequency stabilize dye lasers [50–52]. In recent years the same technique has been applied to diode lasers [60–62, 180].

External cavity diode lasers (ECDL) are used extensively for many applications where the laser frequency needs to be controlled and the line-width needs to be small. For example, a grating can be used as a frequency-selective element that creates the external cavity [181]. The position of the grating can then be adjusted to change the frequency of the laser. This method typically creates free-running line-widths of less than 1 MHz, which can be reduced when electronically stabilising against an external frequency refer-

ence [182]. However, the precise position of the grating is critical, which means that this type of ECDL is susceptible to vibrations. Also, changes in temperature or diode current can change the laser frequency substantially. There is, therefore, a need for an external reference to measure the frequency of the laser.

These issues are solved by using a Faraday filter as the frequency selective element of an ECDL, while compromising on tunability. Previous implementations of this technique [60, 61] were able to ensure the laser frequency did not mode hop more than a few tens of GHz. A recent experiment [62] showed that the laser frequency can stay within a single filter transparency ($\sim$ 1 GHz) even when the laser's temperature and current are changed by $\sim 20^{\circ}$C and ~ 90 mA respectively. However, due to the presence of multiple cavity modes within the filter profile, mode hops caused frequency jumps of ~ 400 MHz. Also, since the cavity length was not stabilized, the laser will have exhibited long term frequency drift. One method to reduce the range of frequency jumps is by using a very long cavity such that the cavity free-spectral range is short [183], thereby leaving a cavity mode near the peak of the filter transmission at all times. This technique also has the advantage that the length of the cavity does not need to be actively stabilized. However, one drawback is that this technique does not eliminate mode hops.

We demonstrate another technique; to use a short cavity length such that there is only one cavity mode within the filter transparency. In this way, mode hops are eliminated. The compromise is that the cavity length must be stabilized for long term frequency stability. We use an external Faraday rotation signal as a laser frequency error signal, however, in principle the frequency can be stabilized by monitoring power of the laser output. Therefore, there should be no need for an external reference.

To be useful for typical atomic physics applications (such as laser cooling), the frequency noise of the laser (characterized by the laser line-width [184]) should be much smaller than the atomic natural line-width. Optical heterodyne detection [185] was used to measure the beat note between the laser and a different grating based ECDL, concluding that the laser linewidth is less than 850 kHz.

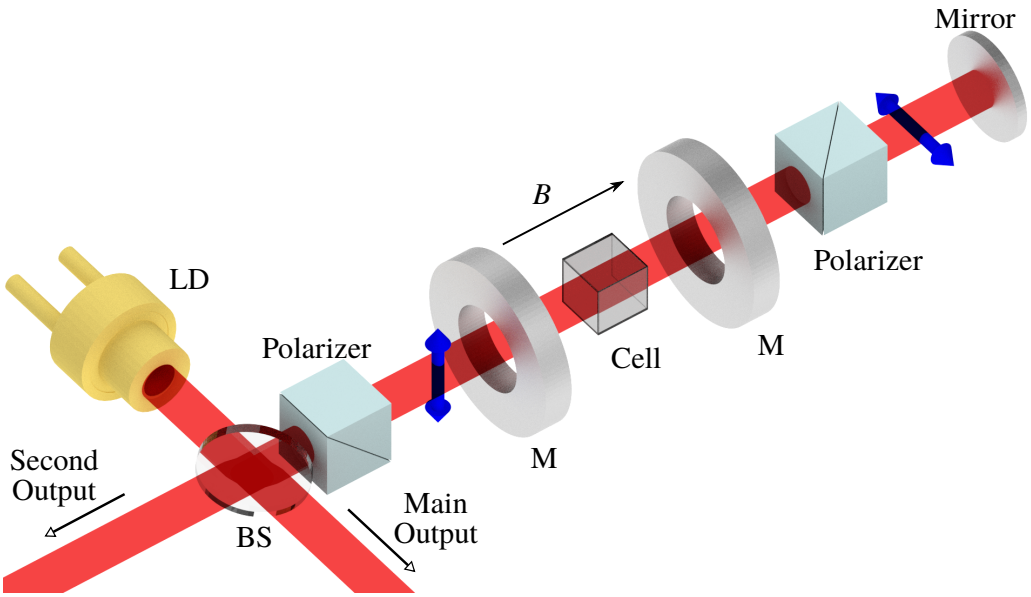

Figure 8.1: Illustration of the experimental arrangement of an external cavity diode laser utilizing a Faraday filter as the frequency selective element. LD – laser diode, M – magnet, B – magnetic field, BS – Beam splitter.

8.2 Background and theory

The working principle of an external cavity diode laser (ECDL) is that a portion of the light is fed back into the laser diode by a frequency selective element. For a Faraday-filter laser this is done by passing a portion of the light through an intra-cavity Faraday filter and then feeding this back into the laser diode. Figure 8.1 shows an illustration of one possible arrangement of a Faraday-filter laser. A beam splitter is placed after the laser diode which allows some light to pass through whilst the reflected light passes though a Faraday filter. This light is then reflected back through the same Faraday filter before being incident again on the beam splitter. A portion of the beam then reflects back into the laser diode. Note that in addition to the Faraday filter, frequency selectivity is provided from the external cavity formed between the laser diode to the mirror. This is due to the fact that only integer wavelengths can be supported within an optical cavity. These cavity modes therefore occur periodically in frequency.

If the frequency spacing between cavity modes (known as the free-spectral range) is large enough, we can ensure that only one cavity mode is supported within the filter bandwidth. This prevents the laser spontaneously jumping

to another cavity mode (a mode hop), which otherwise might occur due to small fluctuations such as acoustic vibrations or diode current fluctuations etc. We can approximate the length of the cavity (D) required by assuming a plane-parallel cavity and using the equation [186]

$$\Delta\nu = \frac{c}{2nD}, \tag{8.1}$$

where $\Delta\nu$ is the free-spectral range. Note that we can define an effective length $D_{\text{eff}} \equiv nD$, which takes into account the refractive index of the medium within the cavity. The effective length can also be built up in parts if there are media of different refractive indices between the cavity mirrors. Since the passband of a typical Faraday filter is of the order of 1 GHz, putting this into equation (8.1) and rearranging gives $D_{\text{eff}} \approx 15\,\text{cm}$. This approximates the longest possible cavity length before multiple modes are passed by the filter.

8.3 Faraday-filter laser design

8.3.1 Experimental arrangement

An anti-reflection (AR) coated laser diode was chosen since this simplifies the situation by removing the internal laser diode cavity. This in turn means that the laser diode has much more of a broadband emission profile when compared to non-AR coated laser diodes, removing the need for heating or cooling the diode [61] to tune its emission characteristics.

Figure 8.1 shows an illustration of the experimental arrangement. The beam from the laser diode was collimated using an aspheric lens (not shown) and was then incident on a beam splitter. The beam splitter transmits approximately 80% of light and reflects the remainder. The transmitted beam is the main output of the laser system since it contains the majority of the output power. The reflected beam passed through a $5 \times 5 \times 5\,\text{mm}^3$ polarising beam splitter cube (PBS1), ensuring it was linearly polarized in the vertical direction. The beam then passes through a naturally abundant rubidium vapour cell with an internal path length of 5 mm. The cell was placed in an

oven which provided heating. Ring magnets apply a magnetic field across the vapour cell of which the non-uniformity is less than 2%. After travelling through the atomic vapour, the polarization of the laser beam was rotated by $\pi/2$ and then passed through a second cube polarizer (PBS2) crossed with the first. The beam was then reflected back over the same path using a mirror. After travelling through the atomic vapour for the second time, the polarization of the beam rotated by a further[1] $\pi/2$ and passed through PBS1. The beam is then incident on the beam splitter, where the transmitted beam gives a secondary output and the reflected beam feeds back into the laser diode. The length of the external cavity (from the laser diode to the mirror) was 52 mm; this gives an effective cavity length of approximately 60 mm once the refractive indices (approximated as 1.5) are taken into account for the PBS cubes and the cell windows. Therefore, using equation (8.1), $\Delta\nu \approx 2.5\,\text{GHz}$. The cavity mirror is mounted on a piezoelectric transducer, which allows fine adjustment of the cavity length (up to $\sim 1\,\mu\text{m}$). This serves to shift the cavity resonances by up to $\sim 3\,\text{GHz}$.

Both PBS cubes, the vapour cell and the collimating lens were all AR coated. This is to minimize losses and ensure the external cavity dominates the feedback into the laser diode.

8.3.2 Filter-profile design

We desire a filter profile that is as narrow as possible whilst consisting of only one large transparency. Also, the filter should transmit as much light as possible so that the feedback to the diode is efficient. It is also desirable, for practical reasons, for this to occur for relatively small magnetic fields and temperatures. Figure 8.2 shows a Faraday filter spectrum, found using ElecSus [72], which shows all of the desired characteristics. The peak transmission feature has a full-width at half-maximum of 0.6 GHz, which is much less than the cavity free-spectral range of 2.5 GHz. Therefore we expect multi-mode behaviour to be greatly suppressed.

[1]Note that the beam rotates further rather than being rotated back to its previous polarization. It makes little difference in this context but for applications such as optical isolators [29], this distinction is crucial.

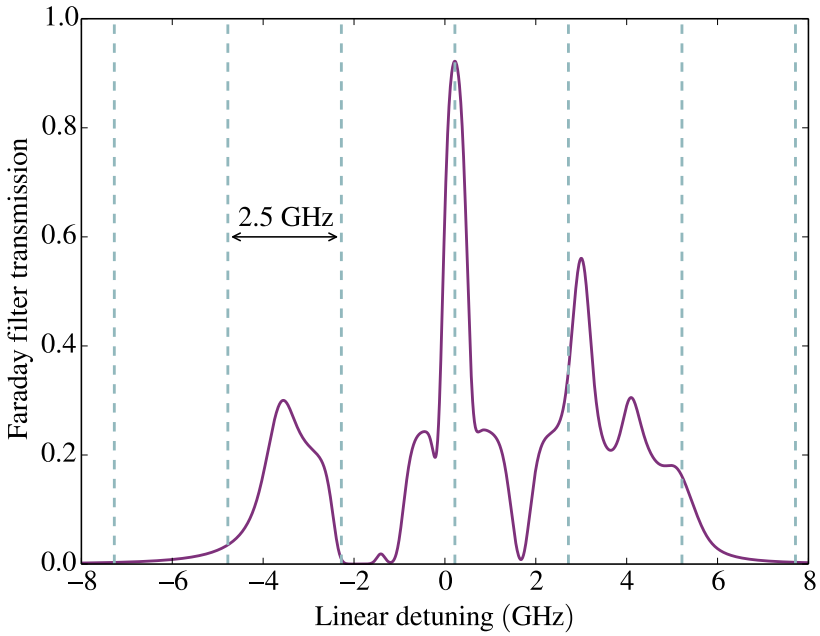

Figure 8.2: Theoretical filter transmission (solid purple line) as a function of linear detuning from the Rubidium D_2 weighted line centre. Simulated is a 5 mm long rubidium vapour at natural abundance with an axial magnetic field of 240 G and a temperature of 93°C. The vertical dashed-blue lines represent the cavity modes, with a free-spectral range of 2.5 GHz corresponding to a 60 mm long effective cavity length. [*Optimal magnetic field and temperature values were found by Renju S. Mathew.*]

8.4 Measuring the filter spectrum

In order to measure the filter spectrum experimentally the arrangement described in section 8.3.1 was slightly modified. The laser diode was replaced by a photodiode, and then a weak-probe laser beam was sent through the filter (backwards against the arrow denoting the second output in figure 8.1). The laser beam was from a grating based ECDL, and the frequency was scanned across the rubidium D_2 weighted line-centre (see appendix B.2). The frequency of the laser beam was calibrated using the method described in section 4.3. The signal measured on the photodiode represents the intensity of light after two passes through the filter. This 'double pass' signal is convenient to measure whilst also being a more natural measure of the filter's affect on the laser light, since any light that is fed back into the laser must make at least two passes through the filter.

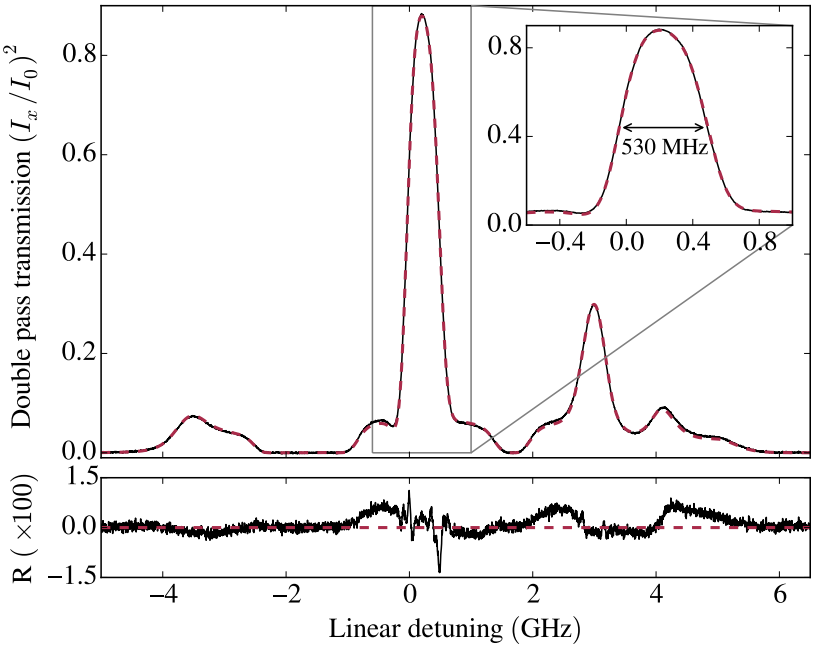

Figure 8.3: Experimental (black solid line) and theoretical (dashed red line) transmission spectra after two passes through the Faraday filter. The fit parameters were the magnetic field and temperature and were found to be (235.73 ± 0.15) G and (91.82 ± 0.04)°C respectively. Plotted underneath are the residuals (R) between experiment and theory. The root-mean-square deviation between experiment and theory is 0.2%. The inset shows the spectrum zoomed into the main transmission feature, which has a full-width at half-maximum of 530 MHz.

Figure 8.3 shows the experimental double pass transmission spectrum along with a fit using ElecSus [72]. Five spectra were taken in quick succession (only one shown) and were independently fit to theory using the random-restart routine in ElecSus. The mean values of the fitted magnetic field and temperature were found to be (235.73 ± 0.15) G and (91.82 ± 0.04)°C respectively, where the uncertainties represent the standard error [118]. Note that, in a similar way to the results of chapter 5 (see section 5.5), these statistical uncertainties are likely to be much smaller than the systematic uncertainties.

8.5 Laser-linewidth measurements

Optical heterodyne detection is a common way to characterize the frequency noise of laser systems. The technique involves superimposing beams from two lasers and detecting the resulting beat-note in intensity. The distribution of beat-note frequencies over time characterizes the combined frequency noise in the two laser [181].

8.5.1 Background on optical heterodyne detection

The superimposed electric field from two collimated laser beams with differing angular frequencies ω_1 and ω_2, and wavenumbers k_1 and k_2, can be written as [186]

$$\boldsymbol{E}(x,y,z,t) = \boldsymbol{E}_1(x,y)\cos(k_1 z - \omega_1 t) + \boldsymbol{E}_2(x,y)\cos(k_2 z - \omega_2 t + \phi), \quad (8.2)$$

where ϕ is an arbitrary phase shift, and the amplitudes $\boldsymbol{E}_1(x,y)$ and $\boldsymbol{E}_2(x,y)$ represent the transverse pattern of the two beams as well as their polarization. The power of this combined beam on a photodetector (choosing the position to be at $z = 0$) will be given by

$$P(t) \propto \iint \boldsymbol{E}^2(x,y,t)\mathrm{d}x\mathrm{d}y \quad (8.3)$$

$$\propto P_1\cos^2(-\omega_1 t) + P_2\cos^2(-\omega_2 t + \phi) + 2P_{12}\cos(-\omega_1 t)\cos(-\omega_2 t + \phi), \quad (8.4)$$

where P_1, P_2 and P_{12} are given by

$$P_1 = \iint \boldsymbol{E}_1^2(x,y)\mathrm{d}x\mathrm{d}y, \quad (8.5)$$

$$P_2 = \iint \boldsymbol{E}_2^2(x,y)\mathrm{d}x\mathrm{d}y, \quad (8.6)$$

$$P_{12} = \iint \boldsymbol{E}_2(x,y)\cdot\boldsymbol{E}_1(x,y)\mathrm{d}x\mathrm{d}y. \quad (8.7)$$

After using a suitable trigonometric identity[2] we get,

$$P(t) \propto P_1 \cos^2(-\omega_1 t) + P_2 \cos^2(-\omega_2 t + \phi) + P_{12}(\cos([\omega_2 - \omega_1]t - \phi) + \cos(-[\omega_1 + \omega_2]t + \phi)), \quad (8.8)$$

Photodetectors in general have limited detection bandwidths and therefore terms which oscillate at optical frequencies (ω_1, ω_2 and $\omega_1 + \omega_2$) are typically detected as an average, dc voltage. Therefore the signal we expect from a photodetector is a constant signal modulated by a sinusoidal wave with frequency, $\omega_{\text{beat}} = \omega_2 - \omega_1$, known as the beat-note.

8.5.2 Laser line-width from ω_{beat} distribution

If the individual frequencies ω_1 and ω_2 have statistical fluctuations over time, then we will measure fluctuations in ω_{beat}. Assuming the fluctuations in the two frequencies are independent we can write the probability density function of ω_{beat} as [187]

$$\begin{aligned} f_{\text{b}}(\omega_{\text{beat}}) &= \int_{-\infty}^{\infty} f_1(\omega_{\text{beat}} - \omega_2) f_2(\omega_2) \mathrm{d}\omega_2 \\ &= \int_{-\infty}^{\infty} f_1(\omega_1) f_2(\omega_{\text{beat}} - \omega_1) \mathrm{d}\omega_1, \end{aligned} \quad (8.9)$$

where f_1 and f_2 are the probability density functions of ω_1 and ω_2 respectively. This result is the convolution of the individual probability density functions. If one of the laser beams has very small frequency fluctuations compared with the other then then we can make the approximation, $f_{\text{b}}(\omega_{\text{beat}}) \approx f_1(\omega_1)$, since this gives the approximation $f_2(\omega_2) \approx \delta(\omega_2)$, where δ represents the Dirac delta distribution. Therefore the laser line-width will be given by the FWHM of $f_{\text{b}}(\omega_{\text{beat}})$.

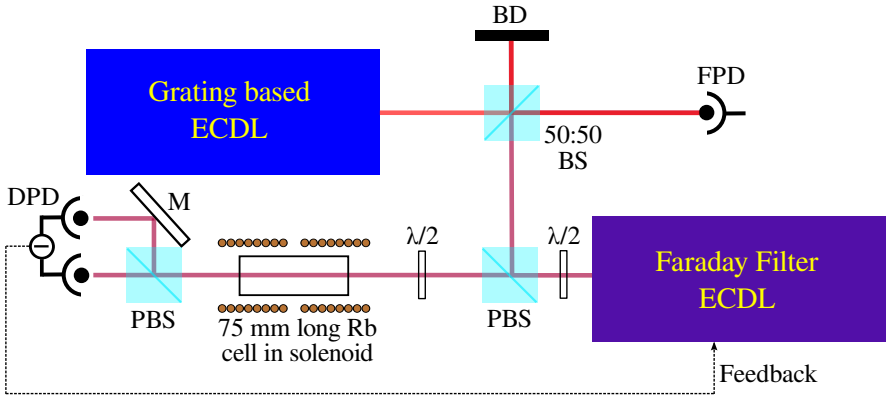

Figure 8.4: Illustration of the heterodyne detection experiment. M – mirror, BD – beam dump, FPD – fast photodetector, DPD – differencing photodetector, BS – beam splitter, PBS – polarizing beam splitter, $\lambda/2$ – half-wave plate. ECDL – external-cavity diode-laser. A beam from the Faraday-filter laser is incident on a PBS. The reflected beam is overlapped with a beam from the grating based ECDL using a 50:50 BS. This combined beam is detected using an FPD. The beam from the Faraday-filter laser which was transmitted through the first PBS is used to make a laser-frequency error signal, which was used to stabilize the laser detuning to $\Delta/2\pi \approx 0.2\,\text{GHz}$ from the weighted rubidium D_2 line centre.

8.5.3 Optical heterodyne detection experiment

A schematic of the optical heterodyne experiment is given in figure 8.4. For this experiment another laser beam is required. A grating based ECDL [188] (Toptica DL 100) was used. This laser was frequency stabilized, using polarization spectroscopy [189] (not shown in figure 8.4), to a detuning from the rubidium weighted line centre of $\Delta/2\pi \approx -1.2\,\text{GHz}$. The Faraday-filter laser was also frequency stabilized using an external atomic reference. This was done by using a portion of the beam from the output, making it linearly polarized at a 45° angle to the x-axis, before being passed through a 75 mm long Rb vapour cell in a solenoid (described in section 4.1.1). The solenoid provides heating of the cell as well as an axial magnetic field. After the vapour cell, the beam is incident on a PBS which splits the beam into I_x and I_y components. A differencing photodetector measures $I_x - I_y$ (proportional to S_1) and this signal is used as an error-signal which is fed back to the laser to keep its frequency stabilized to a detuning value of $\Delta/2\pi \approx 0.2\,\text{GHz}$. This

[2] $2\cos\Theta_1\cos\Theta_2 \equiv \cos(\Theta_1 - \Theta_2) + \cos(\Theta_1 + \Theta_2)$

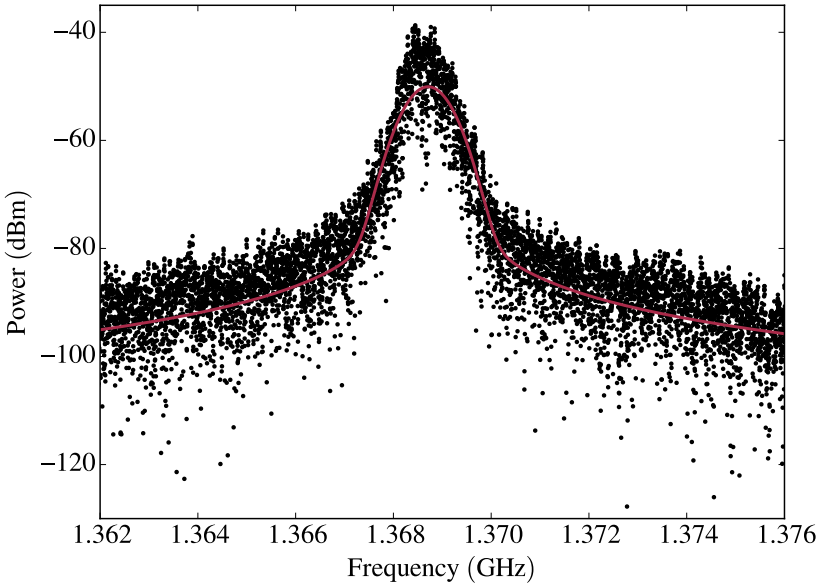

Figure 8.5: Power spectrum of the beat-note signal between the two lasers. The black dots represent the experimental data, while the solid red line is the fit to a Voigt profile. From the fit, the Gaussian full-width at half-maximum (FWHM) was found to be 0.84 MHz while the Lorentzian FWHM was 0.01 MHz.

feedback works by sending the error signal to a PID controller, which outputs a voltage to the piezoelectric transducer placed behind the cavity mirror.

Another beam from the Faraday-filter laser was overlapped with the beam from the grating based laser using a 50:50 non-polarizing beam splitter cube (see figure 8.4). This combined beam was then incident on a fast photodetector. The photodetector has an AC-coupled output and a bandwidth up to $\sim 1.2\,\text{GHz}$. Therefore the photodetector will only measure the beat-note term of equation (8.8). Also despite the 1.2 GHz upper bound on the bandwidth of the detector (as quoted by the manufacturer), we found that the beat-note was detectable up to frequencies of approximately 2 GHz.

A 0.5 ms long signal from the photodetector was measured on an oscilloscope (LeCroy WaveRunner 625Zi), with a sampling resolution of 40 GS/s and an analogue bandwidth of 2.5 GHz. The power spectrum of this signal was calculated using the FFT function of the oscilloscope. The power spectrum showed a single clear peak, indicating that both lasers were exhibiting single mode behaviour within the detection bandwidth. Figure 8.5 shows the power

spectrum zoomed in around the peak. A Voigt profile was fitted to the spectrum which had a full-width at half-maximum (FWHM) of 0.85 MHz. We can therefore conclude that the Faraday-filter laser must have a linewidth of less than 0.85 MHz. This linewidth is small enough to be useful for many atomic physics experiments where the laser linewidth should be ideally be less than the natural line-width of the D lines ($\sim 6\,\mathrm{MHz}$).

8.6 Discussion of potential improvements

The Faraday-filter laser has been shown to work with a sufficiently small linewidth. However, it is not yet clear what the exact line-width value is since the beat-note measurement may be limited by the line-width of the grating-based ECDL system. Further work can be done to find out the absolute line-width, either by introducing a third laser so that three beat-note measurements can be taken[3] or by building an identical Faraday-filter laser system which can be assumed to have the same linewidth.

Another improvement would be to use the power output of the laser to stabilize the frequency, rather than using an external reference. This is possible because the amount of optical feedback to the laser diode is dependent on frequency (due to the intra-cavity Faraday filter). When there is the most optical feedback, there should correspondingly be the most optical output power from the laser. Therefore, we can keep the frequency stable by ensuring the cavity mode frequency coincides with the maximum filter transmission.

Figure 8.6 shows the power of the laser output as a function of frequency, along with the measured weak-probe filter spectrum. We can see that the peak power does not coincide with the peak of the weak-probe filter profile, which may indicate that the beam inside the filter's vapour cell is not in the weak-probe regime. Since the weak-probe filter spectrum is not a good measure of the filter spectrum, we expect that the frequency of peak transmission of the filter is a function of intensity. Unfortunately, this means that adjusting the cavity length in order to maximize the output power may not result

[3] If we assume either a Gaussian or Lorentzian beat-note distribution then equation (8.9) can be deconvolved. The three beat-note measurements would then give a set of three linear equations which can be solved to find the line-width of each laser.

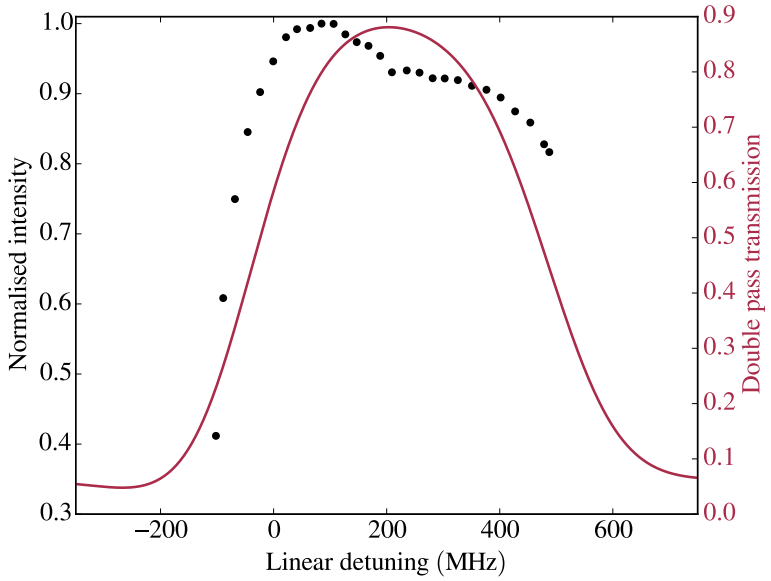

Figure 8.6: The solid back dots show the laser beam intensity (normalized) while the solid red line shows the previously measured (weak-probe) filter spectrum. Both curves are plotted against linear detuning ($\Delta/2\pi$) from the rubidium weighted line centre.

in a unique frequency. A preliminary experiment of this kind showed that the laser exhibits long term drift of ~ 10 MHz over tens of hours. This indicates that further work needs to be done to reduce the intensity of the beam within the vapour cell of the filter. This could be achieved by expanding the size of the beam.

8.7 Discussion

This chapter demonstrates a short cavity length Faraday-filter laser, such that a single cavity mode exists within the filter's passband. We have used an external atomic signal as a reference, however, it should be possible to stabilize the frequency using only the power output of the laser. No external reference is required in principle.

Further work to improve the long term stability of the laser system is ongoing.

Chapter 9

Slow-light pulse propagation

9.1 Introduction

There has been much interest in recent years in the phenomenon of slow light [190]. It is characterized by the situation where the light pulse velocity is much less than that of continuous-wave (CW) light, and is realized in systems where there is a large derivative of the refractive index with respect to frequency. The slow-light effect increases the amount of time a light pulse spends in the medium, and so can enhance processes such as all optical switching [131], image rotation [191] and optical delay lines [192]. A slow-light medium can also increase the sensitivity of interferometers [193]. When combined with the Faraday effect, a slow-light pulse placed off-resonance can act as a sensitive atomic probe [194]. Electromagnetically-induced transparency (EIT) [195] is often used to create large pulse delays [196, 197] due to the extremely (spectrally) narrow transparencies that can be achieved. However, one drawback is the requirement for pulses with low bandwidth to avoid distortion, which corresponds to relatively long (of the order of a microsecond) pulses. For communication purposes, shorter pulses mean more information can be sent in any given time.

In this chapter we look at applying our model (as described in chapter 2) for the electric susceptibility (χ) to describe slow light. So far we have only considered CW beams; in fact χ was calculated using the steady-state solution to the optical Bloch equations. As such it could be expected that the

model is invalid for short pulses of light. However, in this chapter we will experimentally provide some evidence that our model for χ is still valid.

The key is noting that a pulse of light can decomposed (using a Fourier transform) into a collection of continuous sinusoidal waves. Each one of these waves will have its own attenuation and phase shift which we can calculate using ElecSus. We then simply do the reverse Fourier transform to reconstruct the pulse that would be seen after traversing the medium. This section describes in detail an experiment to test the model for pulse propagation.

It should be noted that similar experiments were performed previously in [198], but the agreement with theory started to deviate for large optical depths. It was proposed that this may simply be due to the experiment being carried out beyond the weak-probe regime. In this section we show excellent agreement between theory and the results of an experiment carried out at large optical depth but for much weaker pulse intensities.

9.2 Theory

Consider a time varying intensity profile, $I(z = 0, t)$, which is measured before entering an atomic medium. Assuming a single polarization component, we can relate the intensity with the magnitude of its electric field using equation (2.5). This gives us a measurement of the modulation. We can reconstruct the form of the electric field[1] if we know the carrier frequency, as illustrated in panel (a) of figure 9.1. Given this initial electric field at the front of the medium, $E(z = 0, t)$, we perform a Fourier transform to find the electric field in terms of angular frequency,

$$\tilde{E}\left(z = 0, \omega\right) = \frac{1}{\sqrt{2\pi}} \int_{-\infty}^{\infty} E(z = 0, t) \exp(-\mathrm{i}\omega t) \mathrm{d}t. \tag{9.1}$$

Recalling equations (2.1) to (2.4), we can find the electric field at an arbitrary depth z by multiplying this result by $\exp(\mathrm{i}k(\omega)z)$ (where $k(\omega)$ can be

[1] Strictly speaking we still cannot reconstruct the phase of the electric field, but this does not affect the results.

calculated for the atomic medium using ElecSus). Setting $z = \ell$ gives us the pulse angular frequency profile at the exit of the medium. We can then use the reverse Fourier transform[2] to construct the electric field as a function of time at $z = \ell$,

$$E\left(z = \ell, t\right) = \frac{1}{\sqrt{2\pi}} \int_{-\infty}^{\infty} \tilde{E}(z = L, \omega) \exp(\mathrm{i}\omega t) \mathrm{d}\omega. \tag{9.2}$$

Now we can again use equation (2.5) to reconstruct the pulse intensity, and hence predict what would be measured by a detector after the atomic medium. Note that since our medium is circularly birefringent and dichroic, we simply perform the previous procedure for each circular polarization component independently.

Figure 9.1 illustrates the procedure. After the pulse is constructed (see panel (a)) the Fourier transform is taken. The attenuation due to the medium is shown in panel (b) while panel (c) shows the result of applying this attenuation to the pulse spectrum. This, along with the appropriate phase shift at each frequency, is all that is required to construct the electric field at the output of the medium. Note that the parameters chosen for figure 9.1 closely match those of the experiment (see section 9.4 for the experimental results). The sharp peak of the pulse's spectral magnitude (shown in panel (c)) is the result of the continuous part of the temporal pulse profile.

This treatment is all that is required to describe weak-probe pulse propagation, but there are certain approximations which can be made that provide further insight. Most notably is the concept of the 'group' velocity, which describes the speed a pulse propagates through a medium.

9.2.1 Group velocity and the narrowband approximation

It can be shown, by applying a modulation to a sinusoidal wave (see pages 1–3 in [200]), that while the phase velocity of a carrier wave propagates at

[2]The occurrence of negative frequencies is a mathematical construct associated with using a complex field (see pages 24 to 25 in [199])

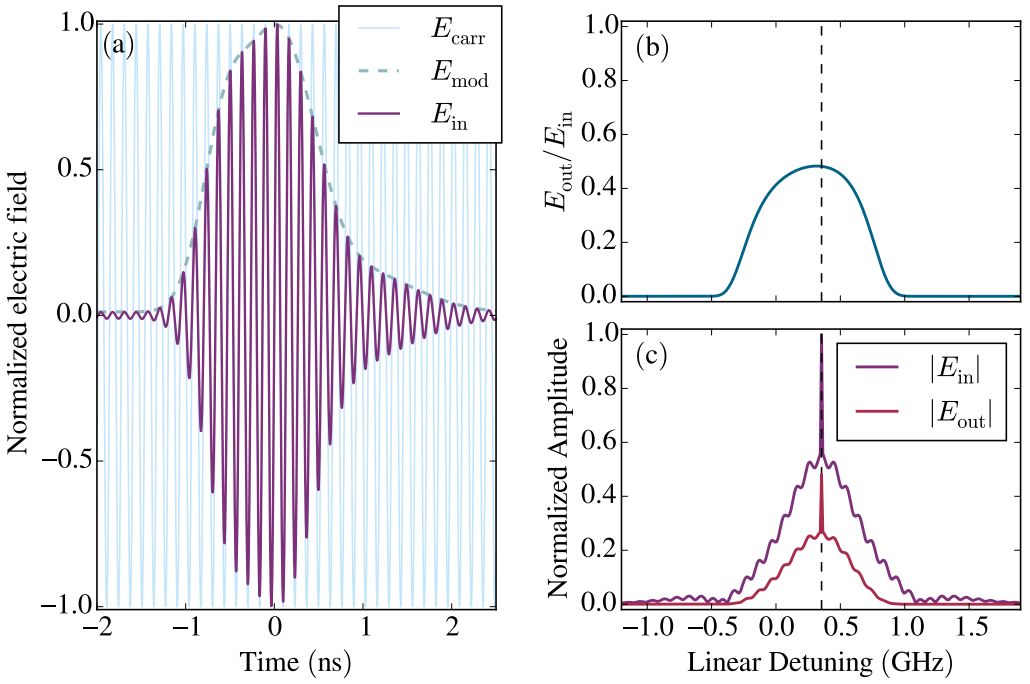

Figure 9.1: Panel (a) shows the electric field of the carrier E_{carr}, modulation E_{mod} and the resultant $E_{\text{in}} = E_{\text{mod}}E_{\text{carr}}$. Note that the angular frequency of E_{carr} has been divided by 5×10^4 for illustration purposes. The solid purple line in Panel (b) shows the magnitude of the Fourier transform of E_{in} as a function of linear detuning ($\Delta/2\pi$). The output electric-field amplitude (E_{out}) is the solid red line and is found from the input electric-field amplitude (E_{in}) multiplied by the ratio $E_{\text{out}}/E_{\text{in}}$. The ratio is plotted in panel (b) and is calculated using ElecSus. The ratio is equivalent to the square root of transmission.

$v_p = \omega/(nk_0)$, the modulation moves with a velocity $v_g \equiv c/n_g$, where

$$n_g(\omega) = n(\omega) + \omega\frac{\mathrm{d}n(\omega)}{\mathrm{d}\omega}. \tag{9.3}$$

This can be a useful quantity when we want to estimate the speed of pulse propagation. We can see from equation (9.3) that the speed of the pulse can be very different from the phase velocity when there is a large gradient in n. Even in an atomic gas where $|n| \approx 1$ a pulse can be slowed by almost an arbitrary amount [196] or made to travel faster [151, 201] by tuning the gradient in n.

However, when the group velocity changes significantly over the pulse bandwidth, and/or there is differing absorption over the bandwidth, the group

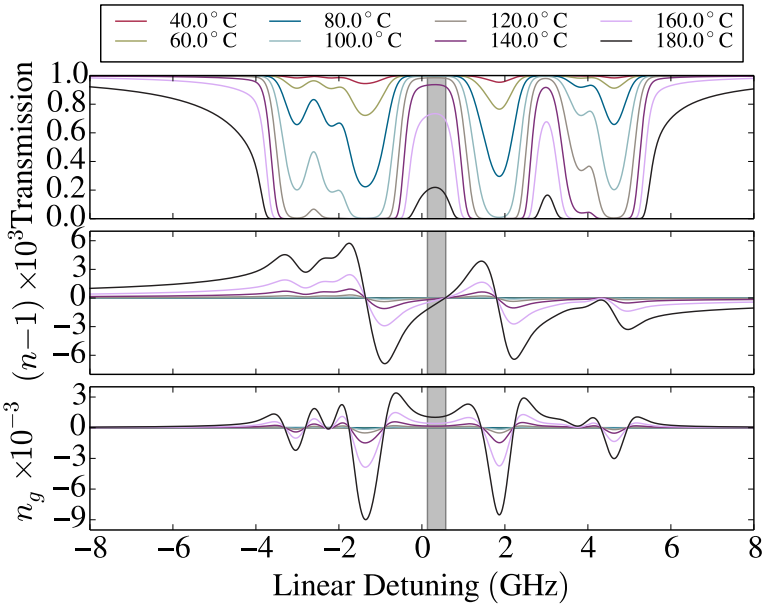

Figure 9.2: Transmission, refractive index (n) and group index (n_g) against linear detuning ($\Delta/2\pi$) from the rubidium D_1 linecentre frequency. The atomic vapour was modelled at natural abundance with a path length of 2 mm. The grey shaded region represents the pulse bandwidth of a Gaussian pulse with a 1 ns full-width at half maximum.

velocity is not well defined. This is because the pulse will distort significantly. Therefore the concept of group velocity is tied into the 'narrowband' approximation, where we can ascribe a single transmission value across the pulse bandwidth, and derivatives of n at higher than first order are negligible.

For our experiment, the narrowband approximation does not yield a precise enough result. As such only the Fourier transform method will be used to model the pulse propagation.

9.2.2 The atomic medium

In general, a region between two absorptive resonances will have a positive group index. Therefore, when the pulse bandwidth fits between two resonances, some light will be transmitted and the pulse will be slowed. This is true for micro-second long pulses with MHz transparencies [196] or even pico-second pulses with the carrier frequency tuned between the rubidium D_1 and D_2 lines [202] (a 7 THz transparency). Fast-light, where the peak

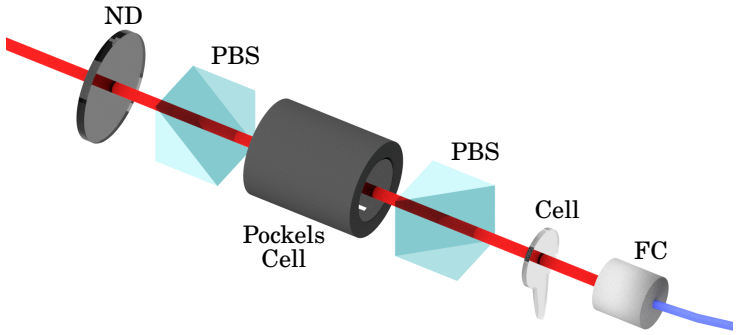

Figure 9.3: Illustration of the pulse propagation apparatus. ND – Neutral density filter, PBS – Polarizing beam splitter, FC – Fibre coupler.

of the pulse arrives before the peak of the reference pulse, is generally seen directly on resonance with an absorptive feature [151].

To demonstrate slow-light pulse propagation we need to look for a frequency range with a large value of n_g across the pulse bandwidth. Figure 9.2 shows that this can be achieved using a 2 mm rubidium vapour cell (at natural abundance) heated to around 180°C. The frequency region between the two Doppler broadened ^{85}Rb transitions gives a group index of $\sim 10^3$ while allowing some light to be transmitted.

9.3 Experiment

Figure 9.3 shows an illustration of the apparatus used for the experiment. Pulses were generated in the same manner as described in section 4.4, with the addition of a neutral density filter (ND) to weaken the pulses. The pulses were then incident on a 2 mm long rubidium (natural abundance) vapour cell, of the kind shown in section 4.1.2. After traversing the cell, the pulse was sent down an optical fibre to a single-photon counting module (SPCM). The signal from the SPCM is detected with an oscilloscope with a bandwidth of 2.5 GHz and 40×10^9 samples a second. A histogram is then built up of photon arrival times over many repetitions.

The pulses typically have 1 ns widths, whereas the SPCM has a 32 ns dead time. This means that, in order to avoid skewing the measurements, the pulses were weak enough so as to cause the SPCM to output less than one

in ten times on average (see appendix A). Taking into account the quantum efficiency of the SPCM and the losses caused by the optics after the cell, we can estimate that the incident pulses contained ~ 1 photon per pulse on average.

To measure the required transmission and refractive index spectra, a weak continuous laser beam was sent through the medium and the transmission of the beam was measured as a function of laser frequency (see inset (a) of figure 9.4). ElecSus was then used to fit this spectrum to find the two temperatures that parameterize number density and the Doppler broadening. These were found to be 179.4 °C and 189.6 °C respectively, which may indicate asymmetric heating of the cell. ElecSus can then be used again to infer what the refractive index of the medium should be given these parameters. Also, this measurement was done before and after the pulse propagation experiment in order to check that the temperature of the vapour does not change significantly during the photon counting.

9.3.1 Laser-frequency stabilization

To measure the pulse profile accurately enough, counting was done over ~ 15 minutes for approximately 100k repetitions. Over this length of time the laser frequency needs to be actively stabilized in order to prevent the carrier frequency of the pulse from drifting. We again use an S_1 signal in a separate 75 mm long vapour cell, a technique similar to that described in section 8.5.3 and ref. [44]. The experimental parameters required to give suitable frequency references were found using ElecSus. We found that tuning the temperature to around ~ 140 °C and magnetic field to around 200 G, gave zero crossings both far off-resonance and near zero detuning for the 75 mm long rubidium vapour cell. This is useful since a carrier detuning near zero can be used to demonstrate slow light while a far off-resonance carrier gives a good approximation to the shape of the reference pulse (defined as a pulse that traversed vacuum instead of the atomic medium). Inset (b) of figure 9.4 shows the raw photodetector signal used as the frequency references. Measuring this signal before and after the experiment ensured that the laser locking points did not vary significantly.

9.4 Results

Figure 9.4 shows the experimentally measured pulse after the medium and the theoretical prediction. When the carrier detuning was locked to (-13.0 ± 0.1) GHz, the shape of the reference pulse is well characterized by a phenomenological multiple-Gaussian fit. However, this off-resonance pulse is not identical to the reference pulse (the pulse as though it had travelled through vacuum). Theoretically, it is predicted that a pulse travelling though the medium at this frequency will be time-delayed by 0.12 ns and be attenuated by a factor of 1.026. Therefore a simple shift and re-scaling is all that is required to recover the reference pulse (the solid black line in figure 9.4).

We can see that the theoretical prediction matches the experimental data within the precision of the experiment; no fit parameters are used. The pulse shows a large time delay which is accurately predicted by the theory. This gives evidence that the refractive index spectrum predicted by ElecSus is accurate.

9.5 Discussion

Excellent agreement between experiment and theory has been seen for slow-light pulse propagation at high optical depths. Not only does this give some evidence that the refractive index spectrum predicted by ElecSus is accurate, but also that our model for the electric susceptibility can be applied to pulses as well as continuous-wave light.

Figure 9.4 shows that it would be desirable for future versions of the ElecSus program to contain a pulse propagation feature. It again shows that the medium can be accurately probed at GHz bandwidth [194]. As such, fitting to short pulses should allow further improvements to accuracy and facilitate observation of dynamics on short time-scales [203].

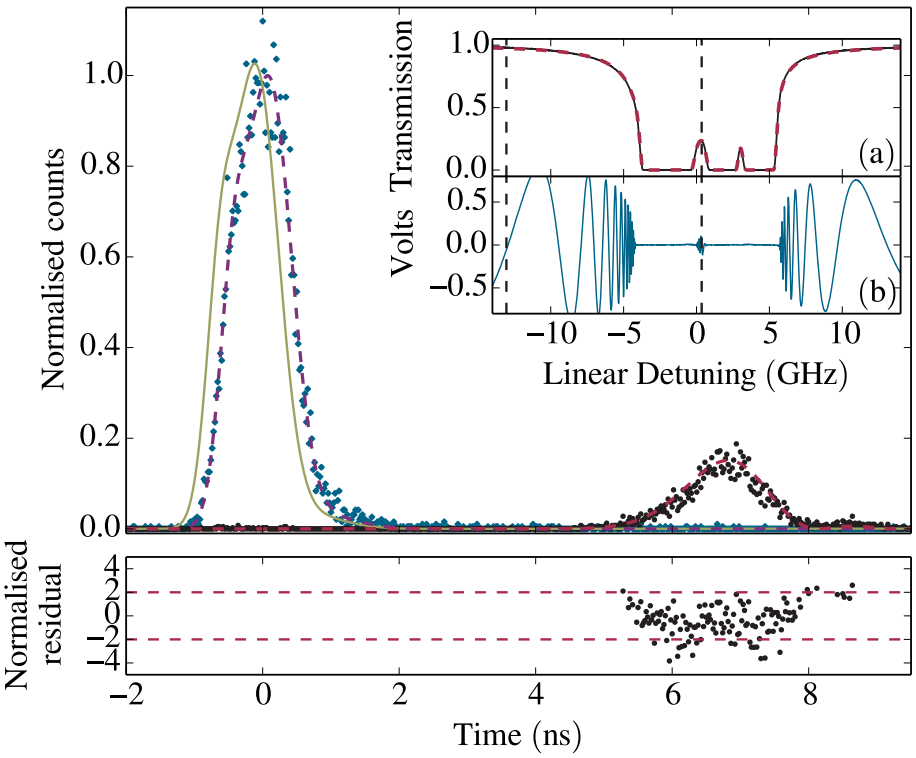

Figure 9.4: Slowlight pulse propagation through a 2 mm long rubidium vapour at natural abundance on the D_1 line (795 nm). The black dots and blue diamonds show the number of photons counted as a function of time (20 ps bin width) for a laser pulse with a carrier detuning near and far from resonance respectively. The counting was completed after approximately 100 k repetitions. The purple dashed line shows a multiple-Gaussian fit used to characterize the shape of the reference pulse. The off-resonance pulse is still subject to a small amounts of time delay and attenuation. The solid-olive curve shows the reference pulse after this is taken into account. The red dashed line shows the theoretical prediction of pulse intensity measured after the cell. The data are normalized to the peak intensity of the reference pulse, while the time axis is centred at this peak. Underneath the graph, the normalized residuals [118] are plotted, which show good agreement (bins with less than 5 counts were omitted since they have been judged statistically insignificant [118]). Inset (a) shows a theoretical fit to a CW experimental transmission scan, performed immediately after the pulse experiment in order to extract the number density temperature and Doppler temperature of the medium. These are taken to be 179.4 °C and 189.6 °C respectively. Inset (b) shows a Faraday signal from a 75 mm long cell used to stabilize the frequency of the laser [44] during the experiment. The black vertical dashed lines show the locking points used to stabilize the carrier detuning to (354 ± 2) MHz, and to (-13.0 ± 0.1) GHz when measuring the reference pulse.

Chapter 10

Conclusions and outlook

10.1 Conclusions

Here we summarize the work presented in this thesis. Part I of the thesis was concerned with the theoretical model of atom-light interaction and its computational implementation. Chapter 1 motivated the work in this thesis and introduced the concept of using alkali-metal vapours as the basis of optical devices. Chapter 2 introduced the theoretical model used to describe the atom-light interaction. The model has previously been shown to be very accurate, however the inclusion of the nuclear interaction with the magnetic field increases this accuracy (essential for the improved accuracy shown in the experiment of chapter 5).

Described in chapter 3 is the computational implementation of the model, which can calculate spectra for all commonly used alkali metals (with the exception of lithium). The implementation is efficient which results in fast computation. The speed of the program makes the problem of computer optimization (whether it be fitting to theory or optimizing some figure of merit) much more practical. Fitting routines are supplied with the program to allow the user to fit experimental atomic spectra to theory. It was shown that fitting to a local minimum can be a problem, therefore two of the three fitting routines supplied are global routines which make it far more likely to find the best fit.

Part II of this thesis looked into applying the computer program to solve

a variety of experimental problems. Chapter 4 described the experimental techniques and apparatus used for the studies in the following chapters. The types of vapour cells, their heaters and the application of magnetic field using permanent magnets were described. Also described was the technique used to calibrate the laser frequency as well as the method used to generate nano-second pulses from continuous light.

In Chapter 5 a new regime for the Faraday effect was introduced. Neither described by the resonant, nor off-resonant, Faraday effect, we call the effect the 'hyperfine Paschen-Back Faraday effect'. This regime of the Faraday effect in a high magnetic field is essentially characterized by the fact that only one hand of light shows dispersion, while the other simply travels through the medium at the vacuum speed c. This has 3 potential uses. One is that the S_1 Faraday rotation spectra closely resemble the refractive index of the medium. The second is that fitting the spectra at these large magnetic fields gives a fractional sensitivity at the 10^{-4} level. Finally, the S_1 spectra have very temperature stable frequency references that could be used as far off-resonance laser frequency error signals.

In Chapter 6 the technique of Faraday filtering was described. We used computer optimization to design the best working conditions of Faraday filters. We see how the two characteristic types of Faraday filter (wing and line-centre) are typically global and local minima respectively (when there is freedom in the signal frequency). The tool of computer optimization was used to explain how line broadening affects the performance of Faraday filters. In particular inhomogeneous broadening was seen to affect the Filter performance drastically for short cell lengths. Also, inhomogeneous broadening affects wing-type filters much more than line-centre filters. This result is of particular importance for the design of compact Faraday filters, where dense vapours are necessary but are subject to unavoidable homogeneous 'self' broadening.

Chapter 7 again employed the technique of computer optimization. It was found the caesium D_1 line performs best for a key figure of merit. Experimentally, the caesium D_1 filter was realized, and achieved a performance that surpasses any other Faraday filter demonstrated to date. This filter could be incorporated into quantum optics experiments that utilize the Cs D_1 line.

The concept of using a Faraday filter in a laser cavity is introduced in chapter 8. A diode laser system using a rubidium Faraday filter as an intra cavity element was experimentally demonstrated. The ElecSus program was again employed in order to find the optimal filter parameters. This 'Faraday-filter laser', to the best of our knowledge, is the first to be made where the cavity free-spectral range is greater than the filter width. This means that the laser frequency does not mode hop within the filter profile, and should in principle be robust to vibrations, temperature changes or current fluctuations.

Finally in chapter 9 we demonstrated a slow-light pulse propagation experiment. Nano-second pulses were detected with single-photon counting modules to test the theoretical prediction. The agreement between experiment and theory is excellent, showing that we can use the absorptive and dispersive properties calculated by ElecSus to accurately model weak-probe pulse propagation. This shows that the optical devices that can be designed using the ElecSus program need not just be continuous-wave, and in principle can be for arbitrary modulations also.

10.2 Outlook

On the theoretical side, the model used was partially in the completely-uncoupled basis. That is to say the matrices were large enough to represent the uncoupled states but the usage of hyperfine coefficients was valid only for the LS-coupled states. When magnetic fields get larger, we expect mixing between the D lines to occur and hence our usage of hyperfine coefficients that are attributed to either D line becomes invalid. This is primarily the reason for the omission of lithium in the ElecSus program. Therefore a model which is based entirely in the completely-uncoupled basis [204] is desirable. For the heavier alkali-metal atoms, this generalization of the model will be advantageous for studies involving the higher lying states. This is because these states (for example the D-states) mix for achievable magnetic fields. This opens up the possibility of studying the Paschen-Back effect, and maybe also the diamagnetic term in the Zeeman interaction [83].

Another extension to the model would be to allow varying populations in

the ground manifold in line with Boltzmann statistics. We assumed that the population of the Zeeman sub-levels in the ground manifold was uniform due to their small separation. In section 2.3.2 we used the fact that the Boltzmann factor was close to unity to justify this. However, using a modified version of the ElecSus program that takes the varying populations of the ground manifold into account, we find that a noticeable difference in the spectra is seen for magnetic fields of just a few tens of kG. This begs the question, can we use the modification of spectra by Boltzmann statistics as a way to perform precise measurements of Boltzmann's constant? Currently there is interest in providing accurate and precise measurements of Boltzmann's constant that can compliment acoustic gas thermometry [205]. One method is to use Doppler broadening of spectral lines [101, 102, 206]. It remains to be seen if measuring the population variation, as predicted by Boltzmann statistics, in hot alkali-metal vapours is feasible as a method to measure Boltzmann's constant.

On the experimental side, we used spectroscopy of a small vapour cell we managed to measure magnetic fields precisely by fitting. We achieve a standard error of 2 G for magnetic fields of ~ 5.5 kG. Further investigation is needed to see if the precision can be further improved. One might expect that using a non-linear signal may improve the precision [207].

Work is ongoing on using the Faraday filter as an internal frequency reference for a Faraday-filter laser. The long term drift needs to be under ~ 1 MHz for the laser to be convenient for atomic physics experiments (such as laser cooling). It is hoped that with these new improvements a 'turnkey' based system can be produced, where the user simply turns on the laser and knows its frequency to an accuracy of 1 MHz or better. This system may also, be cheaper than current systems based on external frequency references, since the control electronics should be simpler. Also a new compact design using a single magnet is under construction. This design shows field variation across the length of the cell, however, theoretical spectra taking this into account seem to indicate that this will not be a problem.

We have seen that by having a model for atomic spectra, and a fast computational implementation, many practical atomic devices can be designed and many experimental problems solved. With our program now publicly

available, there should be no end to the solutions it will provide.

Appendix A

Simulating pulse profiles from photon counting

In this work a single-photon counting module (SPCM) was used to measure the shape of pulses. This was done by building a histogram over time over many repetitions. The shape of the initial pulse (especially its width) critically affects the result of the pulse propagation through the medium. Therefore it is important that we measure the pulse profile accurately. However, two important questions need to be addressed before we can consider the histograms as good representations of the pulses. The first concerns the arrival times of the pulses; if the pulses arrive at different times and/or have different heights, will the histogram be broadened or somehow deformed? It has been observed that pulses can arrive as far apart as 0.3 ns, which is a significant fraction of the pulse width. Therefore one could imagine that the histograms measured are just the result of much shorter pulses arriving at various times. The second question regards the relatively large dead time ($\times$30 pulse widths) of the SPCM; Does the dead time skew the histogram towards earlier times? If the SPCM outputs at the front edge of the pulse, due to the large dead time, there is no chance for it to output again until the next pulse arrives. Therefore we might expect this to significantly skew the data. In this appendix we answer these two questions and confirm that the histograms generated are good representations of the pulse profile.

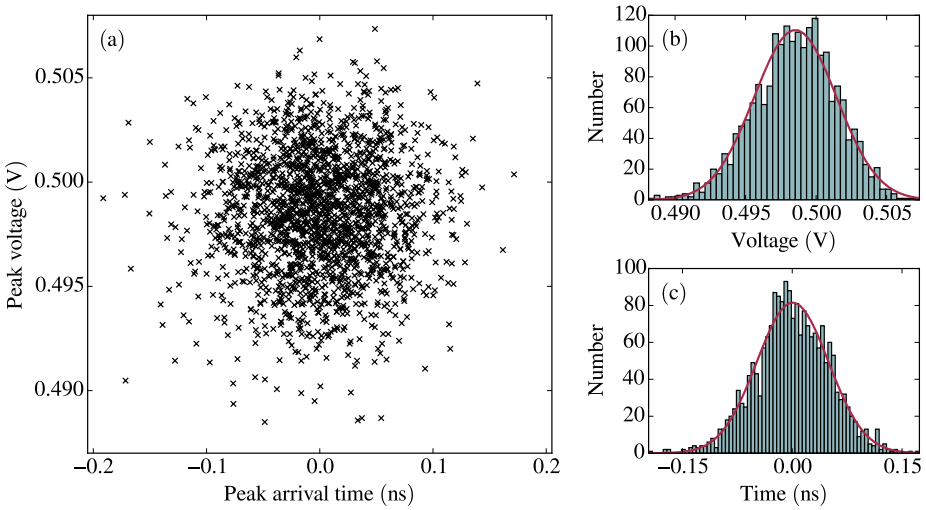

Figure A.1: Pulse peak voltages and arrival times as measured by an FPD. Panel (a) shows the raw data from 2011 repetitions, while panels (b) and (c) show histograms of the voltages and arrival times respectively. The red curves on the histograms are Gaussian curves with the same mean and standard deviation of the data. The voltage mean was found to be 0.498528(14) V while its standard deviation was 2.9 mV. The arrival time mean was 0.0(1.1) ps with a standard deviation of 0.050 ns. The oscilloscope trigger occurs at −150.218 ns.

A.1 Pulse jitter

The pulse propagation experiment utilizes a Pockels cell to create pulses (see section 4.4 for details of the apparatus used to generate pulses). The voltage to the Pockels cell and the trigger to the oscilloscope both come from the same pulse generator, but from different channels. A small variation in the oscilloscope trigger time will make the pulse arrival time (as defined from the oscilloscope trigger) vary. Also any variation in the peak voltage sent to the Pockels cell may change the peak pulse intensity.

To quantify this pulse 'jitter', a method to measure the pulse arrival times and relative intensities for each shot is required, rather than building up a histogram. This can be done by using a fast photo-detector (FPD). The FPD used in this study had a 30 kHz to 1.2 GHz bandwidth. It was found that when using the FPD the pulse shape was not very accurately represented. This was likely due to the limited bandwidth of the detector. However, since we are interested in the spread of arrival times and intensities rather than

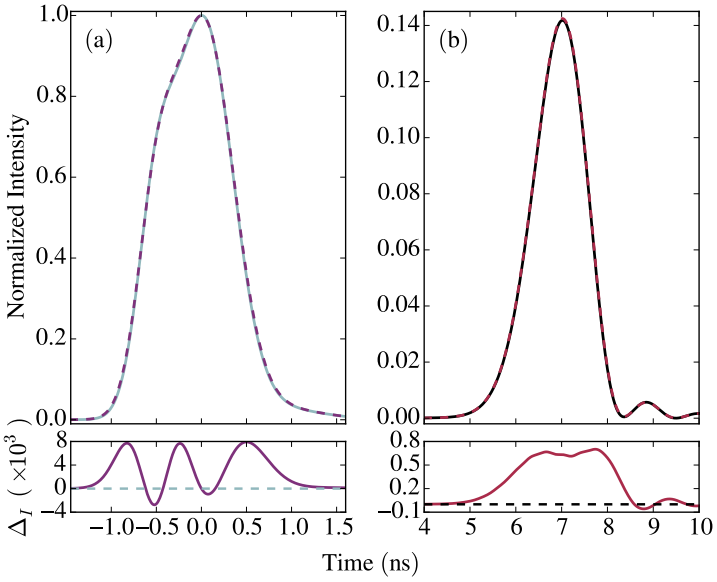

Figure A.2: The solid blue curve in panel (a) is the original reference pulse profile, and the dashed purple curve is the result of adding many copies of the original profile with the different arrival times and peak heights given in figure A.1. The curves are normalized such that the peak value is one. The solid black curve in panel (b) shows the theoretical result after the original pulse profile propagates through the atomic medium (with the same properties as given in the caption of figure 9.4). The dashed red curve is the result of adding the pulses which result from propagating each of the shifted and scaled original reference pulses. This dashed red curve is then normalized using the same factor used to normalize the dashed purple curve in panel (a). Beneath each panel is plotted the difference (Δ_I) between the two curves.

absolute values, we can simply take the peak of the FPD measured pulses as reference points.

Figure A.1 shows the measured peak voltages and arrival times. We can see that over 2011 repetitions the range of peak arrival times was roughly 0.3 ns, while the range of peak intensities was roughly 3% of the mean. To simulate the effect these variations will have on the measured histogram we used the following procedure. First a pulse profile was assumed. Then we assigned a time shift and scaling that corresponds to each of the measured arrival times and peak intensities. The resulting pulses are summed together and then normalized. Figure A.2 shows the resulting pulse shape along with the originally assumed pulse shape. We can see that the difference between the

two pulse shapes is very small (less than 1 %). This effect is far too small to be observed with the precision of our experiment. Therefore, it can safely be ignored.

A.2 The effect of skewed histograms from SPCM dead time

Our measured pulse profiles are built up as histograms of counts from the SPCM over many repetitions. It should be expected that the SPCM is more likely to output at earlier times under the pulse profile than at later times (even for a symmetric pulse profile). This is because of the fact that if the SPCM outputs, it cannot output again until the next pulse arrives, due to the large dead time. For a more intense pulse we may expect that this skew to earlier times will be more pronounced, because we expect the likelihood of the SPCM to output in any given time bin to increase with increasing pulse intensity. In the experiment we do not directly measure the pulse intensity profile, however we have information about the average number of times the SPCM has outputted per repetition. Therefore, we need to know how small the number of counts per repetition should be in order for the measured histograms to accurately represent the pulse intensity profile.

We can directly simulate this by using a 'Monte-Carlo' method [208], which is described as follows.

- Firstly, the time axis (t) was taken to range from -5 to 5 (arb. units) with a grid spacing of 0.05.
- For each time bin there was assigned a value representing the probability (P) of a photon being counted in this time. This probability curve was given a Gaussian profile, $P(t) = A\exp(-t^2)$, where A is an amplitude factor which represents the pulse intensity.
- A random number (R) between 0 and 1 was generated for each time bin. The earliest time bin for which $R < P$ had a 'count' added to it (if there were any at all).

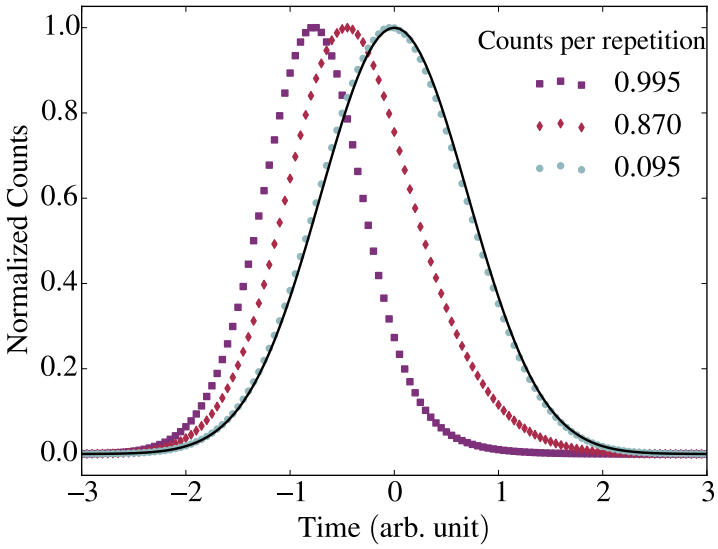

Figure A.3: Normalized counts as a function of time resulting from a Monte-Carlo method of simulating photon counting of pulses (described in the text). We can see that when there are less than 0.1 counts per repetition the counted profile is not significantly skewed to earlier times

- The last step was repeated 800 million times to build up a histogram with good precision.

This algorithm was implemented for three values of A, with higher values giving more counts per repetition, as expected. The resulting histograms are shown in figure A.3. We can see that when the number of counts per repetition is ~ 0.1 or lower the histograms will not be significantly skewed to earlier times.

Appendix B

Physical constants used by the ElecSus program

B.1 Vapour pressure equations and isotopic abundances

Here we list the vapour pressure equations that are used to find the atomic number density as a function of temperature, T. The equations for all four elements are of the form

$$\log_{10}(p[\text{atm}]) = A + B(T[\text{K}])^{-1} + C\log_{10}(T[\text{K}]), \tag{B.1}$$

where p is the vapour pressure, values in square brackets denote the units of the corresponding variables and A, B and C are constants specific to the element and its phase (solid or liquid). Table B.1 shows the values of the constants used for the ElecSus program. All the constants were taken from the "precise" values given in [6]. The atomic number density can then be found from the pressure by assuming an ideal gas,

$$\mathcal{N} = \frac{p}{k_{\text{B}}T}. \tag{B.2}$$

The conversion factor for atmospheres to pascals (1 atm = 101325 Pa) is also used in order to get the number density in units of atoms/m^3. It should

Element (phase)	A	B	C
Na (solid)	5.298	−5603	
Na (liquid)	8.400	−5634	−1.1748
K (solid)	4.961	−4646	
K (liquid)	8.233	−4693	−1.2403
Rb (solid)	4.857	−4215	
Rb (liquid)	8.316	−4275	−1.3102
Cs (solid)	4.711	−3999	
Cs (liquid)	8.232	−4062	−1.3359

Table B.1: Values of the constants used in eq B.1 to determine the vapour pressure. Values are taken from [6].

be noted these equations will give the elemental atomic number density and so they need to be reduced by the appropriate factor when considering one isotope of the element. For example the number density of ^{87}Rb in a naturally abundant vapour will be given by the Rb elemental number density multiplied by 0.2783. Table B.2 shows the natural isotopic abundances.

Element	Mass number	Abundance (%)
Na	23	100
K	39	93.2581
	40	0.0117
	41	6.7302
Rb	85	72.17
	87	27.83
Cs	133	100

Table B.2: Natural abundances of sodium, potassium, rubidium and caesium. Taken from [163].

B.2 Physical constants

This section lists the values of the physical constants used by ElecSus. Note that there has been no attempt to reduce floating point rounding error in calculations. References denote either where the constants have been found

Quantity	Symbol	Value
Electron spin g-factor	g_S	2.00231930436153(53)
Bohr magneton	μ_B	$9.27400968(20) \times 10^{-24}$ J·T^{-1}
Boltzmann constant	k_B	$1.3806488(13) \times 10^{-23}$ J·K^{-1}
Atomic mass unit	u	$1.660538921(73) \times 10^{-27}$ kg
Vacuum permittivity	ϵ_0	$8.854187817620389 \times 10^{-12}$ F·m^{-1}
Bohr radius	a_0	$5.2917721092(17) \times 10^{-11}$ m
Reduced Planck constant	$\hbar$	$1.054571726(47) \times 10^{-34}$ J·s
Speed of light	c	299792458 m·s^{-1}
Elementary charge	e	$1.602176565(35) \times 10^{-19}$ C

Table B.3: Fundamental constants which are loaded from SciPy v0.13.2 library [209], which in turn come from the 2010 CODATA recommended values [210]. Updating SciPy may automatically update these physical constants for ElecSus.

explicitly or for where numbers were found in order to calculate the given constant. The user can change these numbers by changing the entries in the `FundamentalConstants.py` and `AtomConstants.py` files. Isotope shifts are given relative to the linecentre values; negative isotope shifts denote an increase in the hyperfine-free transition frequency. Uncertainties in the values are only given for completeness and do not feature in the code.

Element	Quantity	Symbol	Value	Reference
Na	Linecentre wavelength	λ_0	589.7558147(15) nm	[211]
	Linecentre frequency	ν_0	508.3331958(13) THz	[211]
	Natural linewidth (FWHM)	Γ_0	$2\pi \times 9.765(13)$ MHz	[212]
K	Linecentre wavelength	λ_0	770.10836827(12) nm	[165]
	Linecentre frequency	ν_0	389.286067199(63) THz	[165]
	Natural linewidth (FWHM)	Γ_0	$2\pi \times 5.956(11)$ MHz	[213]
Rb	Linecentre wavelength	λ_0	794.978969380(82) nm	[214]
	Linecentre frequency	ν_0	377.107407299(39) THz	[214]
	Natural linewidth (FWHM)	Γ_0	$2\pi \times 5.746(8)$ MHz	[215]
Cs	Linecentre wavelength	λ_0	894.59295986(11) nm	[178]
	Linecentre frequency	ν_0	335.116048807(41) THz	[178]
	Natural linewidth (FWHM)	Γ_0	$2\pi \times 4.584(8)$ MHz	[216]

Table B.4: Constants related to the D_1 line. The linecentre refers to the definition of zero global detuning.

Element	Quantity	Symbol	Value	Reference
Na	Linecentre wavelength	λ_0	589.1583264(15) nm	[211]
	Linecentre frequency	ν_0	508.8487162(13) THz	[211]
	Natural linewidth (FWHM)	Γ_0	$2\pi \times 9.792(13)$ MHz	[212]
K	Linecentre wavelength	λ_0	766.70090511(24) nm	[165]
	Linecentre frequency	ν_0	391.01617854(12) THz	[165]
	Natural linewidth (FWHM)	Γ_0	$2\pi \times 6.035(11)$ MHz	[213]
Rb	Linecentre wavelength	λ_0	780.24132411(2) nm	[144, 164]
	Linecentre frequency	ν_0	384.23042812(1) THz	[144, 164]
	Natural linewidth (FWHM)	Γ_0	$2\pi \times 6.065(9)$ MHz	[215]
Cs	Linecentre wavelength	λ_0	852.34727582(27) nm	[217]
	Linecentre frequency	ν_0	351.72571850(11) THz	[217]
	Natural linewidth (FWHM)	Γ_0	$2\pi \times 5.225(7)$ MHz	[218]

Table B.5: Constants related to the D_2 line. The linecentre refers to the definition of zero global detuning.

Quantity	Symbol	Value	Reference
Nuclear spin	I	3/2	
Nuclear spin g-factor	g_I'	$-0.0008046108(8)$	[219]
Magnetic dipole constant for $5^2S_{1/2}$	$A_{\rm hf}$	885.8130644(5) MHz·h	[219]
Magnetic dipole constant for $5^2P_{1/2}$	$A_{\rm hf}$	94.44(13) MHz·h	[220]
Magnetic dipole constant for $5^2P_{3/2}$	$A_{\rm hf}$	18.534(15) MHz·h	[221]
Electric quadrupole constant for $5^2P_{3/2}$	$B_{\rm hf}$	2.724(30) MHz·h	[221]
Mass	m	22.9897692807(28) u	[222]

Table B.6: Constants related to the ^{23}Na atom.

Quantity	Symbol	Value	Reference
Nuclear spin	I	3/2	
Nuclear spin g-factor	g_I'	−0.00014193489(12)	[219]
Magnetic dipole constant for $5^2S_{1/2}$	A_{hf}	230.8598601(3) MHz·h	[219]
Magnetic dipole constant for $5^2P_{1/2}$	A_{hf}	27.775(42) MHz·h	[165]
Magnetic dipole constant for $5^2P_{3/2}$	A_{hf}	6.093(25) MHz·h	[165]
Electric quadrupole constant for $5^2P_{3/2}$	B_{hf}	2.786(71) MHz·h	[165]
Isotope shift (D_1)	E_{iso}	8.483 MHz·h	[165]
Isotope shift (D_2)	E_{iso}	8.51 MHz·h	[165]
Mass	m	38.96370668(20) u	[223]

Table B.7: Constants related to the ^{39}K atom.

Quantity	Symbol	Value	Reference
Nuclear spin	I	4	
Nuclear spin g-factor	g_I'	0.000176490(34)	[219]
Magnetic dipole constant for $5^2S_{1/2}$	A_{hf}	−285.7308(24) MHz·h	[219]
Magnetic dipole constant for $5^2P_{1/2}$	A_{hf}	−34.523(25) MHz·h	[165]
Magnetic dipole constant for $5^2P_{3/2}$	A_{hf}	−7.585(10) MHz·h	[165]
Electric quadrupole constant for $5^2P_{3/2}$	B_{hf}	−3.445(90) MHz·h	[165]
Isotope shift (D_1)	E_{iso}	−117.154 MHz·h	[165]
Isotope shift (D_2)	E_{iso}	−117.51 MHz·h	[165]
Mass	m	39.96399848(21) u	[223]

Table B.8: Constants related to the ^{40}K atom.

Quantity	Symbol	Value	Reference
Nuclear spin	I	3/2	
Nuclear spin g-factor	g_I'	−0.00007790600(8)	[219]
Magnetic dipole constant for $5^2S_{1/2}$	A_{hf}	127.0069352(6) MHz·h	[219]
Magnetic dipole constant for $5^2P_{1/2}$	A_{hf}	15.245(42) MHz·h	[165]
Magnetic dipole constant for $5^2P_{3/2}$	A_{hf}	3.363(25) MHz·h	[165]
Electric quadrupole constant for $5^2P_{3/2}$	B_{hf}	3.351(71) MHz·h	[165]
Isotope shift (D_1)	E_{iso}	−227.006 MHz·h	[165]
Isotope shift (D_2)	E_{iso}	−227.67 MHz·h	[165]
Mass	m	40.96182576(21) u	[223]

Table B.9: Constants related to the ^{41}K atom.

Quantity	Symbol	Value	Reference
Nuclear spin	I	5/2	
Nuclear spin g-factor	g_I'	−0.0002936400(6)	[219]
Magnetic dipole constant for $5^2S_{1/2}$	A_{hf}	1011.910813(2) MHz·h	[219]
Magnetic dipole constant for $5^2P_{1/2}$	A_{hf}	120.640(20) MHz·h	[214]
Magnetic dipole constant for $5^2P_{3/2}$	A_{hf}	25.038(5) MHz·h	[224]
Electric quadrupole constant for $5^2P_{3/2}$	B_{hf}	26.011(22) MHz·h	[224]
Isotope shift (D_1)	E_{iso}	21.624 MHz·h	[214]
Isotope shift (D_2)	E_{iso}	21.734 MHz·h	[144]
Mass	m	84.911789732(14) u	[222]

Table B.10: Constants related to the ^{85}Rb atom.

Quantity	Symbol	Value	Reference
Nuclear spin	I	3/2	
Nuclear spin g-factor	g'_I	-0.0009951414(10)	[219]
Magnetic dipole constant for $5^2S_{1/2}$	A_{hf}	3417.34130545215(5) MHz·h	[225]
Magnetic dipole constant for $5^2P_{1/2}$	A_{hf}	406.147(15) MHz·h	[214]
Magnetic dipole constant for $5^2P_{3/2}$	A_{hf}	84.7185(20) MHz·h	[164]
Electric quadrupole constant for $5^2P_{3/2}$	B_{hf}	12.4965(37) MHz·h	[164]
Isotope shift (D_1)	E_{iso}	-56.077 MHz·h	[214]
Isotope shift (D_2)	E_{iso}	-56.361 MHz·h	[144]
Mass	m	86.909180520(15) u	[222]

Table B.11: Constants related to the ^{87}Rb atom.

Quantity	Symbol	Value	Reference
Nuclear spin	I	7/2	
Nuclear spin g-factor	g'_I	−0.00039885395(52)	[219]
Magnetic dipole constant for $5^2S_{1/2}$	A_{hf}	2298.1579425 MHz·h (exact)	[219]
Magnetic dipole constant for $5^2P_{1/2}$	A_{hf}	291.922(20) MHz·h	[217]
Magnetic dipole constant for $5^2P_{3/2}$	A_{hf}	50.28827(23) MHz·h	[95]
Electric quadrupole constant for $5^2P_{3/2}$	B_{hf}	−0.4934(17) MHz·h	[95]
Mass	m	132.905451933(24) u	[223]

Table B.12: Constants related to the ^{133}Cs atom.

Bibliography

[1] P. Gill, *When should we change the definition of the second?*, Phil. Trans. R. Soc. A **369**, 4109 (2011). 1

[2] J. Kitching, S. Knappe, and E. A. Donley, *Atomic sensors - A review*, IEEE Sensors. J. **11**, 1749 (2011). 1

[3] M. H. Anderson, J. R. Ensher, M. R. Matthews, C. E. Wieman, and E. A. Cornell, *Observation of bose-einstein condensation in a dilute atomic vapor*, Science **269**, 198 (1995). 1

[4] D. Barredo *et al.*, *Coherent Excitation Transfer in a Spin Chain of Three Rydberg Atoms*, Phys. Rev. Lett. **114**, 113002 (2014). 1

[5] C. S. Adams, H. J. Lee, N. Davidson, M. Kasevich, and S. Chu, *Evaporative cooling in a crossed dipole trap*, Phys. Rev. Lett. **74**, 3577 (1995). 1

[6] C. B. Alcock, V. P. Itkin, and M. K. Horrigan, *Vapour Pressure Equations for the Metallic Elements: 298–2500K*, Can. Metall. Q. **23**, 309 (1984). 2, 47, 73, 76, 79, 82, 97, 133, 134

[7] C. S. Adams and E. Riis, *Laser cooling and trapping of neutral atoms*, Prog. Quantum Electron. **21**, 1 (1997). 2

[8] H. Kübler, J. Shaffer, T. Baluktsian, R. Löw, and T. Pfau, *Coherent excitation of Rydberg atoms in micrometre-sized atomic vapour cells*, Nat. Photonics **4**, 112 (2010). 2

[9] R. Friedberg, S. Hartmann, and J. Manassah, *Frequency shifts in emission and absorption by resonant systems ot two-level atoms*, Phys. Rep. **7**, 101 (1973). 2

[10] J. Keaveney *et al.*, *Cooperative Lamb Shift in an Atomic Vapor Layer of Nanometer Thickness*, Phys. Rev. Lett. **108**, 173601 (2012). 2, 3, 51, 69

[11] J. Keaveney *et al.*, *Optical transmission through a dipolar layer*, (2011), arXiv:1109.3669. 2

[12] L. Weller *et al.*, *Cooperative Enhancement of Energy Transfer in a High-Density Thermal Vapor*, (2013), arXiv:1308.0129. 2, 10

[13] E. Vliegen *et al.*, *Faraday rotation density measurements of optically thick alkali metal vapors*, Nucl. Instrum. Meth. A **460**, 444 (2001). 2, 32

[14] H. van Kampen, V. Sautenkov, A. Shalagin, E. Eliel, and J. Woerdman, *Dipole-dipole collision-induced transport of resonance excitation in a high-density atomic vapor*, Phys. Rev. A **56**, 3569 (1997). 3

[15] J. Keaveney, A. Sargsyan, D. Sarkisyan, A. Papoyan, and C. S. Adams, *Active narrowband filtering, line narrowing and gain using ladder electromagnetically induced transparency in an optically thick atomic vapour*, J. Phys. B: At. Mol. Opt. Phys. **47**, 075002 (2014). 3

[16] M. Mescher, R. Lutwak, and M. Varghese, *An ultra-low-power physics package for a chip-scale atomic clock*, in *13th International Conference on Solid-State Sensors, Actuators and Microsystems, Digest of Technical Papers. TRANSDUCERS '05.*, volume 1, pp. 311–316, 2005. 3, 77, 81

[17] J. F. DeNatale *et al.*, *Compact, low-power chip-scale atomic clock*, in *Position, Location and Navigation Symposium, 2008 IEEE/ION*, pp. 67–70, 2008.

[18] R. Mhaskar, S. Knappe, and J. Kitching, *A low-power, high-sensitivity micromachined optical magnetometer*, Appl. Phys. Lett. **101**, 241105 (2012). 3, 81

[19] D. Sarkisyan, D. Bloch, A. Papoyan, and M. Ducloy, *Sub-Doppler spectroscopy by sub-micron thin Cs vapour layer*, Opt. Commun. **200**, 201 (2001). 3, 51

[20] L. A. Liew *et al.*, *Microfabricated alkali atom vapor cells*, Appl. Phys. Lett. **84**, 2694 (2004).

[21] S. Knappe *et al.*, *Atomic vapor cells for chip-scale atomic clocks with improved long-term frequency stability*, Opt. Lett. **30**, 2351 (2005). 57, 74

[22] J. Su, K. Deng, Z. Wang, and D.-Z. Guo, *Microfabrication of ^{85}Rb vapor cell for chip-scale atomic clocks*, in *Frequency Control Symposium, Joint with the 22nd European Frequency and Time forum. IEEE International*, pp. 1016–1018, 2009. 32

[23] T. Baluktsian *et al.*, *Fabrication method for microscopic vapor cells for alkali atoms*, Opt. Lett. **35**, 1950 (2010).

[24] K. Tsujimoto *et al.*, *On-chip fabrication of alkali-metal vapor cells utilizing an alkali-metal source tablet*, J. Micromech. Microeng. **23**, 115003 (2013). 32

[25] R. Straessle *et al.*, *Microfabricated alkali vapor cell with anti-relaxation wall coating*, Appl. Phys. Lett. **105**, 043502 (2014). 3

[26] L. Weller *et al.*, *Absolute absorption and dispersion of a rubidium vapour in the hyperfine PaschenBack regime*, J. Phys. B: At. Mol. Opt. Phys. **45**, 215005 (2012). 3, 9, 23, 27, 28, 29, 60, 69, 73, 76, 79, 91

[27] R. Höller, F. Renzoni, L. Windholz, and J. H. Xu, *Coherent population trapping on the sodium D_1 line in high magnetic fields*, J. Opt. Soc. Am. B **14**, 2221 (1997). 3

[28] A. Rudolf and T. Walther, *High-transmission excited-state Faraday anomalous dispersion optical filter edge filter based on a Halbach cylinder magnetic-field configuration*, Opt. Lett. **37**, 4477 (2012). 51, 69

[29] L. Weller *et al.*, *Optical isolator using an atomic vapor in the hyperfine Paschen-Back regime*, Opt. Lett. **37**, 3405 (2012). 4, 5, 9, 32, 60, 69, 73, 105

[30] A. Sargsyan *et al.*, *Hyperfine PaschenBack regime in alkali metal atoms: consistency of two theoretical considerations and experiment*, J. Opt. Soc. Am. B **31**, 1046 (2014). 3

[31] L. Windholz, *Zeeman- and Paschen-Back-effect of the hyperfine structure of the sodium D_1-line*, Z. Phys. A Atoms Nucl. **322**, 203 (1985). 3

[32] L. Windholz and M. Musso, *Zeeman- and Paschen-Back-effect of the hyperfine structure of the sodium D_2-line*, Z. Phys. D Atoms, Mol. Clust. **8**, 239 (1988).

[33] A. Sargsyan *et al.*, *Hyperfine Paschen-Back regime realized in Rb nanocell*, Opt. Lett. **37**, 1379 (2012). 27

[34] A. Sargsyan, R. Mirzoyan, and D. Sarkisyan, *Splitting of the electromagnetically induced transparency resonance on ^{85}Rb atoms in strong magnetic fields up to the Paschen-Back regime*, JETP Lett. **96**, 303 (2012).

[35] A. Sargsyan, G. Hakhumyan, R. Mirzoyan, and D. Sarkisyan, *Investigation of atomic transitions of cesium in strong magnetic fields by an optical half-wavelength cell*, JETP Lett. **98**, 441 (2013).

[36] A. Sargsyan *et al.*, *Saturated-absorption spectroscopy revisited: atomic transitions in strong magnetic fields ($> 20\,mT$) with a micrometer-thin cell*, Opt. Lett. **39**, 2270 (2014). 3

[37] C. Umfer, L. Windholz, and M. Musso, *Investigations of the sodium and lithium D-lines in strong magnetic fields*, Z. Phys. D Atoms, Mol. Clust. **25**, 23 (1992). 3

[38] H. Gibbs, *Incoherent Resonance Fluorescence from a Rb Atomic Beam Excited by a Short Coherent Optical Pulse*, Phys. Rev. A **8**, 446 (1973). 3

[39] D. J. Whiting *et al.*, *Electromagnetically induced absorption in a non-degenerate three-level ladder system*, in preparation, 2015. 3, 10

[40] M. Faraday, *Experimental Researches in Electricity. Nineteenth Series*, Phil. Trans. R. Soc. Lond. **136**, 1 (1846). 4

[41] Y. Öhman, *On some new auxiliary instruments in astrophysical research*, Stockholms Obs. Ann. **19**, 3 (1956). 4

[42] A. I. Lvovsky, B. C. Sanders, and W. Tittel, *Optical quantum memory*, Nat. Photonics **3**, 706 (2009). 4

[43] R. Frey and C. Flytzanis, *Optical limitation in resonant Faraday media*, Opt. Lett. **25**, 838 (2000). 4, 95

[44] A. L. Marchant *et al.*, *Off-resonance laser frequency stabilization using the Faraday effect*, Opt. Lett. **36**, 64 (2011). 4, 33, 54, 55, 76, 77, 120, 122

[45] M. A. Zentile *et al.*, *The hyperfine Paschen-Back Faraday effect*, J. Phys. B: At. Mol. Opt. Phys. **47**, 075005 (2014). 4, 9, 46

[46] D. Budker *et al.*, *Resonant nonlinear magneto-optical effects in atoms*, Rev. Mod. Phys. **74**, 1153 (2002). 4, 30, 70, 72

[47] S. L. Kemp, I. G. Hughes, and S. L. Cornish, *An analytical model of off-resonant Faraday rotation in hot alkali metal vapours*, J. Phys. B: At. Mol. Opt. Phys. **44**, 235004 (2011). 4, 30, 70, 71

[48] G. Agnelli, A. Cacciani, and M. Fofi, *The magneto-optical filter*, Sol. Phys. **44**, 509 (1975). 4, 95

[49] A. Cacciani and M. Fofi, *The magneto-optical filter*, Sol. Phys. **59**, 179 (1978). 4

[50] P. P. Sorokin, J. R. Lankard, V. L. Moruzzi, and A. Lurio, *Frequency-locking of organic dye lasers to atomic resonance lines*, Appl. Phys. Lett. **15**, 179 (1969). 4, 95, 101

[51] T. Endo, T. Yabuzaki, M. Kitano, T. Sato, and T. Ogawa, *Frequency-locking of a CW dye laser to the center of the sodium D lines by a Faraday filter*, IEEE J. Quant. Electron. **13**, 866 (1977). 95

[52] T. Endo, T. Yabuzaki, M. Kitano, T. Sato, and T. Ogawa, *Frequency-locking of a CW dye laser to absorption lines of neon by a Faraday filter*, IEEE J. Quant. Electron. **14**, 977 (1978). 4, 95, 101

[53] D. J. Dick and T. M. Shay, *Ultrahigh-noise rejection optical filter*, Opt. Lett. **16**, 867 (1991). 4, 32, 38, 48, 95

[54] J. Menders, K. Benson, S. H. Bloom, C. S. Liu, and E. Korevaar, *Ultranarrow line filtering using a Cs Faraday filter at 852 nm*, Opt. Lett. **16**, 846 (1991). 4, 32, 38, 71, 95

[55] A. Popescu, K. Schorstein, and T. Walther, *A novel approach to a Brillouin-LIDAR for remote sensing of the ocean temperature*, Appl. Phys. B **79**, 955 (2004). 4

[56] H. Chen, M. A. White, D. A. Krueger, and C. Y. She, *Daytime mesopause temperature measurements with a sodium-vapor dispersive Faraday filter in a lidar receiver*, Opt. Lett. **21**, 1093 (1996). 4

[57] C. Fricke-Begemann, M. Alpers, and J. Höffner, *Daylight rejection with a new receiver for potassium resonance temperature lidars*, Opt. Lett. **27**, 1932 (2002). 5, 82

[58] W. Huang *et al.*, *Na double-edge magneto-optic filter for Na lidar profiling of wind and temperature in the lower atmosphere*, Opt. Lett. **34**, 199 (2009).

[59] S. D. Harrell *et al.*, *The Faraday filter-based spectrometer for observing sodium nightglow and studying atomic and molecular oxygen associated with the sodium chemistry in the mesopause region*, J. Atmos. Sol.-Terr. Phys. **72**, 1260 (2010). 4, 85

[60] P. Wanninger, E. C. Valdez, and T. M. Shay, *Diode-laser frequency stabilization based on the resonant Faraday effect*, IEEE Photon. Technol. Lett. **4**, 94 (1992). 4, 101, 102

[61] K. Choi, J. Menders, P. Searcy, and E. Korevaar, *Optical feedback locking of a diode laser using a cesium Faraday filter*, Opt. Commun. **96**, 240 (1993). 102, 104

[62] X. Miao *et al.*, *Note: Demonstration of an external-cavity diode laser system immune to current and temperature fluctuations*, Rev. Sci. Instrum. **82**, 086106 (2011). 4, 101, 102

[63] S. H. Bloom *et al.*, *Long-range, noncoherent laser Doppler velocimeter*, Opt. Lett. **16**, 1794 (1991). 4

[64] S. H. Bloom, P. A. Searcy, K. Choi, R. Kremer, and E. Korevaar, *Helicopter plume detection by using an ultranarrow-band noncoherent laser Doppler velocimeter*, Opt. Lett. **18**, 244 (1993). 4, 95

[65] T. Junxiong *et al.*, *Experimental study of a model digital space optical communication system with new quantum devices*, Appl. Opt. **34**, 2619 (1995). 4

[66] X. Shan, X. Sun, J. Luo, Z. Tan, and M. Zhan, *Free-space quantum key distribution with Rb vapor filters*, Appl. Phys. Lett. **89**, 191121 (2006). 4

[67] R. P. Abel, U. Krohn, P. Siddons, I. G. Hughes, and C. S. Adams, *Faraday dichroic beam splitter for Raman light using an isotopically pure alkali-metal-vapor cell*, Opt. Lett. **34**, 3071 (2009). 4, 32, 38

[68] P. Siyushev, G. Stein, J. Wrachtrup, and I. Gerhardt, *Molecular photons interfaced with alkali atoms*, Nature **509**, 66 (2014). 4

[69] J. A. Zielińska, F. A. Beduini, V. G. Lucivero, and M. W. Mitchell, *Atomic filtering for hybrid continuous-variable/discrete-variable quantum optics*, Opt. Express **22**, 25307 (2014). 4, 95

[70] D. Jalas *et al.*, *What is and what is not an optical isolator*, Nat. Photonics **7**, 579 (2013). 5

[71] P. Yeh, *Dispersive magnetooptic filters*, Appl. Opt. **21**, 2069 (1982). 5

[72] M. A. Zentile *et al.*, *ElecSus: A program to calculate the electric susceptibility of an atomic ensemble*, Comput. Phys. Commun. **189**, 162 (2015). 6, 8, 82, 84, 92, 98, 100, 105, 107

[73] M. A. Zentile, D. J. Whiting, J. Keaveney, C. S. Adams, and I. G. Hughes, *Atomic Faraday filter with equivalent noise bandwidth less than 1 GHz*, Opt. Lett. **40**, 2000 (2015). 8, 82, 85

[74] M. A. Zentile *et al.*, *Effect of line broadening on the performance of atomic Faraday filters*, (2015), arXiv:1504.03651. 8

[75] B. W. Shore and P. L. Knight, *The Jaynes-Cummings Model*, J. Mod. Opt. **40**, 1195 (1993). 12

[76] P. Siddons, *Light propagation through atomic vapours*, J. Phys. B: At. Mol. Opt. Phys. **47**, 093001 (2014). 13

[77] S. Aljunid, *Interaction of a strongly focused light beam with single atoms*, PhD thesis, National University of Singapore, 2012. 13

[78] J. D. Jackson, *Classical Electrodynamics*, 3rd ed. (Wiley, 1999). 13, 14, 15

[79] R. Loudon, *The Quantum Theory of Light*, 3rd ed. (Oxford University Press, Oxford, 2000). 14, 16, 17, 18

[80] J. Keaveney, *Cooperative interactions in dense thermal Rb vapour confined in nm-scale cells*, PhD thesis, Durham, 2013. 15, 21

[81] R. W. Boyd, *Nonlinear Optics*, 2nd ed. (Academic Press, San Diego, 2003). 15

[82] B. H. Bransden and C. J. Joachain, *Quantum Mechanics*, 2nd ed. (Pearson Education Limited, Harlow, 2000). 16

[83] B. H. Bransden and C. J. Joachain, *Physics of Atoms and Molecules*, 2nd ed. (Pearson Education Limited, Harlow, 2003). 16, 21, 23, 25, 26, 125

[84] M. Harris, *Realisation of a cold mixture of rubidium and caesium*, PhD thesis, Durham, 2008. 18

[85] S. R. Shin and H.-R. Noh, *Calculation and Measurement of Absolute Transmission in Rubidium*, J. Phys. Soc. Jpn. **78**, 084302 (2009). 18, 20

[86] T. Jeong, J. Y. Won, and H.-R. Noh, *Line shapes in polarization spectroscopy for the rubidium D_1 line in an external magnetic field*, Opt. Commun. **292**, 106 (2013). 18

[87] D. A. Smith and I. G. Hughes, *The role of hyperfine pumping in multilevel systems exhibiting saturated absorption*, Am. J. Phys. **72**, 631 (2004). 18, 20, 64, 65, 73

[88] B. E. Sherlock and I. G. Hughes, *How weak is a weak probe in laser spectroscopy?*, Am. J. Phys. **77**, 111 (2009). 18, 20, 73

[89] P. Siddons, C. S. Adams, C. Ge, and I. G. Hughes, *Absolute absorption on rubidium D lines: comparison between theory and experiment*, J. Phys. B: At. Mol. Opt. Phys. **41**, 155004 (2008). 19, 69

[90] A. M. Guénault, *Statistical Physics*, 2nd ed. (Springer, Dordrecht, 2007). 19

[91] L. Weller, R. J. Bettles, P. Siddons, C. S. Adams, and I. G. Hughes, *Absolute absorption on the rubidium D_1 line including resonant dipoledipole interactions*, J. Phys. B: At. Mol. Opt. Phys. **44**, 195006 (2011). 20, 69, 81, 83, 97

[92] S. J. Blundell and K. M. Blundell, *Concepts in Thermal Physics* (Oxford University Press, 2009). 20

[93] T. M. Stace, G.-W. Truong, J. Anstie, E. F. May, and A. N. Luiten, *Power-dependent line-shape corrections for quantitative spectroscopy*, Phys. Rev. A **86**, 012506 (2012). 20

[94] R. H. Dicke, *The Effect of Collisions upon the Doppler Width of Spectral Lines*, Phys. Rev. **89**, 472 (1953). 20

[95] V. Gerginov, A. Derevianko, and C. E. Tanner, *Observation of the Nuclear Magnetic Octupole Moment of ^{133}Cs*, Phys. Rev. Lett. **91**, 072501 (2003). 21, 138

[96] A. Corney, *Atomic and Laser Spectroscopy* (Oxford University Press, Oxford, 1977). 23, 25, 27

[97] A. R. Edmonds, *Angular momentum in quantum mechanics*, 2nd ed. (Princeton University Press, Princeton, New Jersey, 1996). 25

[98] H. Chen, C. Y. She, P. Searcy, and E. Korevaar, *Sodium-vapor dispersive Faraday filter*, Opt. Lett. **18**, 1019 (1993). 32, 38, 49, 82, 95

[99] J. A. Zielińska, F. A. Beduini, N. Godbout, and M. W. Mitchell, *Ultranarrow Faraday rotation filter at the Rb D_1 line*, Opt. Lett. **37**, 524 (2012). 32, 38, 82, 95, 99

[100] D. Budker and M. Romalis, *Optical magnetometry*, Nat. Phys. **3**, 227 (2007). 32

[101] G. Casa *et al.*, *Primary Gas Thermometry by Means of Laser-Absorption Spectroscopy: Determination of the Boltzmann Constant*, Phys. Rev. Lett. **100**, 200801 (2008). 32, 33, 126

[102] M. Triki *et al.*, *Speed-dependent effects in NH_3 self-broadened spectra: Towards the determination of the Boltzmann constant*, Phys. Rev. A **85**, 062510 (2012). 126

[103] G.-W. Truong, J. D. Anstie, E. F. May, T. M. Stace, and A. N. Luiten, *Absolute absorption line-shape measurements at the shot-noise limit*, Phys. Rev. A **86**, 030501 (2012). 32, 80

[104] Z. Wu, M. Kitano, W. Happer, M. Hou, and J. Daniels, *Optical determination of alkali metal vapor number density using Faraday rotation*, Appl. Opt. **25**, 4483 (1986). 32

[105] U. D. Rapol, A. Wasan, and V. Natarajan, *Loading of a Rb magneto-optic trap from a getter source*, Phys. Rev. A **64**, 023402 (2001). 32

[106] K. L. Moore *et al.*, *Collimated, single-pass atom source from a pulsed alkali metal dispenser for laser-cooling experiments*, Rev. Sci. Instrum. **76**, 023106 (2005).

[107] D. R. Scherer, D. B. Fenner, and J. M. Hensley, *Characterization of alkali metal dispensers and non-evaporable getter pumps in ultrahigh vacuum systems for cold atomic sensors*, J. Vac. Sci. Technol. A **30**, 061602 (2012). 32

[108] P. Knapkiewicz *et al.*, *MEMS caesium vapour cell for european micro-atomic-clock*, Procedia Eng. **5**, 721 (2010). 32

[109] A. Horsley *et al.*, *Imaging of relaxation times and microwave field strength in a microfabricated vapor cell*, Phys. Rev. A **88**, 063407 (2013). 32

[110] S. B. Morales, E. Pangui, X. Landsheere, H. Tran, and J.-M. Hartmann, *Variable-length cell for studies of gas spectra with extremely short optical paths*, Appl. Opt. **53**, 4117 (2014). 33

[111] B. Schaefer, E. Collett, R. Smyth, D. Barrett, and B. Fraher, *Measuring the Stokes polarization parameters*, Am. J. Phys. **75**, 163 (2007). 33, 71

[112] W. Yuan, W. Shen, Y. Zhang, and X. Liu, *Dielectric multilayer beam splitter with differential phase shift on transmission and reflection for division-of-amplitude photopolarimeter*, Opt. Express **22**, 11011 (2014). 33

[113] A. Millett-Sikking, I. G. Hughes, P. Tierney, and S. L. Cornish, *DAVLL lineshapes in atomic rubidium*, J. Phys. B: At. Mol. Opt. Phys. **40**, 187 (2007). 33

[114] C. Lee *et al.*, *Small-sized dichroic atomic vapor laser lock*, Rev. Sci. Instrum. **82**, 043107 (2011). 33

[115] R. Clark Jones, *A New Calculus for the Treatment of Optical Systems*, J. Opt. Soc. Am. **31**, 488 (1941). 34

[116] E. Hecht, *Optics*, 4th ed. (Addison Wesley, 2002). 34, 36, 66

[117] J. D. Hunter, *Matplotlib: A 2D graphics environment*, Comput. Sci. Eng. **9**, 90 (2007). 39

[118] I. G. Hughes and T. P. A. Hase, *Measurements and their Uncertainties: A Practical Guide to Modern Error Analysis*, 1st ed. (Oxford University Press, 2010). 39, 42, 45, 46, 60, 61, 76, 84, 107, 122

[119] S. G. Johnson, *Faddeeva Package*, http://ab-initio.mit.edu/wiki/index.php/Faddeeva_Package, 2012, Accessed: 2015-02-06. 40

[120] L. Weller, *Absolute Absorption and Dispersion in a Thermal Rb Vapour at High Densities and High Magnetic Fields*, PhD thesis, Durham University, 2013. 41, 59, 64, 74

[121] S. Russell and P. Norvig, *Artificial Intelligence: A Modern Approach*, 2nd ed. (Pearson Education Inc., New Jersey, 2003). 43, 76, 84

[122] S. Kirkpatrick, C. D. Gelatt Jr., and M. P. Vecchi, *Optimization by simulated annealing*, Science **220**, 671 (1983). 44

[123] N. Metropolis, A. W. Rosenbluth, M. N. Rosenbluth, A. H. Teller, and E. Teller, *Equation of State Calculations by Fast Computing Machines*, J. Chem. Phys. **21**, 1087 (1953). 44

[124] M. Lundy and A. Mees, *Convergence of an annealing algorithm*, Math. Program. **34**, 111 (1986). 44

[125] Y. Wang *et al.*, *Cs Faraday optical filter with a single transmission peak resonant with the atomic transition at 455 nm*, Opt. Express **20**, 25817 (2012). 51, 95

[126] P. M. Duarte *et al.*, *All-optical production of a lithium quantum gas using narrow-line laser cooling*, Phys. Rev. A **84**, 061406 (2011). 51

[127] D. C. McKay *et al.*, *Low-temperature high-density magneto-optical trapping of potassium using the open* $4S \rightarrow 5P$ *transition at 405 nm*, Phys. Rev. A **84**, 063420 (2011).

[128] J. Sebastian *et al.*, *Two-stage magneto-optical trapping and narrow-line cooling of* ^{6}*Li atoms to high phase-space density*, Phys. Rev. A **90**, 033417 (2014). 51

[129] R. I. Billmers *et al.*, *Experimental demonstration of an excited-state Faraday filter operating at 532 nm*, Opt. Lett. **20**, 106 (1995). 51, 95

[130] L. Zhang and J. Tang, *Experimental study on optimization of the working conditions of excited state Faraday filter*, Opt. Commun. **152**, 275 (1998). 51

[131] M. Bajcsy *et al.*, *Efficient All-Optical Switching Using Slow Light within a Hollow Fiber*, Phys. Rev. Lett. **102**, 203902 (2009). 51, 114

[132] V. Venkataraman, K. Saha, and A. L. Gaeta, *Phase modulation at the few-photon level for weak-nonlinearity-based quantum computing*, Nat. Photonics **7**, 138 (2013).

[133] C. Perrella *et al.*, *High-efficiency cross-phase modulation in a gas-filled waveguide*, Phys. Rev. A **88**, 013819 (2013).

[134] G. Epple *et al.*, *Rydberg atoms in hollow-core photonic crystal fibres*, Nat. Commun. **5**, 4132 (2014). 81

[135] M. R. Sprague *et al.*, *Broadband single-photon-level memory in a hollow-core photonic crystal fibre*, Nat. Photonics **8**, 287 (2014).

[136] F. Haas, J. Volz, R. Gehr, J. Reichel, and J. Estève, *Entangled states of more than 40 atoms in an optical fiber cavity*, Science **344**, 180 (2014). 51

[137] H. B. G. Casimir and D. Polder, *The Influence of Retardation on the London-van der Waals Forces*, Phys. Rev. **73**, 360 (1948). 51

[138] H. Bender *et al.*, *Probing Atom-Surface Interactions by Diffraction of Bose-Einstein Condensates*, Phys. Rev. X **4**, 011029 (2014).

[139] K. A. Whittaker *et al.*, *Optical Response of Gas-Phase Atoms at Less than $\lambda/80$ from a Dielectric Surface*, Phys. Rev. Lett. **112**, 253201 (2014). 51, 81

[140] D. J. McCarron, I. G. Hughes, P. Tierney, and S. L. Cornish, *A heated vapor cell unit for dichroic atomic vapor laser lock in atomic rubidium*, Rev. Sci. Instrum. **78**, 093106 (2007). 54, 55

[141] H. D. Young and R. A. Freedman, *University Physics*, 13th ed. (Pearson, San Francisco, 2012). 55

[142] D. Bruce Montgomery and J. Terrell, *Some useful information for the design of air-core solenoids*, 1961, Technical report. 56

[143] K. Shiraishi, F. Tajima, and S. Kawakami, *Compact Faraday rotator for an optical isolator using magnets arranged with alternating polarities*, Opt. Lett. **11**, 82 (1986). 59

[144] G. P. Barwood, P. Gill, and W. R. C. Rowley, *Frequency measurements on optically narrowed Rb-stabilised laser diodes at 780 nm and 795 nm*, Appl. Phys. B **53**, 142 (1991). 60, 89, 93, 136, 137, 138

[145] W. Robertson, B. Cazzolato, and A. Zander, *A simplified force equation for coaxial cylindrical magnets and thin coils*, IEEE Trans. Magn. **47**, 2045 (2011). 64

[146] K. B. MacAdam, A. Steinbach, and C. Wieman, *A narrow-band tunable diode laser system with grating feedback, and a saturated absorption spectrometer for Cs and Rb*, Am. J. Phys. **60**, 1098 (1992). 64

[147] L. Weller, T. Dalton, P. Siddons, C. S. Adams, and I. G. Hughes, *Measuring the Stokes parameters for light transmitted by a high-density rubidium vapour in large magnetic fields*, J. Phys. B: At. Mol. Opt. Phys. **45**, 055001 (2012). 69

[148] M. Nawaz, W. A. Farooq, and J.-P. Connerade, *The influence of the Paschen-Back effect on magneto-optical rotation spectra*, J. Phys. B: At. Mol. Opt. Phys. **25**, 3283 (1992). 69

[149] M. Nawaz, W. A. Farooq, and J.-P. Connerade, *Magneto-optical spectra of lithium and sodium*, J. Phys. B: At. Mol. Opt. Phys. **25**, 5327 (1992). 69

[150] G. T. Purves, G. Jundt, C. S. Adams, and I. G. Hughes, *Refractive index measurements by probe-beam deflection*, Eur. Phys. J. D **29**, 433 (2004). 71

[151] J. Keaveney, I. G. Hughes, A. Sargsyan, D. Sarkisyan, and C. S. Adams, *Maximal Refraction and Superluminal Propagation in a Gaseous Nanolayer*, Phys. Rev. Lett. **109**, 233001 (2012). 71, 117, 119

[152] A. Sargsyan *et al.*, *Atomic transitions of Rb, D_2 line in strong magnetic fields: hyperfine Paschen-Back regime*, Opt. Commun. **334**, 208 (2015). 76

[153] A. Sargsyan *et al.*, *Complete hyperfine Paschen-Back regime at relatively small magnetic fields realized in potassium nano-cell*, Europhys. Lett. **110**, 23001 (2015). 76

[154] T. Sebastian, *Temperature effects on torque production and efficiency of PM motors using NdFeB magnets*, IEEE Trans. Ind. Appl. **31**, 353 (1995). 77

[155] J. Larry Pezzaniti and R. A. Chipman, *Angular dependence of polarizing beam-splitter cubes.*, Appl. Opt. **33**, 1916 (1994). 79

[156] E. L. Lewis, *Collisional relaxation of atomic excited states, line broadening and interatomic interactions*, Phys. Rep. **58**, 1 (1980). 81

[157] W. Kiefer, R. Löw, J. Wrachtrup, and I. Gerhardt, *Na-Faraday rotation filtering: The optimal point*, Sci. Rep. **4**, 6552 (2014). 82, 84, 95, 99

[158] B. Yin and T. M. Shay, *Theoretical model for a Faraday anomalous dispersion optical filter*, Opt. Lett. **16**, 1617 (1991). 82

[159] S. D. Harrell *et al.*, *Sodium and potassium vapor Faraday filters revisited: theory and applications*, J. Opt. Soc. Am. B **26**, 659 (2009). 82

[160] J. Menders, P. Searcy, K. Roff, and E. Korevaar, *Blue cesium Faraday and Voigt magneto-optic atomic line filters*, Opt. Lett. **17**, 1388 (1992). 82

[161] S. Franke-Arnold, M. Arndt, and A. Zeilinger, *Magneto-optical effects with cold lithium atoms*, J. Phys. B: At. Mol. Opt. Phys. **34**, 2527 (2001). 82

[162] J. A. Nelder and R. Mead, *A Simplex Method for Function Minimization*, Comput. J. **7**, 308 (1965). 84

[163] K. J. R. Rosman and P. D. P. Taylor, *Isotopic compositions of the elements 1997 (Technical Report)*, Pure Appl. Chem. **70**, 217 (1998). 88, 99, 134

[164] J. Ye, S. Swartz, P. Jungner, and J. L. Hall, *Hyperfine structure and absolute frequency of the ^{87}Rb $5P_{3/2}$ state*, Opt. Lett. **21**, 1280 (1996). 89, 93, 136, 138

[165] S. Falke, E. Tiemann, C. Lisdat, H. Schnatz, and G. Grosche, *Transition frequencies of the D lines of ^{39}K, ^{40}K, and ^{41}K measured with a femtosecond laser frequency comb*, Phys. Rev. A **74**, 032503 (2006). 89, 136, 137

[166] P. Siddons, C. S. Adams, and I. G. Hughes, *Off-resonance absorption and dispersion in vapours of hot alkali-metal atoms*, J. Phys. B: At. Mol. Opt. Phys. **42**, 175004 (2009). 89

[167] M. D. Rotondaro and G. P. Perram, *Collisional broadening and shift of the rubidium D_1 and D_2 lines ($5^2S_{1/2} \rightarrow 5^2P_{1/2}$, $5^2P_{3/2}$) by rare gases, H_2, D_2, N_2, CH_4 and CF_4*, J. Quant. Spectrosc. Radiat. Transf. **57**, 497 (1997). 94

[168] N. D. Zameroski, G. D. Hager, W. Rudolph, C. J. Erickson, and D. A. Hostutler, *Pressure broadening and collisional shift of the Rb D2 absorption line by CH_4, C_2H_6, C_3H_8, n-C_4H_{10}, and He*, J. Quant. Spectrosc. Radiat. Transf. **112**, 59 (2011). 94

[169] I. Novikova, A. B. Matsko, and G. R. Welch, *Detection of nonresonant impurity gases in alkali vapor cells*, Appl. Phys. Lett. **81**, 193 (2002). 94

[170] N. P. Wells, T. U. Driskell, and J. C. Camparo, *Kr-collision shift of the Rb D_1 transition: The isoclinic point and precision optical spectroscopy*, Phys. Rev. A **89**, 052516 (2014). 94

[171] S. Brandt, A. Nagel, R. Wynands, and D. Meschede, *Buffer-gas-induced linewidth reduction of coherent dark resonances to below 50 Hz*, Phys. Rev. A **56**, R1063 (1997). 94

[172] Y. C. Chan and J. A. Gelbwachs, *Fraunhofer-wavelength magnetooptic atomic filter at 422.7 nm*, IEEE J. Quant. Electron. **29**, 2379 (1993). 95

[173] Z. Hu, X. Sun, Y. Liu, L. Fu, and X. Zeng, *Temperature properties of Na dispersive Faraday optical filter at D_1 and D_2 line*, Opt. Commun. **156**, 289 (1998). 95

[174] Y. Yong *et al.*, *A flat spectral Faraday filter for sodium lidar*, Opt. Lett. **36**, 1302 (2011). 95

[175] B. Yin and T. Shay, *A potassium Faraday anomalous dispersion optical filter*, Opt. Commun. **94**, 30 (1992). 95

[176] Q. Sun, Y. Hong, W. Zhuang, Z. Liu, and J. Chen, *Demonstration of an excited-state Faraday anomalous dispersion optical filter at 1529 nm by use of an electrodeless discharge rubidium vapor lamp*, Appl. Phys. Lett. **101**, 211102 (2012). 95

[177] D. Höckel and O. Benson, *Electromagnetically induced transparency in cesium vapor with probe pulses on the single-photon level*, Phys. Rev. Lett. **105**, 153605 (2010). 95

[178] Th. Udem, J. Reichert, R. Holzwarth, and T. W. Hänsch, *Absolute Optical Frequency Measurement of the Cesium D_1 Line with a Mode-Locked Laser*, Phys. Rev. Lett. **82**, 3568 (1999). 98, 136

[179] M. Widmann *et al.*, *Faraday Filtering on the Cs-D_1-Line for Quantum Hybrid Systems*, (2015), arXiv:1505.01719v1. 100

[180] V. Gerginov and C. E. Tanner, *Heterodyne frequency calibration of high resolution cesium spectra using diode lasers*, Opt. Commun. **216**, 391 (2003). 101

[181] A. S. Arnold, J. S. Wilson, and M. G. Boshier, *A simple extended-cavity diode laser*, Rev. Sci. Instrum. **69**, 1236 (1998). 101, 108

[182] S. D. Saliba and R. E. Scholten, *Linewidths below 100 kHz with external cavity diode lasers*, Appl. Opt. **48**, 6961 (2009). 102

[183] X. Zhang *et al.*, *An all-optical locking of a semiconductor laser to the atomic resonance line with 1 MHz accuracy*, Opt. Express **21**, 28010 (2013). 102

[184] L. D. Turner, K. P. Weber, C. J. Hawthorn, and R. E. Scholten, *Frequency noise characterisation of narrow linewidth diode lasers*, Opt. Commun. **201**, 391 (2002). 102

[185] T. Okoshi, K. Kikuchi, and A. Nakayama, *Novel method for high resolution measurement of laser output spectrum*, Electron. Lett. **16**, 630 (1980). 102

[186] A. E. Siegman, *Lasers*, 1st ed. (University Science Books, Sausalito, 1986). 104, 108

[187] L. C. Andrews and R. L. Phillips, *Mathematical Techniques for Engineers and Scientists* (SPIE, Bellingham, 2003). 109

[188] C. J. Hawthorn, K. P. Weber, and R. E. Scholten, *Littrow configuration tunable external cavity diode laser with fixed direction output beam*, Rev. Sci. Instrum. **72**, 4477 (2001). 110

[189] C. P. Pearman *et al.*, *Polarization spectroscopy of a closed atomic transition: applications to laser frequency locking*, J. Phys. B: At. Mol. Opt. Phys. **35**, 5141 (2002). 110

[190] T. F. Krauss, *Why do we need slow light?*, Nat. Photonics **2**, 448 (2008). 114

[191] S. Franke-Arnold, G. Gibson, R. W. Boyd, and M. J. Padgett, *Rotary photon drag enhanced by a slow-light medium*, Science **333**, 65 (2011). 114

[192] R. M. Camacho, M. V. Pack, J. C. Howell, A. Schweinsberg, and R. W. Boyd, *Wide-bandwidth, tunable, multiple-pulse-width optical delays using slow light in cesium vapor*, Phys. Rev. Lett. **98**, 153601 (2007). 114

[193] Z. Shi, R. W. Boyd, D. J. Gauthier, and C. C. Dudley, *Enhancing the Spectral Sensitivity and Resolution of Interferometers Using Slow-Light Media*, in *Conference on Lasers and Electro-Optics/Quantum Electronics and Laser Science Conference and Photonic Applications Systems Technologies*, p. CTuT2, 2007. 114

[194] P. Siddons, N. C. Bell, Y. Cai, C. S. Adams, and I. G. Hughes, *A gigahertz-bandwidth atomic probe based on the slow-light Faraday effect*, Nat. Photonics **3**, 225 (2008). 114, 121

[195] M. Fleischhauer, A. Imamoglu, and J. P. Marangos, *Electromagnetically induced transparency: Optics in coherent media*, Rev. Mod. Phys. **77**, 633 (2005). 114

[196] L. V. Hau, S. E. Harris, Z. Dutton, and C. H. Behroozi, *Light speed reduction to 17 metres per second in an ultracold atomic gas*, Nature **397**, 594 (1999). 114, 117, 118

[197] M. Kash *et al.*, *Ultraslow Group Velocity and Enhanced Nonlinear Optical Effects in a Coherently Driven Hot Atomic Gas*, Phys. Rev. Lett. **82**, 5229 (1999). 114

[198] P. Siddons, *Faraday Rotation of Pulsed and Continuous-wave Light in Atomic Vapour*, PhD thesis, University of Durham, 2011. 115

[199] G. Brooker, *Modern Classical Optics*, 1st ed. (Oxford University Press, Oxford, 2003). 116

[200] L. Brillouin, *Wave Propagation and Group Velocity*, 1st ed. (Academic Press, 1960). 116

[201] L. J. Wang, A. Kuzmich, and A. Dogariu, *Gain-assisted superluminal light propagation*, Nature **406**, 277 (2000). 117

[202] R. Zhang, J. A. Greenberg, M. C. Fischer, and D. J. Gauthier, *Controllable ultrabroadband slow light in a warm rubidium vapor*, J. Opt. Soc. Am. B **28**, 2578 (2011). 118

[203] R. Löw and T. Pfau, *Magneto-optics: Hot atoms rotate light rapidly*, Nat. Photonics **3**, 197 (2009). 121

[204] H. Orth, H. Ackermann, and E. W. Otten, *Fine and hyperfine structure of the 2^2P term of ^7Li; Determination of the nuclear quadrupole moment*, Z Phys. A **273**, 221 (1975). 125

[205] H. Lin *et al.*, *Improved determination of the Boltzmann constant using a single, fixed-length cylindrical cavity*, Metrologia **50**, 417 (2013). 126

[206] G.-W. Truong, E. F. May, T. M. Stace, and A. Luiten, *Quantitative atomic spectroscopy for primary thermometry*, Phys. Rev. A **83**, 033805 (2011). 126

[207] D. Budker and D. F. J. Kimball, editors, *Optical Magnetometry*, 2nd ed. (Cambridge University Press, Cambridge, 2013). 126

[208] R. E. Caflisch, *Monte Carlo and quasi-Monte Carlo methods*, Acta Numer. **7**, 1 (1998). 131

[209] E. Jones, T. Oliphant, P. Peterson, and Others, *SciPy: Open source scientific tools for Python*, http://www.scipy.org/, 2001–, Accessed: 2015-05-12. 135

[210] P. J. Mohr, B. N. Taylor, and D. B. Newell, *CODATA recommended values of the fundamental physical constants: 2010*, Rev. Mod. Phys. **84**, 1527 (2012). 135

[211] P. Juncar, J. Pinard, J. Hamon, and A. Chartier, *Absolute Determination of the Wavelengths of the Sodium D_1 and D_2 Lines by Using a CW Tunable Dye Laser Stabilized on Iodine*, Metrologia **17**, 77 (1981). 136

[212] U. Volz, M. Majerus, H. Liebel, A. Schmitt, and H. Schmoranzer, *Precision Lifetime Measurements on NaI $3p\ ^2P_{1/2}$ and $3p\ ^2P_{3/2}$ by Beam-Gas-Laser Spectroscopy*, Phys. Rev. Lett. **76**, 2862 (1996). 136

[213] H. Wang, P. L. Gould, and W. C. Stwalley, *Long-range interaction of the $^{39}K(4s)+^{39}K(4p)$ asymptote by photoassociative spectroscopy. I. The 0_g^- pure long-range state and the long-range potential constants*, J. Chem. Phys. **106**, 7899 (1997). 136

[214] A. Banerjee, D. Das, and V. Natarajan, *Absolute frequency measurements of the D_1 lines in ^{39}K, ^{85}Rb, and ^{87}Rb with ~ 0.1 ppb uncertainty*, Europhys. Lett. **65**, 172 (2004). 136, 137, 138

[215] U. Volz and H. Schmoranzer, *Precision lifetime measurements on alkali atoms and on helium by beam–gas–laser spectroscopy*, Phys. Scr. **T65**, 48 (1996). 136

[216] J. M. Amini and H. Gould, *High Precision Measurement of the Static Dipole Polarizability of Cesium*, Phys. Rev. Lett. **91**, 153001 (2003). 136

[217] Th. Udem, J. Reichert, T. W. Hänsch, and M. Kourogi, *Absolute optical frequency measurement of the cesium D_2 line*, Phys. Rev. A **62**, 031801 (2000). 136, 138

[218] J. F. Sell *et al.*, *Lifetime measurement of the cesium $6P_{3/2}$ state using ultrafast laser-pulse excitation and ionization*, Phys. Rev. A **84**, 010501 (2011). 136

[219] E. Arimondo, M. Inguscio, and P. Violino, *Experimental determinations of the hyperfine structure in the alkali atoms*, Rev. Mod. Phys. **49**, 31 (1977). 136, 137, 138

[220] W. A. van Wijngaarden and J. Li, *Measurement of hyperfine structure of sodium $3P_{1/2,3/2}$ states using optical spectroscopy*, Z Phys. D **32**, 67 (1994). 136

[221] W. Yei, A. Sieradzan, and M. D. Havey, *Delayed-detection measurement of atomic Na 3p $^2P_{3/2}$ hyperfine structure using polarization quantum-beat spectroscopy*, Phys. Rev. A **48**, 1909 (1993). 136

[222] M. P. Bradley, J. V. Porto, S. Rainville, J. K. Thompson, and D. E. Pritchard, *Penning Trap Measurements of the Masses of ^{133}Cs, $^{87,85}Rb$, and ^{23}Na with Uncertainties $\leq 0.2\,ppb$*, Phys. Rev. Lett. **83**, 4510 (1999). 136, 137, 138

[223] G. Audi, A. H. Wapstra, and C. Thibault, *The AME2003 atomic mass evaluation: (II). Tables, graphs and references*, Nucl. Phys. A **729**, 337 (2003). 137, 138

[224] U. D. Rapol, A. Krishna, and V. Natarajan, *Precise measurement of hyperfine structure in the $5P_{3/2}$ state of ^{85}Rb*, Eur. Phys. J. D **23**, 185 (2003). 137

[225] S. Bize *et al.*, *High-accuracy measurement of the ^{87}Rb ground-state hyperfine splitting in an atomic fountain*, Europhys. Lett. **45**, 558 (1999). 138